Università degli Studi "Roma Tre"

Scuola Dottorale in Scienze Matematiche e Fisiche

Dottorato di Ricerca in Fisica - XXVI Ciclo

Study of associated production of W-Higgs boson with the ATLAS detector

Candidato:
Valerio Bortolotto

Supervisor:
Prof.ssa Domizia Orestano

January 2014

A tutti i miei parenti,
in particolare ai miei genitori.
A tutti i miei amici,
in particolare ai F. Muppets.
A Sara,
in particolare a Sara.

“Perché vedi l’avere ragione
non è un dogma statico una religione
ma è seguire la dinamica della storia
e mettersi sempre in discussione.
Perché sai non basta
scegliere di avere l’idea giusta
assumerne il linguaggio ed il comportamento
poi dormire dentro.”

“Non diventare grande mai”, Eugenio Finardi.

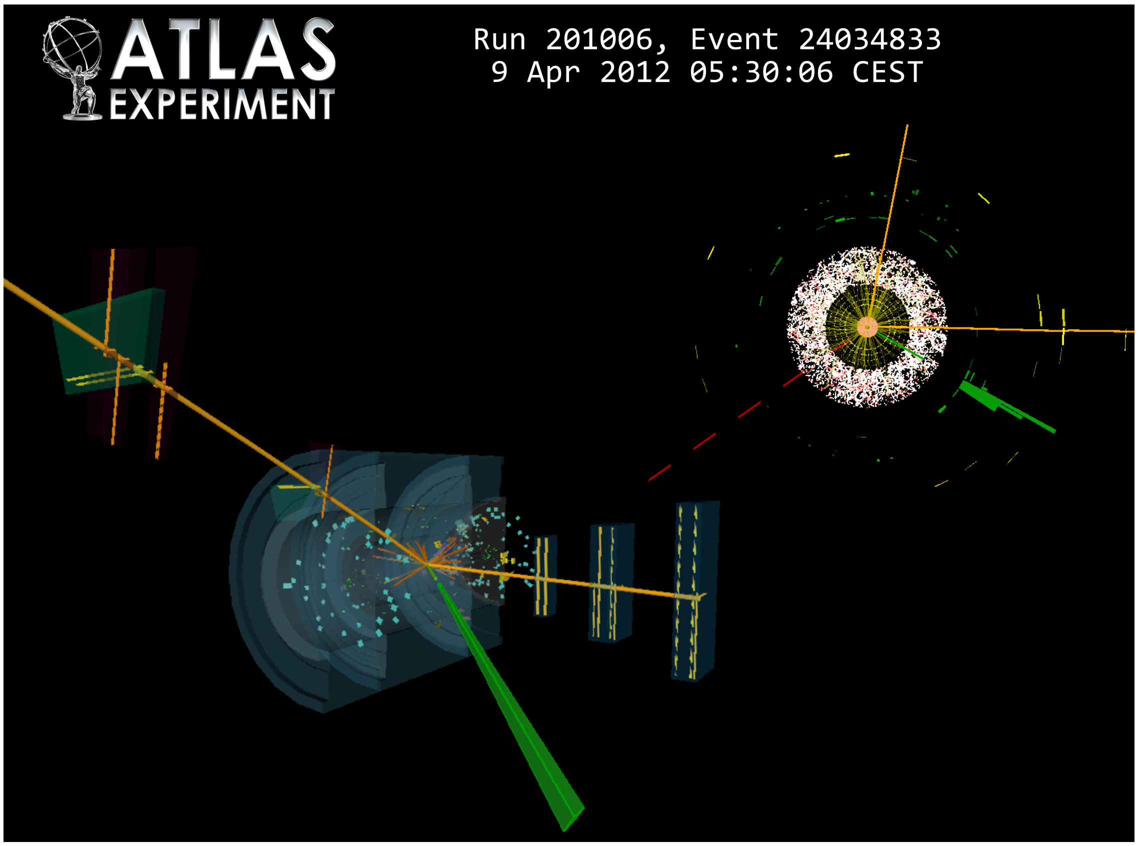

Figure 1: Display of a WH associated production candidate event. The reconstructed lepton p_T values are 23.5 (μ^+), 25.2 (μ^+) and 88.5 (e^-) GeV. (from https://atlas.web.cern.ch/Atlas/GROUPS/PHYSICS/CONFNOTES/ATLAS-CONF-2013-075/)

Contents

Introduction

The 19th century has seen the birth of the Standard Model (SM), a mathematical model based upon field theory, able to describe and predict most of the phenomena at the energy scale accessible at the colliders. One of the most important parts of this model is the Electroweak Symmetry Breaking, the mechanism that allows the particles to acquire mass. The introduction of this symmetry breaking added a new particle: a spin 0 boson, also called Higgs boson. Since the introduction of this mechanism in 1964 a huge effort to search for this particle was made by several groups of physicists. The Large Hadron Collider (LHC), a proton-proton collider at CERN, was built mainly to discover this particle and study its properties. In particular two detectors, ATLAS and CMS, were designed to search for it. In the 4th of July 2012, both the experiments, announced the discovery of a boson with properties consistent with those expected from the Electroweak Symmetry Breaking model. After the discovery, the effort was focused on the study of the properties with data acquired in 2011 and 2012 years. In particular the interactions between the Higgs boson and the SM particles became relevant to verify its nature and that is the reason why the study of associated production modes at LHC acquired more relevance.

The main goal of this thesis is to present a study of one of the Standard Model Higgs boson production mechanisms allowed at the LHC. The analysis is focused on the Higgs boson produced in association with a vector boson W. The Higgs boson decay investigated, due to the large branching ratio, is the $H \to WW^{(*)}$. Due to the more clear signature only a fully leptonic final state is analyzed. Because of the higher statistic compared with the 2011, the thesis focuses on the data acquired by the ATLAS detector in the 2012 but to have a more complete study of the $WH \to WWW^{(*)} \to l\nu l\nu l\nu$ channel the analysis described is combined with the analysis performed using the data acquired by the ATLAS detector in the 2011. Additionally due to the connection between the associated production of an Higgs boson with a Z boson and the WH production a combination of the two analyses involving the $H \to WW^{(*)}$ decay is presented. Finally a combination of the main Higgs boson production mechanisms (vector-boson fusion, gluon-gluon fusion and associated production with a W or Z bosons) at the LHC considering only the $H \to WW^{(*)}$ decay is reported to give to the reader a complete description of the $H \to WW^{(*)}$ channel.

In this thesis an introduction to the Standard Model is presented in chapter 1 while a description of the Higgs boson production at the Large Hadron Collider is reported in chapter 2. In chapter 3 the LHC collider and the ATLAS apparatus are described. Chapter 4 presents the physical object definitions in the ATLAS experiment while in chapters 5 and 6 a description of the analysis, from event selection to statistical treatment, and final results are reported.

Chapter 1

The Standard Model

The Standard Model (SM) is the model used in particles physics to describe the particles and their interactions. With the high energy physics experiments, in particular with those connected to the colliders, the SM was stressed a lot but its predictions were found in agreement with the experimental results. The SM seems to give a detailed description of the phenomena that the particle physics investigated so far at least up to the energy scale reached by the collider up to now. Although the SM provides an explanation of the processes observed in the experiments there are still open issues concerning this model. In particular the main problem is the introduction of the particles masses. In this chapter we report a brief introduction to the SM formalism and theory [1] [2] [3] (section 1.1) and an explanation of the mechanism developed by Peter Higgs [4] and independently by Robert Brout and Francois Englert [5], and Gerald Guralnik, C.R. Hagen and Tom Kibble [6] to solve the massless particle problem, the Electroweak Symmetry Breaking (section 1.2).

1.1 Introduction to the SM

The Standard Model is a $SU(3)_C \times SU(2)_L \times U(1)_Y$ quantum field theory. These groups correspond to local gauge symmetry and the associated Lagrangian is required to be invariant under local transformations in each group. The Standard Model is described by particles carrying the forces and particles constituents of matter. The first ones are spin integer bosons and are classified according to the mediated force and the type of interaction. The constituents of matter are 12 fermions divided in leptons and quarks according to the forces to which they are subject.

All the fermions interact via the weak force while quarks and charged leptons are subject also to the electromagnetic interaction. Only the quarks are subject to the strong force. The fermions have spin-1/2 and are divided in doublets according to electric charge and in families (also called generations) according to the mass of the particles. Particles that, according to the doublets, are of the same type, have the same quantum numbers. Considering the leptons sector the doublets are divided in charged lepton (with electric charge “e”, that is the absolute value of the electron charge) and neutral lepton (neutrinos). The lightest charged lepton is the electron while the muon and the tau are respectively the leptons of the second and third generation. The other particles of the lepton doublets are the neutrinos whose flavor is derived from the associated leptonic number.

In the quark sector the doublets are divided in a different way. Both the particles of the doublets are electrically charged, with a fractionally charge compared with the leptons. In particular the doublets are split in up-quark, with charge $+\frac{2}{3}e$, and down-quark, with charge $-\frac{1}{3}e$. The up quarks of the three families are: up, charm and top; while the down quarks are: down, strange and bottom. For both leptons and quarks the doublets scheme described above is related to the weak force. In particular particles of the same doublet appear together in order to conserve the associated quantum number. All the fermions have an anti-particle partner. Those anti-particles have the same mass and spin of the described particle but opposite values of all other quantum numbers, including the electric charge. In table 1.1 the properties of fermions are summarized.

The SM describes also the interactions between the particles for three of the four forces of the nature. According to the model the interactions occur via the exchange of particles (bosons), mediating the force. The bosons introduced by the SM to describe the electromagnetic, weak and strong interactions are 12. As described in section 1.1.2 (Electroweak theory) it was demonstrated that the electromagnetic and weak interactions can be unified into one force, the electroweak force. This model requires four bosons mediating the interaction, two charged and two not charged. The neutral force carriers are the γ (related to the electromagnetic interactions) and the Z (related to the weak interactions) while the two charged bosons are $W^{\pm}$ (related to the weak interactions). The Z is responsible of neutral current interactions while the W bosons are the force carriers involved in flavor-changing interactions. The other 8 bosons are the particles mediating the strong interaction, the gluons. The gluons are massless and with null electric charge but with another kind of charge, the color. There are 3 charges of color let’s call them red (r), blue (b) and green (g), and all the gluons are composed by colored and anti-colored charges. The several combinations of color-anticolor pairs give rise to a base composed by 8 different bosons:
$r\overline{g}, r\overline{b}, g\overline{b}, g\overline{r}, b\overline{r}, b\overline{g}, \frac{r\overline{r}-g\overline{g}}{\sqrt{2}}, \frac{r\overline{r}+g\overline{g}-2b\overline{b}}{\sqrt{6}}$.

In table 1.2 the properties of the particle force carrier are summarized. In the

Particle	Interactions	Mass	Charge (e)
First Family			
electron (e)	Electrom., Weak	$0.511 \pm 1.3 \times 10^{-8}$ MeV	$-e$
neutrino e (ν_e)	Weak	$< 2eV$	0
up quark (u)	Strong, Electrom., Weak	$1.7 - 3.1$ MeV	$+\frac{2}{3}e$
down quark (d)	Strong, Electrom., Weak	$4.1 - 5.7$ MeV	$-\frac{1}{3}e$
Second Family			
muon (μ)	Electrom., Weak	$105.7 \pm 4 \times 10^{-6}$ MeV	$-e$
neutrino μ (ν_μ)	Weak	$< 2eV$	0
charm quark (c)	Strong, Electrom., Weak	$1.29^{+0.05}_{-0.11}$ GeV	$+\frac{2}{3}e$
strange quark (s)	Strong, Electrom., Weak	100^{+30}_{-20} MeV	$-\frac{1}{3}e$
Third Family			
tau (τ)	Electrom., Weak	1.77 ± 0.16 GeV	$-e$
neutrino τ (ν_τ)	Weak	$< 2eV$	0
top quark (t)	Strong, Electrom., Weak	$172.9 \pm 0.6 \pm 0.9$ GeV	$+\frac{2}{3}e$
bottom quark (b)	Strong, Electrom., Weak	$4.19^{+0.18}_{-0.06}$ GeV	$-\frac{1}{3}e$

Table 1.1: Overview of leptons and quarks properties.

Particle	Interactions	Mass	Charge (e)
photon (γ)	Electrom.	0	0
$W^\pm$	Weak	80.385 ± 0.015 GeV	$\pm e$
Z^0	Weak	91.188 ± 0.002 GeV	0
gluon (g)	Strong	0	0

Table 1.2: Overview of bosons properties.

next sections a more detailed description of the SM is reported, starting from the theory connected to the quarks sector.

1.1.1 QCD

The SM can be divided in two main theories, one taking into account the electromagnetic and the weak interactions, the electroweak theory (represented by the $SU(2)_L \times U(1)_Y$), and one taking into account the strong force, the Quantum Chromo Dynamics (QCD). While the electroweak theory is mainly connected to the lepton and quark sector of the SM, the QCD focuses on the quarks and gluons. The QCD is described by a $SU(3)$ group and is composed by eight spin-1 massless gluon fields G^{α}_{μ} ($\alpha = 1, ..., 8$) and quark Q. The Q are triplets under the $SU(3)$. In QCD there are three color charges. The Lagrangian of the QCD is

$$L_{QCD} = \overline{Q}(i\gamma^{\mu} D_{\mu} - m)Q - \frac{1}{4} G^{\alpha}_{\mu\nu} G^{\mu\nu}_{\alpha} \tag{1.1}$$

with $G^{\alpha}_{\mu\nu}$ field strength tensor of G^{α}_{μ} and g_s strong coupling. The algebra of $SU(3)$ is non-commuting and this gives rise to the self-interaction of the gluon fields. The structure of the $SU(3)_C$ gauge symmetry, where C stands for color, gives two peculiar properties to the QCD: the asymptotic freedom and the confinement.

The first one is connected to the behavior of the strong coupling constant α_s as a function of the transfer momentum q of the interacting particles. In particular α_s decreases with the increasing of the energy scale Q (defined as $Q^2 = |q^2|$) and asymptotically vanishes for $Q^2 \to \infty$. This means that at short distances or large transfer momentum the strong interaction becomes weak and quarks can be considered as free particles. For large momentum transfers we can apply the perturbation theory to make predictions, but this is not true for large distance or low energy. In this energy regime α_s increases and the perturbative approach is no longer applicable to the QCD calculations. The behavior of α_s also explain the confinement property. Trying to separate two colored particles means create a infinite distance between the two particles. In QCD an increase of distances is related to an increase of binding energy. At a certain point the creation of quark-antiquark pairs from the vacuum becomes energetically favored compared with the binding energy. This property is the so called confinement. The main consequence of the confinement is the impossibility to observe a colored particle alone. For the strong force it is less energetically favorable to have colored particles separated than to produce quark-antiquark pairs, which can join the existing quarks producing uncolored hadrons. Hadrons should be always not-colored so only particles with a color-anticolor couple of quark (called mesons) or particles with a combination of three different colored quarks (baryons) could exist. The process described above is known as hadronization and it is, at sufficient high energies, the mechanism forcing the hadrons to propagate together in a cluster of particles, the so called jet.

1.1.2 Electroweak theory

This model was developed in primis in the late 1960's by Sheldon Glashow, Steven Weinberg and Abdul Salam [7] [8]. They described how it would be possible to treat electromagnetic and weak interactions as different aspects of a single electroweak interaction, with a single coupling given by the electric charge (e). To unify the weak and electromagnetic interactions they used a $SU(2)_L \times U(1)_Y$ gauge theory (the GWS theory). This theory is based on a gauge symmetry group of the weak isospin and weak hypercharges. According to the GWS theory the symmetry between electromagnetic and weak interactions would be manifest at large transfers momentum ($q^2 \gg 10^4$ GeV^2). This symmetry, at low energies, would be broken. For a better understanding of the SM and of the electroweak symmetry breaking (section 1.2) it is useful to introduce the electroweak Lagrangian. The behavior of a relativistic spin-1/2 field $\psi(x)$ in free space is described by the Lagrangian

$$L_{Dirac}(x) = \overline{\psi}(x)(i\gamma^\mu\partial_\mu - m)\psi(x) \tag{1.2}$$

In 4 dimensions γ^μ is a matrix (4×4) with anticommutation relationships

$$\{\gamma^\mu, \gamma^\nu\} = 2g^{\mu\nu} \tag{1.3}$$

with $g^{\mu\nu}$ metric tensor. From the 1.2 using the Eulero-Lagrange formula it is possible to derive the equation of motion for the field $\psi(x)$.

$$(i\gamma^\mu\partial_\mu - m)\psi(x) = 0 \tag{1.4}$$

It's possible to take into account the interaction with the electromagnetic field introducing in the Lagrangian a term proportional to $F^{\mu\nu}F_{\mu\nu}$ where the $F^{\mu\nu}$ is the field tensor introduced to express the Maxwell's equations in a covariant form. The field tensor is

$$F^{\mu\nu}(x) = \partial^\nu A^\mu(x) - \partial^\mu A^\nu(x) \tag{1.5}$$

with $A^\mu = (\phi, A)$. With the introduction of the interaction term the Lagrangian becomes

$$L_{QED} = \overline{\psi}(x)(i\gamma^{\mu}\partial_{\mu} - m)\psi(x) - \frac{1}{4}F_{\mu\nu}F^{\mu\nu} \tag{1.6}$$

where QED stands for Quantum Electro Dynamics. This is the theory which describes the interaction between a charged particle and the electromagnetic field. Applying the Eulero-Lagrange equation with respect to the field ψ it's possible to obtain the equation of motion

$$(i\gamma^{\mu}\partial_{\mu} - m)\psi(x) = -e\gamma^{\mu}A_{\mu}\psi(x) \tag{1.7}$$

To obtain an electroweak Lagrangian that takes into account the phenomena connected to the weak interaction new terms should be included in the L_{QED}. In particular the electroweak theory is described by a $SU(2)_L \times U(1)_Y$ gauge symmetry so it's necessary to introduce spin-1 gauge fields W_{μ}^{α} ($\alpha = 1, 2, 3$) transforming under the adjoint of the $SU(2)_L$ group and a gauge field B_{μ} associated with $U(1)_Y$. These gauge fields correspond to two charged and two neutral force carriers. To understand this theory is interesting to describe how the particles are related to the groups. The particles could be classified as right-handed or left-handed based on whether the spin and momentum vectors are parallel or antiparallel. The right-handed fermions ψ_R are singlets under $SU(2)_L$ and transform under $U(1)_Y$ while the left-handed fermions ψ_L are SU(2) doublets. This means that B_{μ} couples to both the left-handed and right-handed components of the fermion fields while the W_{μ}^{i} gauge fields only couple to the left-handed components. The left-handed projections of the fermion fields form weak isospin doublets of the form

$$\psi_L = \begin{pmatrix} \nu_l \\ l^- \end{pmatrix}_L, \begin{pmatrix} q_u \\ q_d \end{pmatrix}_L \tag{1.8}$$

where ψ_L could be either leptons or quarks. This doublet structure is present in all the generations. The right-handed projections form a $SU(2)_L$ singlets.

$$\psi_R = l_R, q_{uR}, q_{dR} \tag{1.9}$$

The electroweak Lagrangian can be written as a sum of two components:

$$L_{EW} = L_G + L_F \tag{1.10}$$

where L_G is the Lagrangian in which only gauge fields appears and L_F is connected to the fermions and their interactions with the gauge bosons. According to the gauge field introduced above it's possible to write the L_G as

$$L_G = -\frac{1}{4}W^{\alpha}_{\mu\nu}W^{\mu\nu}_{\alpha} - \frac{1}{4}B^{\mu\nu}B_{\mu\nu} \tag{1.11}$$

with the field strengths defined by

$$W^a_{\mu\nu} = \partial_\mu W^a_\nu - \partial_\nu W^a_\mu + g\epsilon^{abc}W^b_\mu W^c_\nu \tag{1.12}$$

and

$$B_{\mu\nu} = \partial_\mu B_\nu - \partial_\nu B_\mu \tag{1.13}$$

where g is the weak $SU(2)_L$ coupling constant.

The bosons coupling actually to the fermions are a mixture of these gauge fields. In particular introducing a rotation angle, the so called Weinberg angle θ_W, it's possible to write the neutral bosons as a linear combination of the gauge fields B_μ and W^3_μ as

$$\begin{pmatrix} A_\mu \\ Z_\mu \end{pmatrix} = \begin{pmatrix} cos\theta_W & sin\theta_W \\ -sin\theta_W & cos\theta_W \end{pmatrix} \begin{pmatrix} B_\mu \\ W^3_\mu \end{pmatrix} \tag{1.14}$$

and the charged ones as

$$W^\pm_\mu = \frac{1}{\sqrt{2}}W^1_\mu \pm iW^2_\mu \tag{1.15}$$

where the $sin\theta_W = g_1/\sqrt{g_1^2 + g_2^2}$ and $cos\theta_W = g_2/\sqrt{g_1^2 + g_2^2}$. There is a relation between g_1, g_2 and the electric charge e of the form

$$g_1 sin\theta_W = g_2 cos\theta_W = e \tag{1.16}$$

The remaining part of the Lagrangian L_F is

$$L_F = i\overline{\psi}_L\gamma^\mu D_{\mu L}\psi_L + i\overline{\psi}_R\gamma^\mu D_{\mu R}\psi_R \tag{1.17}$$

with D_μ, the covariant derivative

$$D_\mu = \left(\partial_\mu + ig_1\frac{\sigma_i}{2}W^i_\mu + ig_2\frac{Y_\phi}{2}B_\mu\right) \tag{1.18}$$

where B_μ and W_μ are the gauge fields introducing in the electroweak theory, Y is the weak hypercharge and g_1 and g_2 are the $SU(2)_L$ and $U(1)_Y$ gauge couplings.

1.2 Electroweak Symmetry Breaking and Higgs sector

In the electroweak Lagrangian described above there are no mass terms for fermions and bosons but this is in contrast with the experimental results. The observations suggested that all fermions and bosons, but the photons and the gluons, have mass. It's possible to show that introduce by hand mass terms in the Lagrangian, will break the gauge symmetry. Considering for instance a fermion mass term of the Lagrangian of the form

$$L_{massfer} = m\overline{\psi}\psi \tag{1.19}$$

Introducing the helicity states it's possible to demonstrate that

$$L_{massfer} = m\overline{\psi}_L\psi_R + m\overline{\psi}_R\psi_L \tag{1.20}$$

Since right-handed leptons are singlets while left-handed are doublets these terms are doublets in the $SU(2)_L$ space, so the $SU(2)_L$ gauge symmetry is broken. The bosons mass terms break the $U(1)_Y$ symmetry. A boson mass term of the Lagrangian has the form:

$$L_{massbos} = \frac{1}{2}m^2A^\mu A_\mu \tag{1.21}$$

but the $U(1)_Y$ symmetry, connected to the covariant form of the Maxwell's equations, imposes invariance under

$$A_\mu \to A_\mu - \partial_\mu\theta(x) \tag{1.22}$$

Applying this transformation to the 1.21

$$\frac{1}{2}m^2A^\mu A_\mu \to \frac{1}{2}m^2(A^\mu - \partial^\mu\theta(x))(A_\mu - \partial_\mu\theta(x)) \tag{1.23}$$

it can be seen that since $\theta(x)$ is an arbitrary phase the only way to have these terms equal is to require m=0.

Since experimentally mass terms of fermions and bosons are observed a mechanism that incorporates the mass terms in the Lagrangian without violating the gauge symmetry is needed. It's possible to solve the mass problem via a mechanism discovered in the 1964 by Higgs [4], Brout and Englert [5], and Guralnik Hagen, and

Kibble [6] that now is called the Higgs mechanism or spontaneous symmetry breaking. The idea is to introduce an additional complex scalar (spin-0) multiplet of the $SU(2)_L$ gauge group

$$\phi = \begin{pmatrix} \phi^+ \\ \phi^0 \end{pmatrix} \tag{1.24}$$

with electrically charged (ϕ^+) and neutral (ϕ^0) components. The Lagrangian corresponding to this doublet has the form:

$$L_H = (D^\mu \phi)^\dagger (D_\mu \phi) - V(\phi) \tag{1.25}$$

The 1.25 also contains a potential V in which the Higgs field self-interaction is taken into account. The V has the form:

$$V(\phi) = \mu^2 \phi^\dagger \phi + \lambda (\phi^\dagger \phi)^2 \tag{1.26}$$

with $\lambda > 0$. In figure 1.1 the shape of the potential for $\mu^2 > 0$ and $\mu^2 < 0$ is shown.

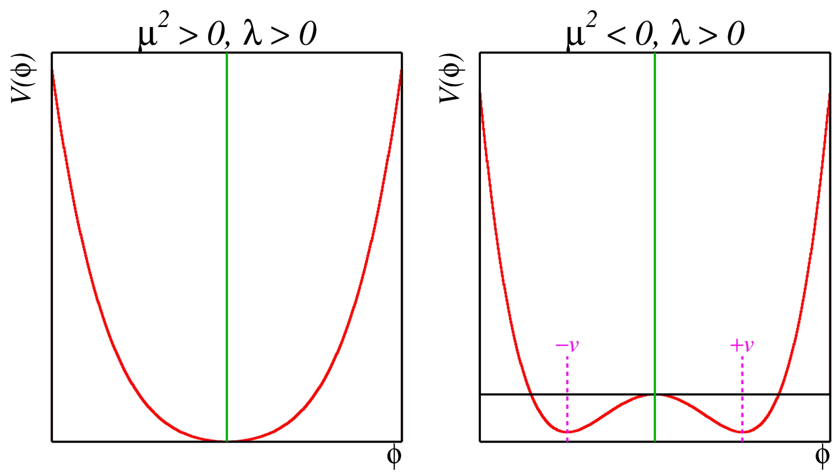

Figure 1.1: Higgs field potential in case of $\mu^2 > 0$ (left) and $\mu^2 < 0$ (right). In case of $\mu^2 > 0$ the minimum of the potential is at $\phi = 0$ while for $\mu^2 < 0$ the minimum is not at $\phi = 0$.

In case of $\mu^2 > 0$ (figure 1.1 left) the minimum of $V(\phi)$ is at $\phi = 0$ while for $\mu^2 < 0$ (figure 1.1 right and figure 1.2) the minimum is not at $\phi = 0$ but in a configuration satisfying the relation

$$|\phi_0^2| = -\frac{\mu^2}{2\lambda} = \frac{v^2}{2} \tag{1.27}$$

with v, the vacuum expectation value, different from 0. As shown in figure 1.2 there are infinitely many ground states.

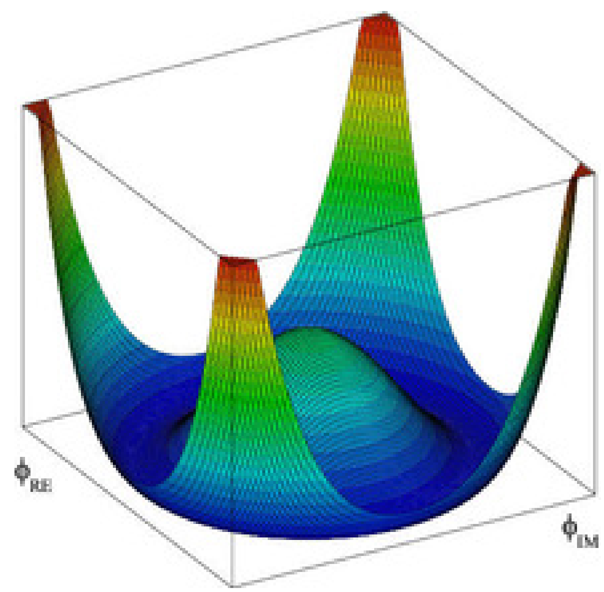

Figure 1.2: Higgs field potential in case of $\mu^2 < 0$.

Selecting one specific vacuum state the $SU(2)_L \times U(1)_Y$ gauge symmetry is broken but the full gauge symmetry of the Lagrangian, describing the electroweak interaction, is preserved. Since the ϕ doublet is $SU(2)_L$ invariant, it is always possible to find a gauge transformation (a rotation) that removes the upper component. Applying this transformation to the doublet it is possible to express ϕ_0 in the form

$$\phi_0 = \frac{1}{\sqrt{2}} \begin{pmatrix} 0 \\ v \end{pmatrix} \tag{1.28}$$

It's always possible to study a deviation, $\sigma(x)$, around a vacuum expectation value. The ϕ_0 doublet according to this expansion becomes:

$$\phi_0 = \frac{1}{\sqrt{2}} \begin{pmatrix} 0 \\ v + \sigma(x) \end{pmatrix} \tag{1.29}$$

$\sigma(x)$ is the scalar field which represents the physical Higgs boson. By adding a term in the Electroweak Lagrangian that takes into account the new scalar field it is possible to calculate the mass of bosons and fermions. The introduction of this particle solves the mass problem of the SM. Focusing on the boson sector and in particular in the boson-boson interaction, taking into account the quantization of the fields that allows to describe with the usual fields the particles, the Lagrangian is

$$L_{bosons} = L_{BB} + L_{HB} + L_{HH} \tag{1.30}$$

with

$$\begin{aligned} L_{BB} =& igcos\theta_W[(W^\dagger_\alpha W_\beta - W^\dagger_\beta W_\alpha)\partial^\alpha Z^\beta + (\partial_\alpha W_\beta - \partial_\beta W_\alpha)W^{\dagger\beta}Z^\alpha - (\partial_\alpha W^\dagger_\beta - \partial_\beta W^\dagger_\alpha)W^\beta Z^\alpha]+ \\ &+ ie[(W^\dagger_\alpha W_\beta - W^\dagger_\beta W_\alpha)\partial^\alpha A^\beta + (\partial_\alpha W_\beta - \partial_\beta W_\alpha)W^{\dagger\beta}A^\alpha - (\partial_\alpha W^\dagger_\beta - \partial_\beta W^\dagger_\alpha)W^\beta A^\alpha]+ \\ &+ g^2cos^2\theta_W[W_\alpha W^\dagger_\beta Z^\alpha Z^\beta - W_\beta W^{\dagger\beta}Z_\alpha Z^\alpha]+ \\ &+ e^2[W_\alpha W^\dagger_\beta A^\alpha A^\beta - W_\beta W^{\dagger\beta}A_\alpha A^\alpha]+ \\ &+ egcos\theta_W[W_\alpha W^\dagger_\beta(Z^\alpha A^\beta + A^\alpha Z^\beta) - 2W_\beta W^{\dagger\beta}A_\alpha Z^\alpha]+ \\ &+ \frac{1}{2}g^2W^\dagger_\alpha W_\beta[W^{\dagger\alpha}W^\beta - W^\alpha W^{\dagger\beta}] \end{aligned} \tag{1.31}$$

$$\begin{aligned} L_{HB} =& \frac{1}{2}vg^2W^\dagger_\alpha W^\alpha\sigma + \frac{1}{4}g^2W^\dagger_\alpha W^\alpha\sigma^2+ \\ &+ \frac{vg^2}{4cos^2\theta_W}Z_\alpha Z^\alpha\sigma + \frac{g^2}{8cos^2\theta_W}Z_\alpha Z^\alpha\sigma^2 \end{aligned} \tag{1.32}$$

$$L_{HH} = \frac{1}{4}\lambda\sigma^4 - \lambda v\sigma^3 \tag{1.33}$$

from eq.1.32 it's possible to derive the mass of the particles mediating the electroweak force while from 1.33 the mass of the Higgs boson. In particular according to L_{HB} it's possible to define the masses of $W^\pm$ and Z^0 as

$$m_W = \frac{1}{2}vg, m_Z = \frac{m_W}{cos\theta_W} \tag{1.34}$$

with

$$v = \left(-\frac{\mu^2}{\lambda}\right)^{\frac{1}{2}} \tag{1.35}$$

Since there is no interaction between the γ (photon) and the Higgs boson, the photon remains massless as observed. In this theory, all the masses of the bosons, including the Higgs boson itself, arise from the interaction of the gauge field with the Higgs field. To introduce the masses of the fermions it's necessary to introduce, in the Lagrangian, interaction terms between the fermion fields and the Higgs field. This additional term of the Lagrangian is called Yukawa term and the couplings between the fermions and the scalar field ϕ are called Yukawa couplings. The Lagrangian that takes into account the lepton-Higgs boson interaction has the form:

$$L_{LH} = -\frac{1}{v} m_l \overline{\psi}_l \psi_l \sigma - \frac{1}{v} m_{\nu l} \overline{\psi}_{\nu l} \psi_{\nu l} \sigma \tag{1.36}$$

where m_l and $m_{\nu l}$ are

$$m_l = \frac{v g_l}{\sqrt{2}}, m_{\nu l} = \frac{v g_{\nu l}}{\sqrt{2}} \tag{1.37}$$

with g_l and $g_{\nu l}$ the Yukawa couplings.

One important point in this theory is connected to the Higgs boson self-interaction, 1.33. In this theory is the Higgs field itself that gives mass to the Higgs boson. The Higgs boson mass it's:

$$m_H = \sqrt{-2\mu^2} = \sqrt{2\lambda v^2} \tag{1.38}$$

Considering the equations 1.33, 1.37 and 1.38 all the fermions and bosons masses are described by 6 base parameters

$$g_1, g_2, \mu^2, \lambda, g_l \text{ and } g_{\nu l} \tag{1.39}$$

It's possible to express the parameter v in terms of G ($G = 1.166 \times 10^{-5}$ GeV^{-2}) as

$$v = \left(G\sqrt{2}\right)^{\frac{1}{2}} \tag{1.40}$$

and so the W and Z masses as

$$m_W = \left(\frac{\alpha\pi}{G\sqrt{2}}\right)^{\frac{1}{2}} \frac{1}{sin\theta_W} \tag{1.41}$$

$$m_Z = \left(\frac{\alpha\pi}{G\sqrt{2}}\right)^{\frac{1}{2}} \frac{2}{sin2\theta_W} \tag{1.42}$$

As shown in 1.16 it's possible to calculate the g_1 and g_2 coupling constant measuring the weak mixing angle while g_l and $g_{\nu l}$ are known from the measurement of the masses. The only free parameter of this theory is λ that could be determined only by measuring the Higgs self-coupling term L_{HH}, this explain why, in the last 50 years, there was an huge effort in searching for this particle.

Chapter 2

The search for the Standard Model Higgs boson at the Large Hadron Collider

As discussed in the previous chapter the Higgs boson's mass in the SM is a free parameter so it's not possible to find theoretically the mass of this particle. Before the discovery of a particle Higgs SM boson like, with a mass of about 125 GeV, by the ATLAS and CMS experiments there were only theoretical and experimental constraints on this parameter. The Feynman diagrams involving the emission and reabsorption of an Higgs boson contribute to high-order corrections. Without them the electroweak theory would not be renormalizable. If the Higgs mass was large (order of TeV) the contribution due to these corrections would become huge, that's why the perturbation theory calculation requires an m_H lower than 10^3 GeV .

From the experimental point of view limits on the Higgs mass were produced from direct searches performed by several collaborations, in particular from the experiments connected to the Large Electron Positron collider (LEP) and Tevatron. Limits on the the Higgs mass were also derived from high precision electroweak measurement. Interactions between fermions and Higgs boson in loops contribute to observable quantities such as the W mass. A precise measurement of this quantity gives information about the Higgs boson mass. In particular from the measurement of the Z, W and top quark masses from LEP and Tevatron it was possible to estimate the value of m_H that is in the best agreement with the measurements. In figure 2.1 a χ^2 fit of the Higgs boson that gives the best agreement with the observations.

The minimum of the χ^2 distribution is at $m_H = 89^{+35}_{-16}$ GeV [9] [10]. The fit was redone including also the direct searches of LEP and Tevatron. The best fit value

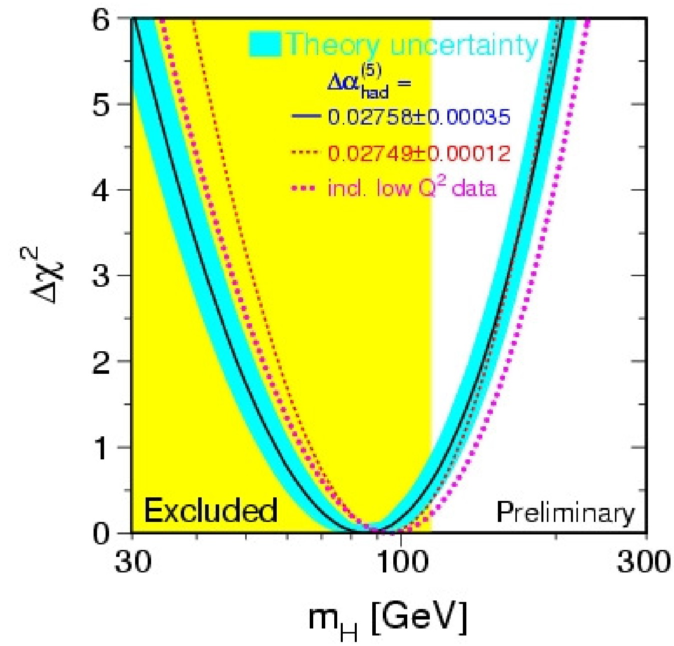

Figure 2.1: Limits on the SM Higgs boson mass from LEP. The yellow band represents the SM Higgs boson mass hypotheses excluded from direct searches while the χ^2 distribution indicates the most probable value for the SM Higgs boson mass parameter.

considering both the direct and indirect searches is at $m_H = 120^{+12}_{-5}$ GeV [11]. This value is in good agreement with the mass of the new boson discovered in the 2012 by the ATLAS and CMS collaborations, discussed in section 2.3. In this chapter the decay modes of the Higgs boson are described (section 2.1) together with the production modes (section 2.2) accessible at the Large Hadron Collider (LHC).

2.1 The Higgs boson decay

According to the predictions of the model the Higgs boson can decay in several modes, with fermions or bosons [12] [13]. Of course the branching ratio (BR) of the several decay modes is different and it is possible to calculate all the BR starting from the Lagrangian described in chapter 1. A dependence from the mass arises both from the mass dependence of the couplings and from the phase space in the Higgs boson decay. In figure 2.2 the Feynman diagrams of the main SM Higgs boson decays are shown while in figure 2.3 the BR of several SM Higgs boson decay channels is reported as a function of the Higgs boson's mass.

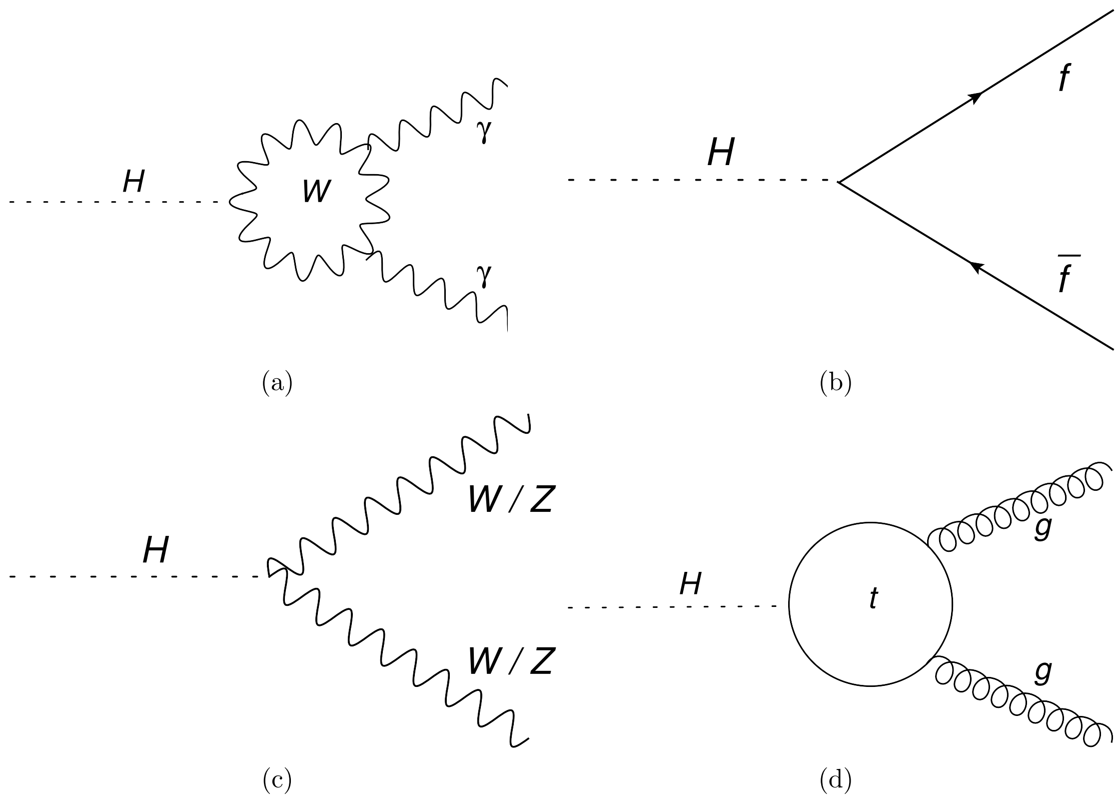

Figure 2.2: SM Higgs boson decay Feynman diagrams. The decay mechanisms are described in 2.1.

As shown in figure 2.3 for a low mass Higgs boson the most probable decay mode is in the $b\overline{b}$ channel. These events are mainly dominated by a large hadronic activity so in an experiment at a hadron collider, such as Tevatron and LHC, this channel is difficult to study because of the high level of background. This is true for all the final state with hadronic activity, including $\tau\tau$ with τ to hadrons, and that's why the most relevant channel for low mass Higgs is the $\gamma\gamma$ decay mode.
The diphoton decay is interesting also because all the final state quantities could be

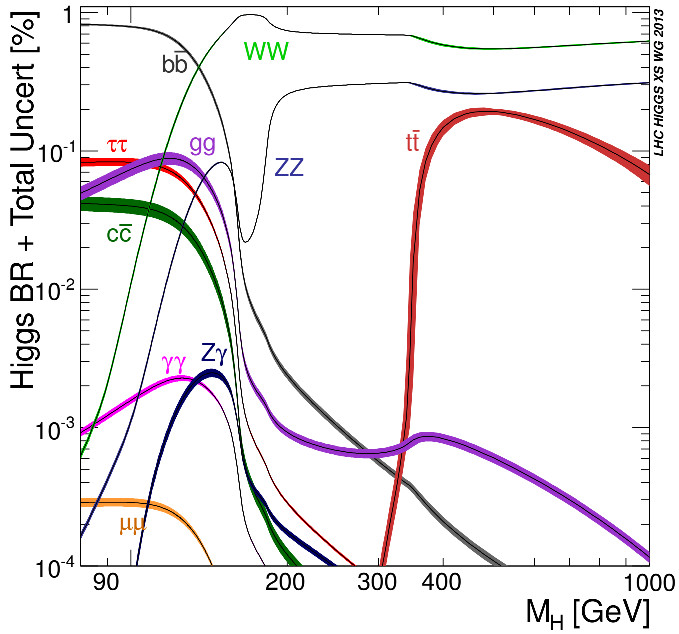

Figure 2.3: SM Higgs boson decays BR as a function of mass. The dependence from the mass arises both from the mass dependence of the couplings and from the phase space in the Higgs boson decay.
(from https://twiki.cern.ch/twiki/bin/view/LHCPhysics/CrossSections)

measured. In particular the Higgs mass could be correctly reconstructed and this is the reason why in this channel the search is focused on a peak in the diphoton invariant mass over the background distribution. For a Higgs boson mass larger than 120 GeV the BR in dibosons final states becomes relevant. In particular these contributions become dominant for $m_H \geq 2m_W$. The WW$^{(*)}$ decay mode is the preferred one for a large mass range but there is an issue with the final state, the two bosons can decay: leptonically (presence of missing transverse momentum due to neutrinos), semileptonically (presence of missing transverse momentum and hadronic activity) or hadronically (presence of hadronic activity). The semileptonic and hadronic final states suffer of huge background contribution so the most powerful channel in the WW$^{(*)}$ is the fully leptonic final state, with electrons or muons. The $H \to WW^{(*)} \to l\nu l\nu$ decay channel is the primary discovery channel for a large Higgs boson mass range but suffers the presence of the missing transverse momentum. Because of the presence of neutrinos is not possible to reconstruct the exact invariant mass. The other diboson decay, the ZZ$^{(*)}$, has a lower BR compared with the WW$^{(*)}$ but plays a great role in the discovery of the Higgs thanks to the fully leptonic final states. The $H \to ZZ^{(*)} \to llll$ channel has a low BR but the topology of the events is clear and reconstructing leptons is experimentally more efficient than reconstructing photons. This final state thanks to the complete reconstruction of cinematic of the events is also useful in the study of several properties of the Higgs boson, such as the spin and CP state. In table 2.1 the BR for the most relevant Higgs boson decay mode at $m_H = 125$ GeV is presented

Branching Ratios (BR) at $m_H = 125$ GeV				
$H \to b\bar{b}$	$H \to WW^{(*)}$	$H \to \tau\tau$	$H \to ZZ^{(*)}$	$H \to \gamma\gamma$
0.577	0.215	0.0632	0.0264	0.00228

Table 2.1: SM Higgs boson BR for a mass hypothesis of $m_H = 125$ GeV.

2.2 The Higgs boson production at LHC

At the LHC collider there are four main Higgs boson production modes. Their cross section depend on the mass and on the center-of-mass energy [12] [13]. In figure 2.4 the cross section of the main Higgs boson production modes as a function of the Higgs boson mass with a center-of-mass energy of $\sqrt{s} = 7$ TeV (a) and $\sqrt{s} = 8$ TeV (b) are presented.

The production mode with the higher cross section, in the whole Higgs boson mass range, is the gluon-gluon fusion (ggf). This is mainly mediated by a top loop as shown in the Feynman diagram figure 2.5 (a). The topology of these events is mainly connected to low hadron activity and this makes the ggf be one of the most important production modes for the Higgs boson studies. The second most relevant production mode is the vector boson fusion (vbf). The vbf has a cross section a factor 10 smaller than ggf in a large m_H range. The Feynman diagram is represented in figure 2.5 (b). Two vector boson (W or Z) are radiated by quarks and fusing to create the Higgs boson. Usually in vbf the Higgs boson is produced in association with two or more jets visible in the detector at large pseudorapidity. At a smaller cross section the Higgs boson associated production with W or Z, also called the Higgs-strahlung. The WH production has a larger cross section than the ZH but both the modes are interesting for low Higgs masses. Both the associated production modes are useful to test the SM predictions because they are sensitive, more than ggf and vbf, to the

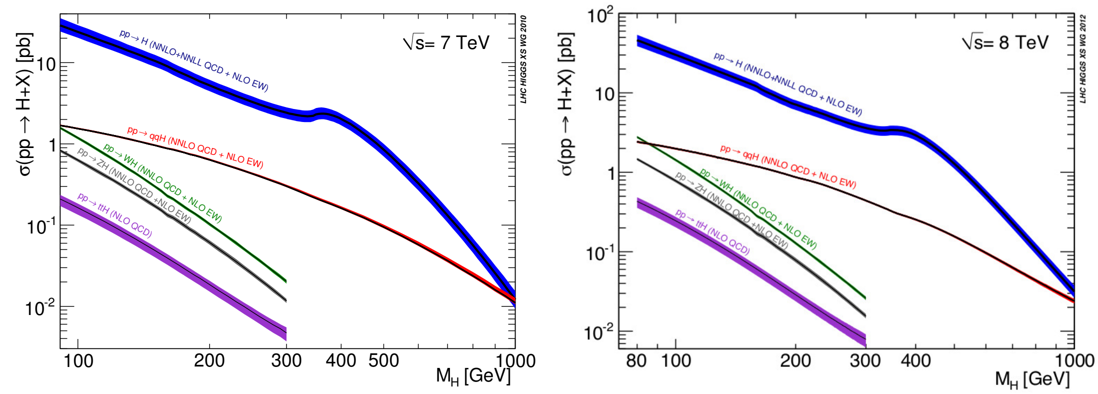

(a) (b)

Figure 2.4: SM Higgs boson production cross section at LHC as a function of the mass with a center-of-mass energy of (a) $\sqrt{s} = 7$ TeV and (b) $\sqrt{s} = 8$ TeV. The production mechanisms are described in 2.2.
(from https://twiki.cern.ch/twiki/bin/view/LHCPhysics/CrossSections)

coupling between the Higgs boson and the vector bosons. In particular considering an Higgs boson's decay in two W bosons, as it will presented in this thesis, the $WH \to WWW^{(*)}$ channel is really sensitive to the coupling between the Higgs and the W bosons and it becomes, after the discovery of a SM Higgs boson like particle made by ATLAS and CMS, an interesting channel to test the SM predictions. The production mode with the smaller cross section, reported in figure 2.2, is the $\mathrm{t\bar{t}H}$. Despite the small cross section, a factor 100 smaller the ggf, this production mode is interesting to test the SM coupling and in particular, as is shown in the corresponding Feynman diagram 2.5 (d), the coupling between the top and the Higgs boson. Due to this coupling the $\mathrm{t\bar{t}H}$ is also useful to test the ggf because this production mechanism, as shown in figure 2.5 (a), occurs via a top-loop.

At $m_H = 125$ GeV about the 87% of the Higgs bosons are produced through the ggf process while only the 7% and 5% are produced via vbf and Higgs-strahlung, respectively. The $\mathrm{t\bar{t}H}$ contribution at this mass is the smallest, about 1%. Table 2.2 presents the cross section in pb for all the production modes for a Higgs boson mass hypothesis of 125 GeV.

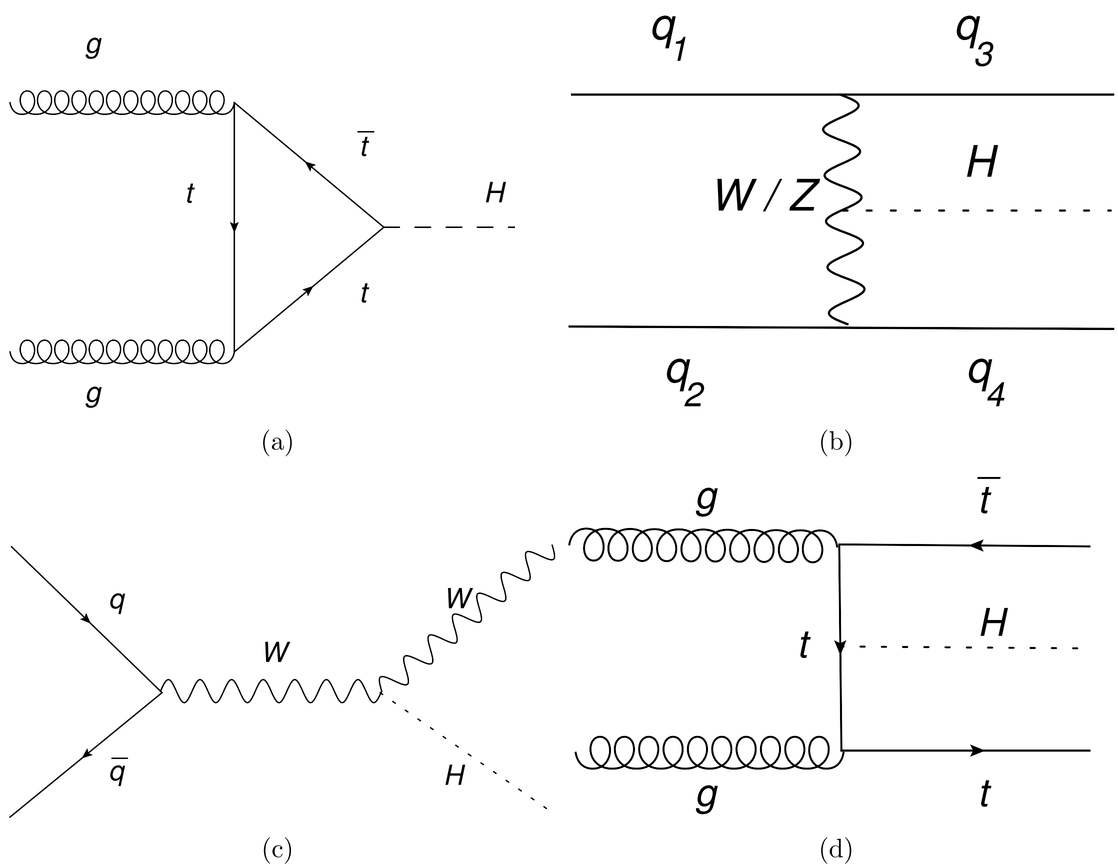

Figure 2.5: SM Higgs boson production at LHC Feynman diagrams. The production mechanisms are described in 2.2.

Higgs boson production Cross Section (pb) at LHC for $m_H = 125$ GeV					
$\sqrt{s}$	ggf	vbf	WH	ZH	$\mathrm{t\bar{t}H}$
7 TeV	15.13	1.222	0.5785	0.3351	0.0863
8 TeV	19.27	1.578	0.7046	0.4153	0.1293

Table 2.2: SM Higgs boson production cross section at LHC for a mass hypothesis of $m_H = 125$ GeV.

2.3 Discovery of a new boson Higgs SM like

In the December 2011 the ATLAS and CMS collaborations reported a first hint of the presence of a new particle in a mass region between 124-126 GeV [14] [15]. Both the experiments observed an excess of events in their data acquired at center-of-mass energy of $\sqrt{s} = 7$ TeV at the LHC. The excesses, which were compatible with the hypothesis of a SM Higgs boson, had significances of 2.9σ (ATLAS) and 3.1σ (CMS). A reanalysis of the events acquired by the CDF and D0 experiments at the Tevatron showed a broad excess in the 120-135 GeV mass region [16] [17]. The observed local significance for the combination of the two experiments at $m_H = 125$ GeV is 2.8σ [18]. On 4 July 2012 both the ATLAS and CMS experiments announced the observation of a new particle in the search for the Standard Model Higgs boson [19] [20]. The discovery is based on 4.6 - 4.8 fb^{-1} and 5.1 fb^{-1} of data acquired in pp collisions at a center-of-mass energy of $\sqrt{s} = 7$ TeV in the 2011 plus 5.8-5.9 fb^{-1} and 5.3 fb^{-1} of data acquired in pp collisions at a center-of-mass energy of $\sqrt{s} = 8$ TeV in the 2012 at LHC by ATLAS and CMS respectively. The two experiments observed a new boson Higgs SM like in a mass range between 125-126 GeV decaying into $\gamma\gamma$, ZZ and WW. In figure 2.6 the exclusion limits at 95% confidence level (CL) for a SM Higgs boson, with mass m_H, computed by ATLAS (a) and CMS (b) are shown. ATLAS has seen an excess in the region 122-131 GeV while CMS observed an excess in the range 121.5-128 GeV.

Figure 2.7 shows the probability, as a function of the Higgs boson mass hypothesis, of a background fluctuation producing, in absence of any signal, a number of events at least as large as the observed one (p_0). Both the experiments observed a minimum in the probability for an Higgs boson mass of about 125 GeV. The observed significance is 5.9σ for ATLAS and 5.0σ for CMS. Both the results allowed the claim of the discovery of a new particle.

The collaborations also started to look into the properties of this particle. The mass measured is $m_H = 125.5 \pm 0.2(\text{stat})\ ^{+0.5}_{-0.6}$ (syst) GeV for ATLAS [21] and $m_H = 125.3 \pm 0.4(\text{stat})$ ± 0.5 (syst) GeV for CMS [20]. The spin value is not yet measured but the spin-1 scenario is excluded by the fact that the particle decays in $\gamma\gamma$. However studies on the spin of that particle were performed by both the experiments and a spin 0 hypothesis seems to be favored with respect to the spin 2 hypothesis. ATLAS reports a combined study of the spin of the Higgs SM like boson observed at LHC [22] that is an update of the Ref.[23]. This study is based on the $H \to WW^{(*)} \to l\nu l\nu$, $H \to ZZ^{(*)} \to llll$ and $H \to \gamma\gamma$ decay channels. The dataset used corresponds to 20.7 fb^{-1} at $\sqrt{s} = 8$ TeV for all the channels but for the $H \to ZZ^{(*)} \to llll$ for which a dataset of 4.6 fb^{-1} of pp collision data at $\sqrt{s} = 7$ TeV

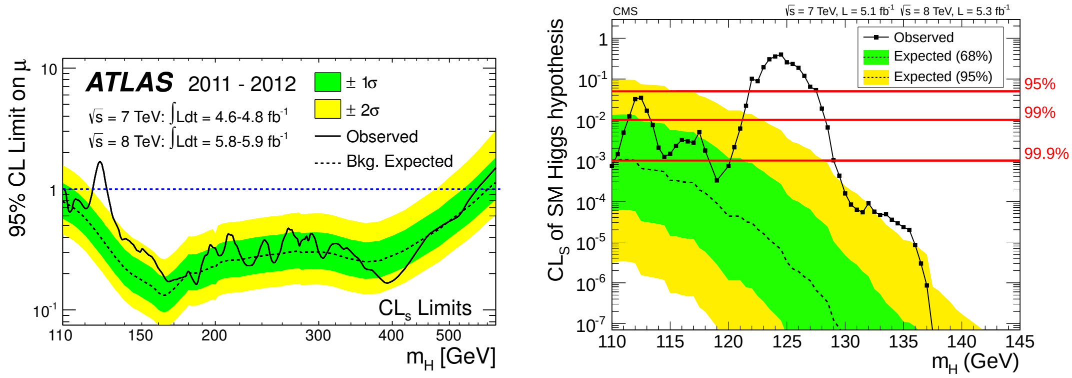

(a) (b)

Figure 2.6: Upper limits at 95% CL$_s$ on the presence of a SM Higgs boson for (a) ATLAS and (b) CMS as a function of mass. The mass region near to 125 GeV is not excluded due to excesses, compared with background-only expectation, observed in both the experiment.

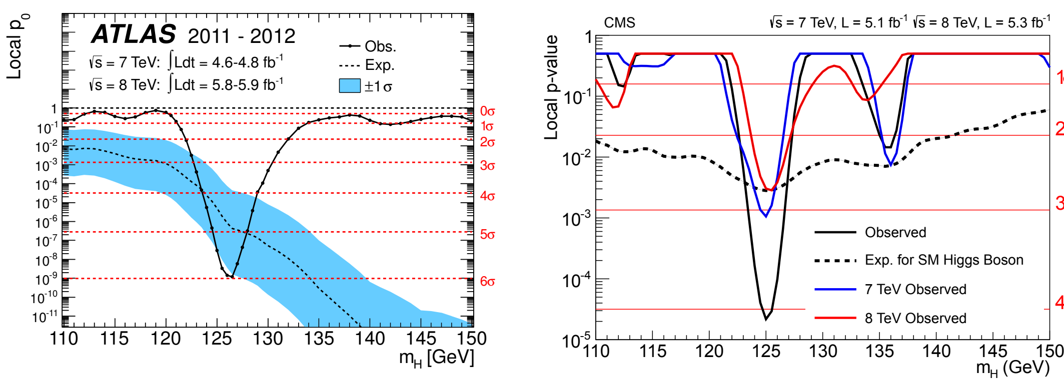

(a) (b)

Figure 2.7: Observed (continuous line) and expected (dashed line) significance of the excesses as a function of the Higgs boson mass for (a) ATLAS and (b) CMS.

is added. In the ATLAS spin analysis the Standard Model assignment of $J^P = 0^+$ is compared with alternative hypotheses namely $J^P = 0^-, 1^+, 1^-, 2^+$. The data are in good agreement with the expected distributions of a SM particle while the alternative models are excluded at confidence levels above 97.8%. In particular the $J^P = 2^+$ model, that is expected to be produced dominantly via the gluon fusion process, is excluded at more than 99.9% confidence level. To establish if the discovered particle is a SM Higgs boson further measurements are needed but all the studies made up to now are in a good agreement with all the SM predictions.

ATLAS published a couplings determination of the SM Higgs-like boson observed using a dataset corresponding to 4.7 fb^{-1} of pp collision data at $\sqrt{s} = 7$ TeV and 20.7 fb^{-1} at $\sqrt{s} = 8$ TeV [21]. This result is presented for the three most sensitive channels $H \to WW^{(*)} \to l\nu l\nu$, $H \to ZZ^{(*)} \to llll$ and $H \to \gamma\gamma$ and it is an update of the results presented in Ref. [24] and in Ref. [25]. The combined measurement of the signal strength for the final states $H \to WW^{(*)} \to l\nu l\nu$, $H \to ZZ^{(*)} \to llll$, $H \to \gamma\gamma$, $H \to \tau\tau$ and $H \to b\bar{b}$, obtained for a mass hypothesis of 125.5 GeV, results in a value of $1.33 \pm 0.14(\text{stat}) \pm 0.15(\text{syst})$. The signal strength ratio between vector-boson fusion and gluon (top) initiated Higgs boson production processes is determined to be $\mu_{VBF}/\mu_{ggf+t\bar{t}H} = 1.4^{+0.4}_{-0.3}(\text{stat})^{+0.6}_{-0.4}(\text{syst})$.

In figure 2.8 a summary of all coupling scale factor measurements in the benchmark models used in the analysis is shown. No significant deviation from the SM prediction is observed in any of the different tested benchmarks.

Similar studies performed by the CMS collaboration lead to results compatible with the ones from ATLAS and with the SM predictions, both for the spin of the new boson and for its production strength [26].

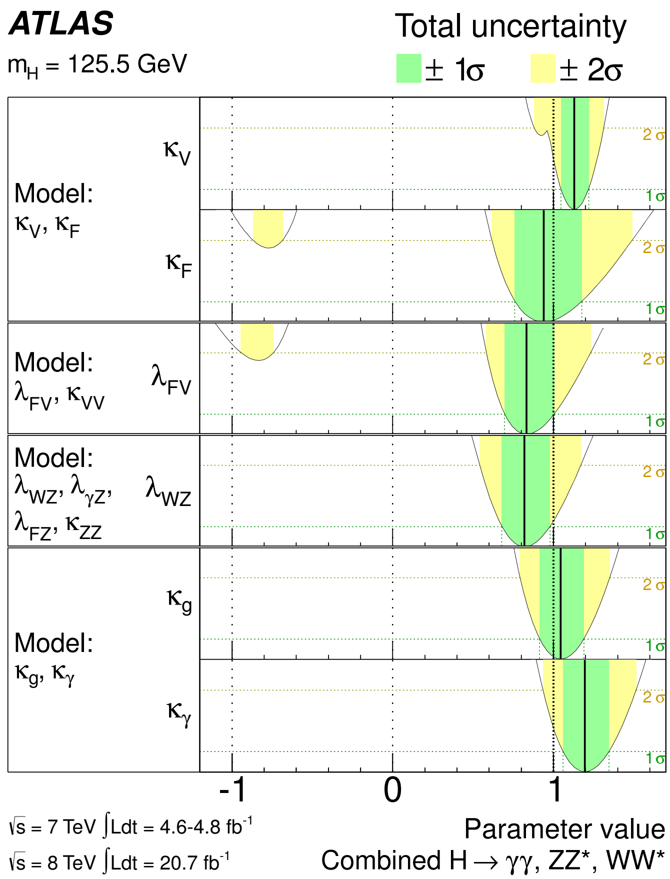

Figure 2.8: Summary of all coupling scale factor measurements performed by ATLAS on the Higgs-like boson observed at LHC. A detailed description of the different factors is reported in Ref. [21].

Chapter 3

The Large Hadron Collider and the ATLAS experiment

The data analyzed in this thesis (chapter 5) were collected in the 2012 by the A Toroidal LHC ApparatuS (ATLAS) [27] [28] [29] experiment. The ATLAS detector is placed on the beamline of the LHC [30], located in Geneva at the European Organization for Nuclear Research (CERN). In this chapter a description of the collider producing the interactions and of the ATLAS experiment are reported. Section 3.1 will focus on the collider properties, on the detectors connected to the LHC and on the whole accelerator complex while in section 3.2 a detailed description of the ATLAS apparatus is reported.

3.1 The Large Hadron Collider (LHC)

The LHC is a proton-proton or Pb-Pb collider located between the France and Switzerland built by the CERN. The accelerator was designed for several purposes, especially to test the validity of the SM and possible extensions. The main goal is connected to the discovery of new particles, such as the Higgs boson (chapter 2), and to the test of theoretical model such as the SM. The LHC is a circular accelerator built in the same tunnel which hosted the LEP, 26.7 kilometers of circumference and about 100 meters beneath the ground. In figure 3.1 a view of the LHC collider with the main experiments located on its beamline is shown.

The Large Hadron Collider is designed to work at the highest center of mass energy never achieved up to now, $\sqrt{s} = 14$ TeV, 7 TeV for each of the two beams. The accelerator ran at $\sqrt{s} = 7$ TeV in the 2010 and 2011 and reached the $\sqrt{s} = 8$ TeV in 2012. The machine is currently shut down and it will be off for about 2 years for

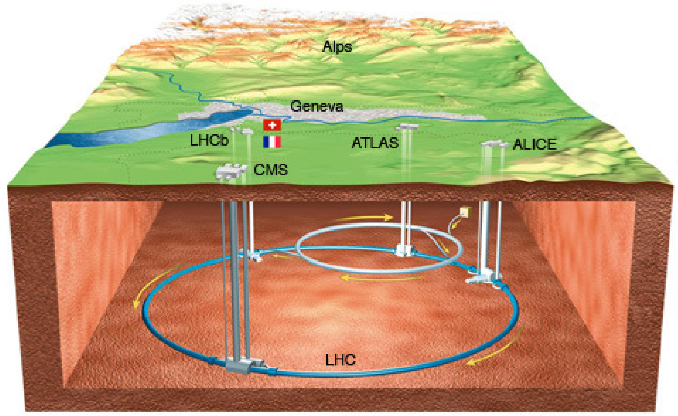

Figure 3.1: View of the LHC collider with the main experiments located on its beamline.
(from http://www.atlas.ch/photos/detector-site-surface.html)

upgrades which will allow it to run at the maximum energy once it will work again, between 2014 and 2015. The LHC is composed by a system of accelerators of which the 27 Km ring is the last step. Figure 3.2 shows the whole accelerator system connected to the LHC.

The protons derived from hydrogen atoms, stripped of their valence electrons, are accelerated in a linear accelerator (Linac2) up to 50 MeV. They are then injected in a circular accelerator, the Proton Synchrotron Booster (PSB) [31]. Here the beam reaches an energy of about 1.4 GeV and it is injected in a larger accelerator, the Proton Synchrotron (PS), where the beam energy rises to 26 GeV. The protons before being injected in the main ring are accelerated in another synchrotron, the Super Proton Synchrotron (SPS) [32]. In the SPS each beam reaches an energy of 450 GeV. The protons in the SPS are also accumulated in bunches to have an higher interaction probability during the collisions. By project the maximum number of protons for each bunch and the number of bunches for each beam are 115 billion and 2808 respectively. At full operation the interactions between the two beams take place at discrete intervals never shorter than 25 ns, with a maximum collision rate of 40 MHz.

One important parameter in the particle experiments is the number of expected events for a given process per unit of time. This number, N_{exp}, depends on two factors: the cross section of the event (σ_{event}) and the integrated luminosity (L):

$$N_{exp} = L \times \sigma_{event} \tag{3.1}$$

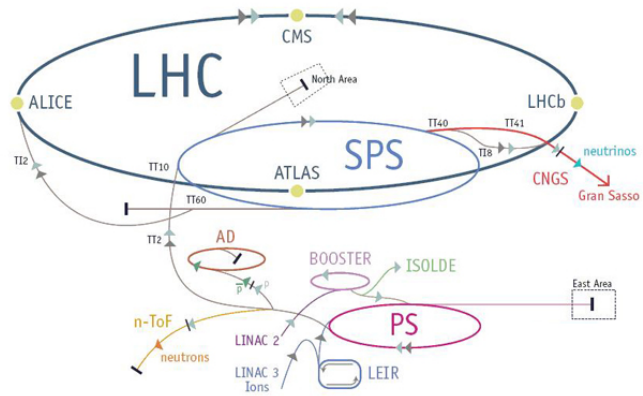

Figure 3.2: View of the LHC accelerator system.

The L is a machine parameter. In figure 3.3 the integrated luminosity for 2011 (a) and 2012 (b) acquired by the ATLAS experiment is shown. The integrated luminosity [33] depends on the live time of the experiment and on the instantaneous luminosity. The instantaneous luminosity (L_{inst}) depends only on the beam parameters and in case of Gaussian beam probability can be written as:

$$L_{inst} = \frac{N_b^2 n_b f_{rev} \gamma}{4\pi \epsilon_n \beta^*} \left\{ 1 + \left(\frac{\theta_c \sigma_z}{2\sigma^*} \right)^2 \right\} \tag{3.2}$$

where

- N_b is the number of protons per bunch
- n_b is the number of bunch per beam
- f_{rev} is the revolution frequency
- γ is the relativistic factor
- ϵ_n is the normalized transverse beam emittance
- β^* is the β function
- θ_c is the full crossing angle at the Interaction Point (IP)
- σ_z is the RMS bunch length

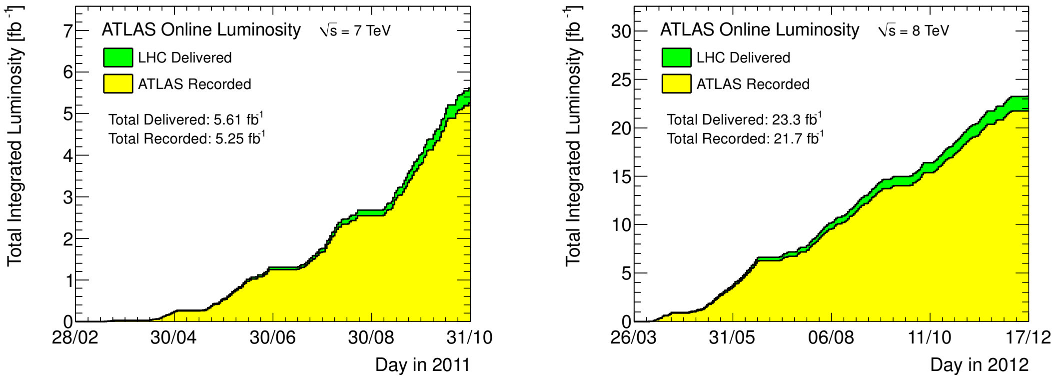

(a) (b)

Figure 3.3: The luminosity delivered by LHC and recorded by ATLAS in (a) 2011 and in (b) 2012.
(from https://twiki.cern.ch/twiki/bin/view/AtlasPublic/LuminosityPublicResults)

- σ^* is the transverse RMS beam size at the IP

The values of the above parameters are summarized for the operating period of 2012 in table 3.1.

The instantaneous luminosity described above does not take into account the loss of intensity during the collisions. In particular the beam intensity decays exponentially as a function of the characteristic decay time τ_L. The integrated luminosity (L_{int}) for a single run could be expressed as a function of the τ_L and length of the run T_{run} as

$$L_{int} = L_{inst}\tau_L \left\{ 1 - exp\left(-\frac{T_{run}}{\tau_L} \right) \right\} \tag{3.3}$$

In the LHC collider the peak instantaneous luminosity, by project, is expected to be $L = 10^{34}\text{cm}^{-2}\text{s}^{-1}$.

One effect visible in runs is the pile-up [34]. This effect is due to either additional proton-proton interactions in the same bunch crossing of the event of interest or to detector signals which occurred a bunch crossing before the event of interest but that are reconstructed later because of the integration time of some detectors. The first one is called "in time pile-up" and it causes a larger number of particles to be produced compared with the expectation in case of a single vertex. In fact because of this effect in the event of interest, several interaction points are produced and

Parameter	Value
N_b	1.6×10^{11}
n_b	1368
f_{rev}	11.25 kHz
γ	4260
ϵ_n	2.5 μm
β^*	0.6
θ_c	290 μrad
σ_z	9.4 cm
σ^*	19 μm

Table 3.1: LHC parameters for the operating period of 2012.

this causes a large multiplicity of collisions and particles per event. The pile-up effect related to the integration time of some detectors is called "out of time pile-up" and it usually affects the signal in calorimeter (section 3.2.4). Because of the out of time pile-up and the signal integration time, the information related to some calorimeter cells may result from the sum of the energy deposited in different bunch crossing. Due to the several interactions occurring in a bunch crossing there are several vertices per event. The vertices located on the beamline axis are called "primary vertices". ATLAS defines as the "primary vertex" the one with the largest value of Σp_T^2 where the sum runs to all the associated charged tracks. The vertices not located on the beamline axis are called "secondary vertices". The secondary vertices are in general related to heavy hadron decays because these particles have a short lifetime and decay before escaping the detector. The out of time pile-up effect on the reconstructed calorimeter information is estimated using simulations and cross-checked with data while the in time pile-up effect is suppressed checking the origin of the particles using tracks. In figure 3.4 the number of interactions per bunch crossing in the 2011 and 2012 years are shown.

The whole accelerator is composed by several superconducting magnets: 1232 dipoles and 392 quadrupoles. The firsts one are the system that bends the charged particles path during the not linear parts of the collider while the second are mainly connected to the focusing of the beam. The nominal field strength is of 8.33 T and it's generated by an electric current 11.700 A for each dipoles. The magnets work at a temperature of 1.9 K obtained using superfluiding hydrogen for the cooling. In figure 3.5 a projection of the LHC magnets, dipoles (a) and quadrupoles (b) is shown.

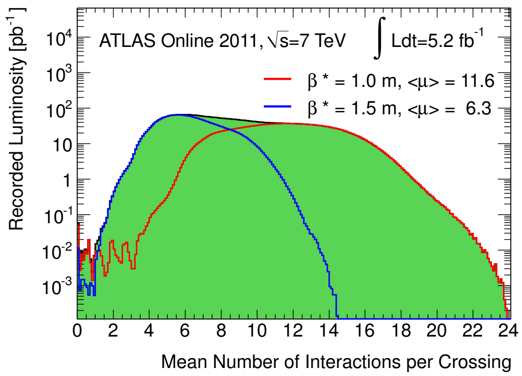

(a)

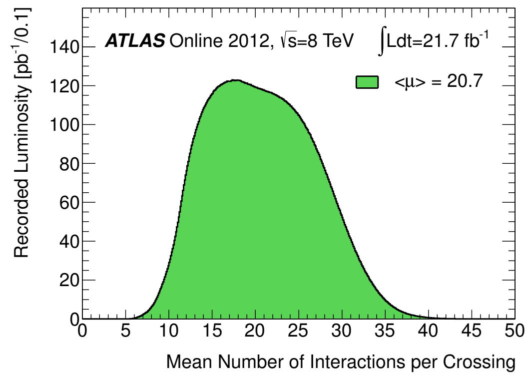

(b)

Figure 3.4: Number of interactions per bunch crossing in the (a) 2011 and (b) 2012 years.
(from https://twiki.cern.ch/twiki/bin/view/AtlasPublic/LuminosityPublicResults)

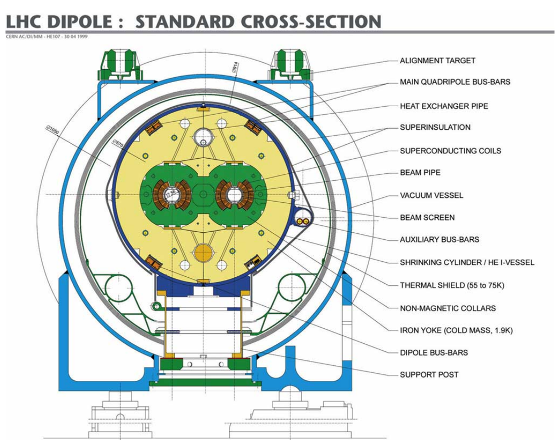

(a)

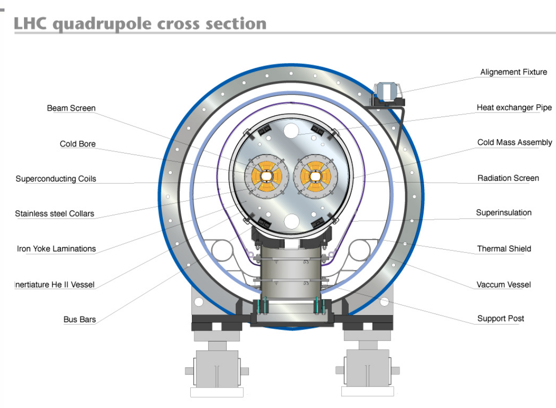

(b)

Figure 3.5: Cross section of the LHC dipoles (a) and quadrupoles (b).
(from http://www.atlas.ch/photos/lhc.html)

Connected to the LHC collider there are four main particle experiments:

- ATLAS [27]: one of the two general purpose detectors. A detailed description of the apparatus is given in section 3.2.
- Compact Muon Solenoid (CMS) [35]: together with ATLAS a general purpose detectors.
- Large Hadron Collider Beauty (LHCb) [36]: the main goal is to study the physics of the B-mesons and measure the CP violation parameters. It operates during the proton-proton collision period.
- A Large Ion Collision Experiment (ALICE) [37]: the main goal is to study the quark-gluon plasma. It's designed to study the Pb-Pb collisions. In the LHC accelerator during the Pb-Pb collisions period each nucleon reaches an center-of-mass energy of 2.76 TeV.

The location of the experiments around the ring of the collider is shown in figure 3.6 while in figure 3.7 a view of CMS (a), LHCb (b) and ALICE (c) is presented.

Together with these experiments there are three other detectors devoted to special purposes:

- TOTal Elastic and diffractive cross section Measurement (TOTEM) [38]: the main goal is to study the total proton-proton interaction cross section. It also studies the elastic scattering and the diffractive processes.
- Large Hadron Collider forward (LHCf) [39]: the main goal is to study the energy and the momentum of the neutral pions produced by the collider. These results are of particular interest for the modeling of the atmospheric showers.
- Monopole and Exotics Detector At the LHC (MoEDAL) [40]: the main goal is to search for the magnetic monopole and other highly ionizing stable massive particles at the LHC.

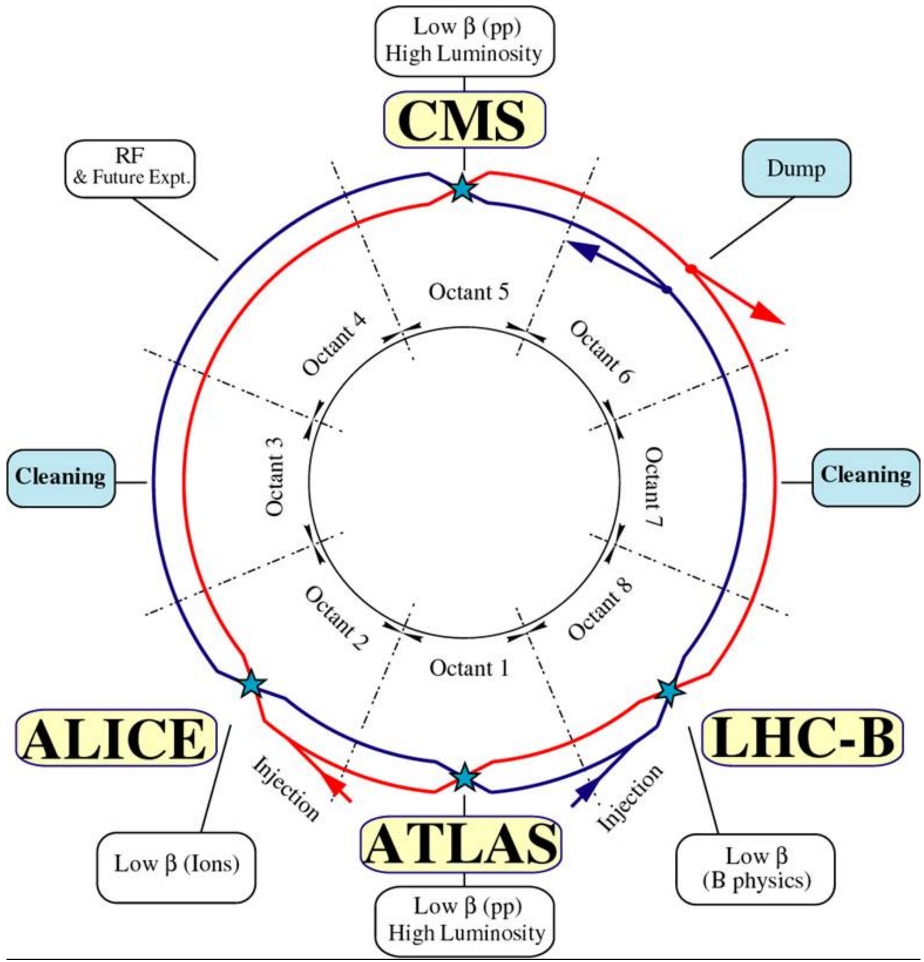

Figure 3.6: Location of the experiments around the LHC ring.

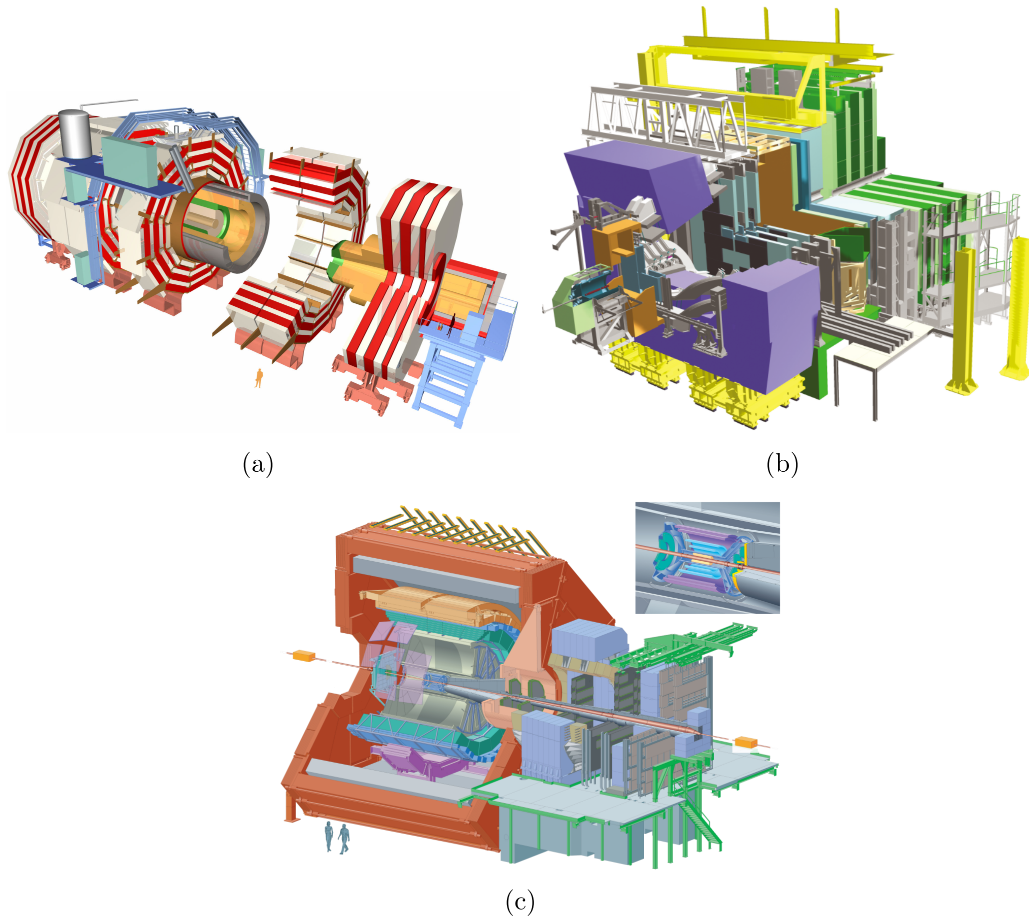

Figure 3.7: View of the CMS (a), LHCb (b) and ALICE (c) experiments.

3.2 The ATLAS experiment

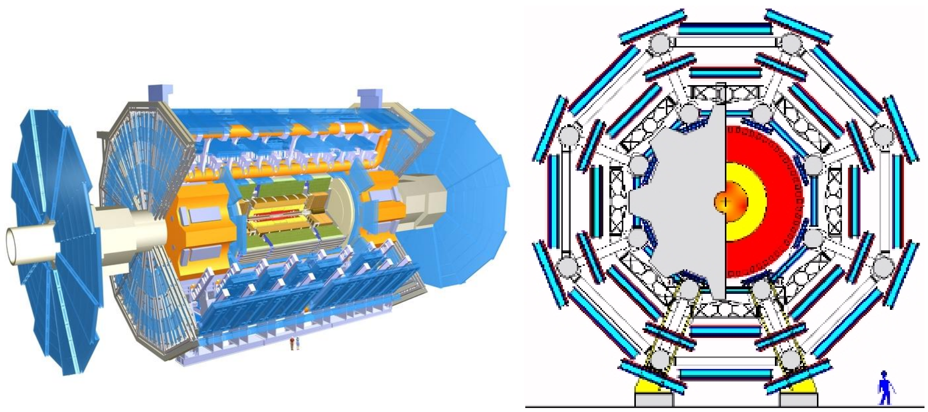

(a) (b)

Figure 3.8: The longitudinal (a) and the cross section (b) views of the ATLAS experiment.

The ATLAS [27] experiment is located at the cavern Point 1 at CERN and, together with CMS, is one of the two general purpose detectors. It is built to study several different processes and probe theories, as SM and Supersymmetry. This experiment, with its 44 meters length, 25 meters high and a weight of 7000 tons is the largest experiment connected to the LHC. It is an hermetic (4π) coverage detector built to satisfy several physics and hardware constraints, mainly:

1. Radiation-hard and fast electronics elements and detectors stand to the high luminosity condition.
2. Detectors with high granularity to limit overlap between different events or different particles of the same event.
3. High trigger efficiency for both high and low transverse momentum objects.
4. High reconstruction efficiency and resolution for charged particles tracking, crucial for the inner detector where the experiment should be capable to distinguish between primary and not primary vertices.
5. Good momentum resolution for the muons in the muon spectrometer up to $p_T \sim 1$ TeV.

6. Calorimeter system able to discriminate between electrons and photons.

7. Full-coverage calorimeter system to measure the jet and the missing transverse momentum, useful in most of the interesting physics processes.

To satisfy all these requirement the ATLAS experiment is constructed using several sub-detectors. Starting from the beam line going outwards:

- Inner Detector (section 3.2.3): for vertices and tracks reconstruction.

- Calorimeter system (section 3.2.4): composed by two sub systems, an Electro-Magnetic (EM) part to measure the EM particle energy and a hadronic part to measure the hadrons energy.

- Muon Spectrometer (section 3.2.5): for muons identification and reconstruction.

In the ATLAS experiment there are also a magnetic system that ensures the bending of charged particles (section 3.2.2) and a trigger system that allows fast selection of interesting events (section 3.2.6).

3.2.1 Coordinate System

The coordinate system of ATLAS is chosen such that the origin is in the center of the detector at the nominal collision point. The z-axis coincides with the beam line and the positive part has the same direction of the beam moving anti-clockwise. The x-y plane is transverse to the beam line and it divides the apparatus in two sides: A-side (positive z) and C-side (negative z). The positive x axis points to the center of the LHC collider while the positive y axis points upward. The coordinate system of the ATLAS detector is drawn in figure 3.9.

Usually in the analysis an alternative coordinate system that uses the polar angle (θ), the azimuthal angle (ϕ) and a variable R is adopted. It is defined with:

$$R = \sqrt{x^2 + y^2} \tag{3.4}$$

$$\phi = tan\frac{y}{x} \tag{3.5}$$

$$\theta = arcos\frac{z}{\sqrt{R^2 + z^2}} \tag{3.6}$$

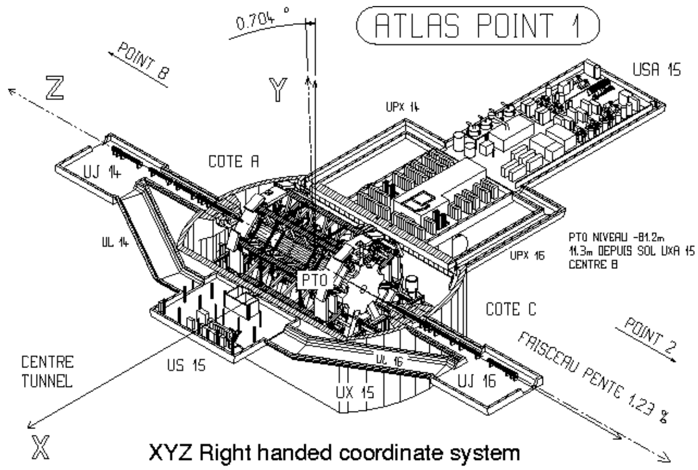

Figure 3.9: ATLAS Coordinate System.

For relativistic particles instead of the polar angle another quantity is used, the pseudo-rapidity (η) defined as:

$$\eta = -\ln tan\left(\frac{\theta}{2}\right) \tag{3.7}$$

The ATLAS apparatus is divided in three regions along η, a central part (barrel) and two extreme ones (endcap):

- Barrel for $|\eta| < 1.05$
- Transition region for $1.05 < |\eta| < 1.4$
- Endcap for $|\eta| > 1.4$

3.2.2 Magnetic System

The ATLAS Magnetic System is composed by four magnets. One solenoid, the Central Solenoid (CS) [41], is located in the barrel outside the Inner Detector (ID) and in front of the calorimeter system. It works at a temperature of 4.5 K and it creates a magnetic field of 2 T (2.6 T of peak value). The CS is needed for the momentum measurement of the particles tracked in the ID and it is designed to minimize the materials to reduce the multiple scattering and the energy loss that can affect the momentum and the energy measurements. The final dimensions are

5.8 m length, an internal diameter of 2.4 m and an external diameter of 2.6 m, for a total number of radiation lengths of 0.66. In the barrel there is also another magnet, a cylindrical toroid constructed to provide the magnetic field to the Muon Spectrometer (MS) [42]. It's located after the calorimeter system and it's composed of eight parts as shown in figure 3.10. The produced magnetic field is about 0.5 T and the dimensions are 25.3 m for the length, 9.4 m the internal diameter and 20.1 m the external diameter. The other two magnets are small toroids located in the endcap regions, one for each side, producing a 1 T magnetic field [43] [44]. The dimensions are 5 m for the length, 1.65 m the internal diameter and 10.7 m the external diameter.

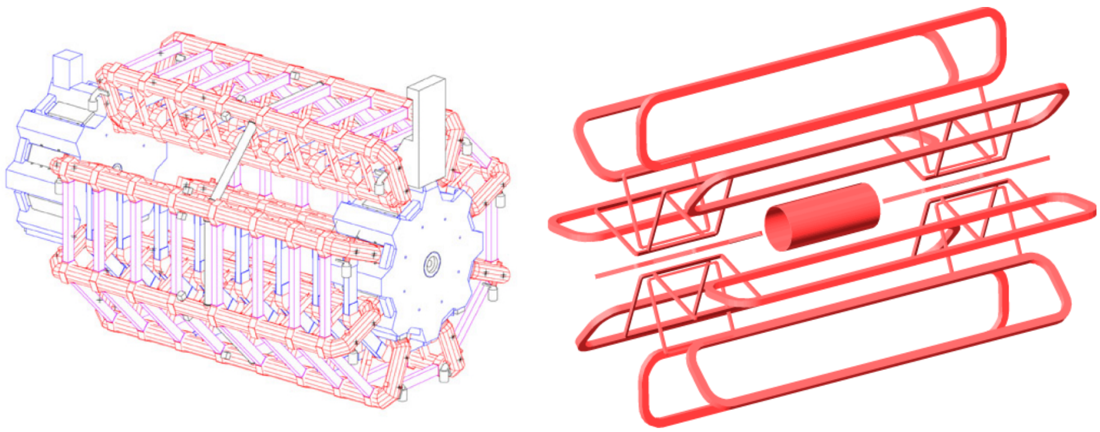

(a) (b)

Figure 3.10: The ATLAS magnets system.

3.2.3 Inner Detector

The ID [45] [46], is the detector nearest to the collision point, it provides precise measurements of the momentum, impact parameter of charged particles and the vertices reconstruction. All these measurements are obtained thanks to the high granularity that allows to discriminate between the about a hundred particles traveling into the detector after the bunch crossing. The ID works in a 2 T magnetic field produced by a solenoid superconducting. The detector is instrumented with three technologies:

- Pixel: the innermost detector is also the subdetector with the highest granularity [47]. It is composed by three concentric cylindrical layers in the barrel and 3 disks for each endcap. From the collision point the radii of the cylindrical layers are about 5.05 cm, 8.85 cm and 12.25 cm while the 6 disks of the endcaps are located, in the z direction, between 11 cm and 20 cm on each side of the interaction point. The pixel size is 50×400 μm^2 and they allow to achieve a resolutions of 10 μm in the $R\phi$ plane and 115 μm in z for the barrel and 10 μm in the $R\phi$ plane and 115 μm in R for the endcap.

- SCT: it is composed by four cylindrical layers in the barrel and 9 disks for each endcap part [48]. From the collision point the radii of the layers are about 30.0 cm, 37.3 cm, 44.7 cm and 52.0 cm while the disks of the endcap parts are located, in the z direction, between 85 cm and 272 cm for each side. The SCT is composed by silicon strips of 80 μm that give just one dimensional measurement. All the layers are composed by a pair of strips, one parallel to the beam line and the other with an angle of 40 mrad compared to the first one to obtain a two dimensional measurement. The resolution is 17 μm in the $R\phi$ plane and 580 μm in z for the barrel and 17 μm in the $R\phi$ plane and 580 μm in R for the endcap.

- TRT: it is composed by drift tubes with a 2 mm radius aligned parallel to the beam line in barrel and perpendicular to it in the endcap. The tubes are filled with a gas mixture of $Xe : CO_2 : O_2 = 70 : 27 : 3$ that ionizes when a charged particle cross it [49]. The TRT is useful to discriminate between electrons and hadrons. The transition radiation (TR) is connected to the speed of a particle. Comparing electrons and hadrons the first one are lighter and so they have an higher speed and emit more TR. The barrel part covers the radii from 56 cm to 107 cm while the endcap is composed by 18 disks.

The Pixel and SCT detectors cover a pseudorapity $|\eta| < 2.5$ while the TRT covers only $|\eta| < 2$. Two views of the ID are shown in figure 3.11.

3.2.4 Calorimeter system

The ATLAS calorimeter system [50] [51] is divided in an inner electromagnetic (EM) layer and another hadronic one. The main goal of the EM calorimeter is to measure, whit high precision, the energy of photons and electrons while the hadronic calorimeter system is mainly focused on jets energy measurement. All the systems use sampling calorimeters, detectors in which particles cross alternatively inert and active materials. The active material used is liquid argon (LAr) for most of the calorimeters while the absorber material depends on the region in which the detector is located. The choice of LAr is connected to its performance and in particular

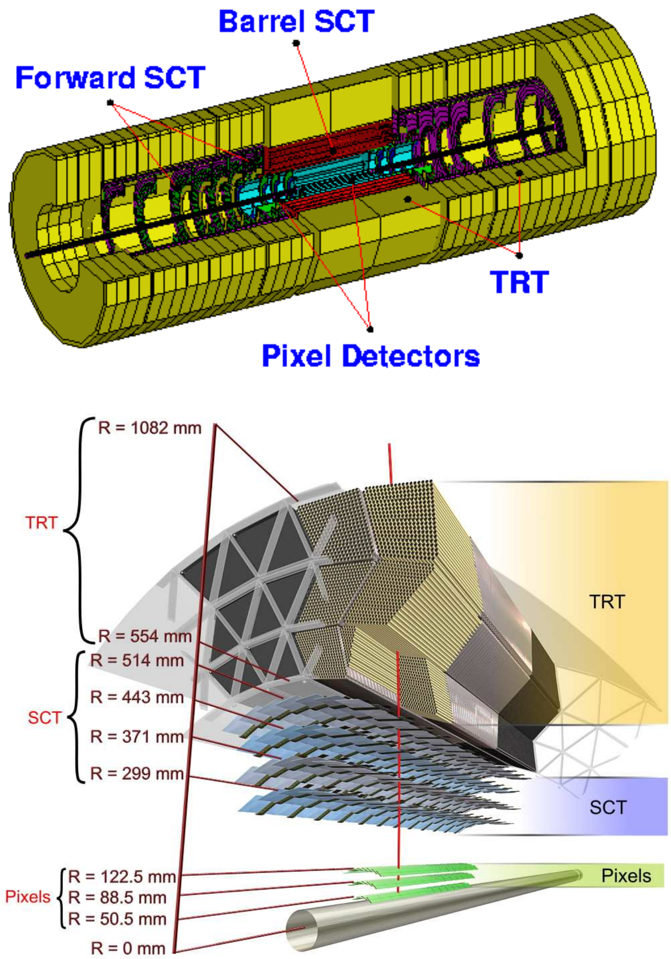

Figure 3.11: Two views of the ATLAS Inner Detector.

to the linearity of the signal, the fast response and the radiation hardness (in ten years of activity the calorimeter system will receive more than 300 KGy of radiation). The EM calorimeters are divided in barrel (EMB) and endcap (EMEC). The EMB is composed by 3 layers and a presampler (to correct for the energy loss in the material in front of the calorimeter). The EMB uses LAr as active material and lead as absorber and all the system covers a pseudorapidity of $|\eta| < 1.475$. The first layer has the best granularity in η while the second provides the best position in ϕ. The number of radiation lengths in the EMB is 24 X_0. The EMEC calorimeters are made with the same material of the EMB but the number of radiation lengths in the endcap is larger, 26 X_0. In the endcaps the EM is composed of two concentric wheels covering the range $1.375 < |\eta| < 3.2$. The hadronic calorimeter system is located after the EM calorimeters. As the EM it is divided in a barrel (TileCal) and two endcaps (HEC). TileCal is composed by steel, as absorber, and plastic scintillators as sampling material. The number of interaction lengths in the TileCal is 8 λ, enough to ensure a complete measurement of the jet energy. The TileCal, as the EMB, is divided in three layers with thickness of 1.5, 4.1 and 1.8 interaction lengths for $|\eta| < 1.0$ and 1.5, 2.6 and 3.3 interaction lengths up to $|\eta| = 1.7$. The HEC is composed of LAr and copper and it covers up to $|\eta| < 3.2$. It's divided in two wheels for each endcap. In the endcap regions the total number of interactions lengths (including the EMEC) is 12 λ.

To cover pseudorapidity larger than $|\eta| > 3.2$ another calorimetric is used, the forward calorimeter (FCAL). FCAL is composed by one EM and two hadronic calorimeters and covers between $3.1 < |\eta| < 4.9$. The number of interaction lengths is about 10 λ. The ATLAS Calorimeter System is shown in figure 3.12.

3.2.5 Muon Spectrometer

The Muon Spectrometer (MS) [52] is the outermost detector of the ATLAS apparatus. It is composed by four different technologies, two connected to the trigger and two connected to the precise tracking. The MS is built to reconstruct the muon trajectories and measure the muon momentum independently from the ID and to provide the trigger for muons. The spectrometer operates under a magnetic field orthogonal to the muon trajectory. The magnetic field bends the trajectory of particles and, according to the arc of the muon track, allows to measure the particle momentum. The four subdector technologies composing the MS are:

- Muon Drift Chamber (MDT)
- Resistive Plate Chamber (RPC)

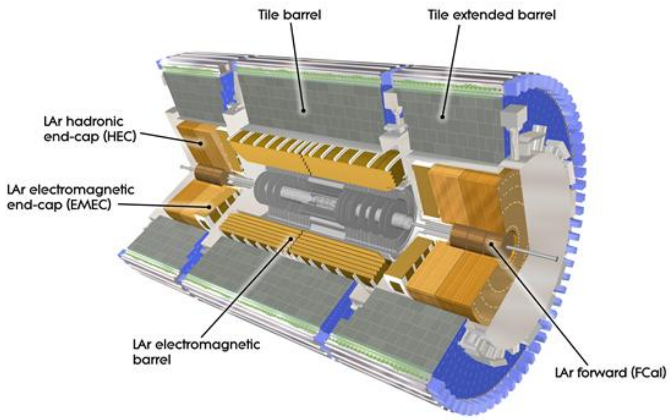

Figure 3.12: The ATLAS Calorimeter System.

- Cathode Strip Chamber (CSC)
- Thin Gap Chamber (TGC)

The MDT and CSC are the chambers used for the tracking and momentum measurement while the RPC and TGC are the trigger chambers providing also an additional measurement of the non bending coordinate in the non bending projection. The detectors in the barrel region are located on three concentric layers at a distance from the collision point of 5 m, 8 m and 10 m respectively, while in the endcap there are three wheels at a distance of 7.5 m, 14 m and 22.5 m from the interaction point. A MS view is shown in figure 3.13. In the following a description of the four technologies used in the MS is reported.

1. The MDT: the MDT system is composed by 1088 chambers for about 339 k readout channels. Each chamber is made by two multi-layers of three or four (only in the innermost chambers) layers of tubes with 3 cm diameter and 400 μm thick aluminum walls. The gas mixture is 93%Ar+7%CO_2+10^3ppmH_2O operating at 3 bar pressure and at 3040 V. The MDT are located in both the barrel and endcap regions. In the barrel, $|\eta| < 1.3$ the chamber are divided in 16 sectors along Φ. In each sector there are large and small chambers. This allow a full coverage and an overlap between chambers that ensure a robust muon momentum measurement. In the endcap the MDTs cover the region $1.3 < |\eta| < 2.4$ and are not used near the beam pipe because of the huge flux

of particles, larger than the acceptable counting rate (about 150 Hz/cm^2). In both the regions, barrel and endcap, the MDT tubes are oriented perpendicular to both the beam pipe and the radial axis to measure the muon track curvature, occurring in the rz plane. MDT stands for Monitored Drift Tubes, where Monitored refers to the carefully monitored alignment, through a continuously readout RASNIK system. A MDT and RASNIK system view is shown in figure 3.14.

2. The RPC: the RPC are used in the barrel for $|\eta| < 1.05$. 544 chambers are located in three concentric layers connected to the MDT. Every chamber has 2-layers of gas gap filled with a gas mixture of $94.7\% C_2H_2F_4 + 5\% \mathsf{iso} C_4H_{10} + 0.3\% SF_6$, where the last one is added to limit the charge avalanches in the chamber. The chambers are made with bakelite plates of 2 mm and readout strip with pitches of about 3 cm. The RPCs work at 9.8 kV and have a time resolution of 1.5 ns.

3. The CSC: the CSCs are multiwire proportional chambers located between $2.0 < |\eta| < 2.7$. They are designed to provide high granularity in an apparatus region near to the beam pipe. The acceptable counting rate of the CSCs is larger than for the MDTs, 1000 Hz/cm^2 instead of 150 Hz/cm^2. This choice is made to be safe in a region with a really high flux of particles. The CSCs are divided in 16 sectors for each of the three wheels, 8 small and 8 large. The chambers, composed by four layers, are in overlap to ensure no loss of information. The chatode strips are mounted in the η - ϕ plane such that the muon track position will be measured by the interpolation of the induced charges in different strips of the layers. The gas mixture is $80\% Ar + 20\% CO_2$ and the typical spatial resolution is 40 μm in the magnet field direction and 5 mm in the azimuthal direction while the time resolution is about 7 ns.

4. The TGC: The TGCs are multiwire proportional chambers dedicated to the trigger system on the endcap part of the ATLAS detector. They cover the forward region in the pseudorapidity range $1.05 < |\eta| < 2.7$. The TGCs, like the RPCs, provide also a measurement of the muon track coordinate orthogonal to the one provided by the precision tracking chambers. The nominal spatial resolution for the TGC it's 3.7 mm in the $R - \phi$ plane. The TGC system is divided in 4 layers, one innermost (TGI) and three in the endcap (TGC1, TGC2 and TGC3). The TGCI covers $1.05 < |\eta| < 1.92$ while the others TGC layers cover up to $|\eta| = 2.7$. TGC1 is composed by three chambers while TGC2 and TGC3 are composed by two chambers. The gas mixture used for

these chambers is $55\% CO_2 + 45\% nC_5H_{12}$ and they work at 2.9 kV. The time resolution is about 4 ns.

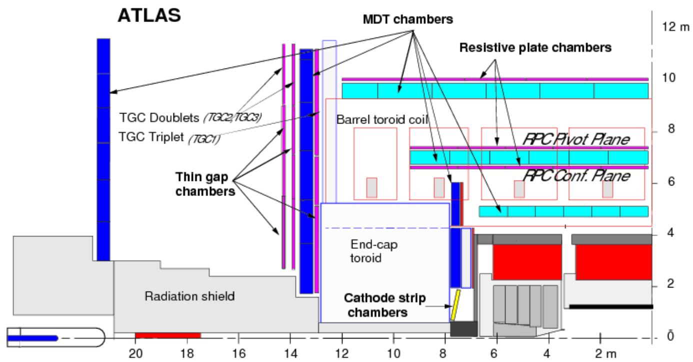

Figure 3.13: The ATLAS Muon Spectrometer.

3.2.6 Trigger System

As described in section 3.1 the designed instantaneous luminosity at LHC is $L = 10^{34}$ cm^{-2}s^{-1} with a collision every 25 ns corresponding to a bunch crossing frequency of 40 MHz. In ATLAS each event digitized needs a storage size of about 1.5 MB, this means an enormous amount of information during the collision period. With the actual technologies the data exceed the recording capability by several orders of magnitude. The trigger system [53] reduces the number of events to be recorded to a manageable number, from the nominal 40 MHz to about 300 Hz.

The system is shown in figure 3.15 and it is divided in

- Level 1 (L1) trigger based on hardware information. It uses information from the MS and the calorimeters. In particular the L1 selects events with electrons, photons, jets, missing transverse momentum and muons using energy thresholds. The information connected to the muons is taken from the RPC and TGC of the MS while the information connected to the energy deposits in the calorimeters is taken from towers in the calorimeter system. Each trigger tower has dimensions $\Delta\eta \times \Delta\phi = 0.1 \times 0.1$. All the L1 information are stored in Region of Interest (RoI) that are analyzed from the High Level Trigger (HLT) composed by the L2 and the Event Filter. The L1 has a maximum latency of 2.5 ms and it reduces the event rate from 40 MHz to 75 KHz.

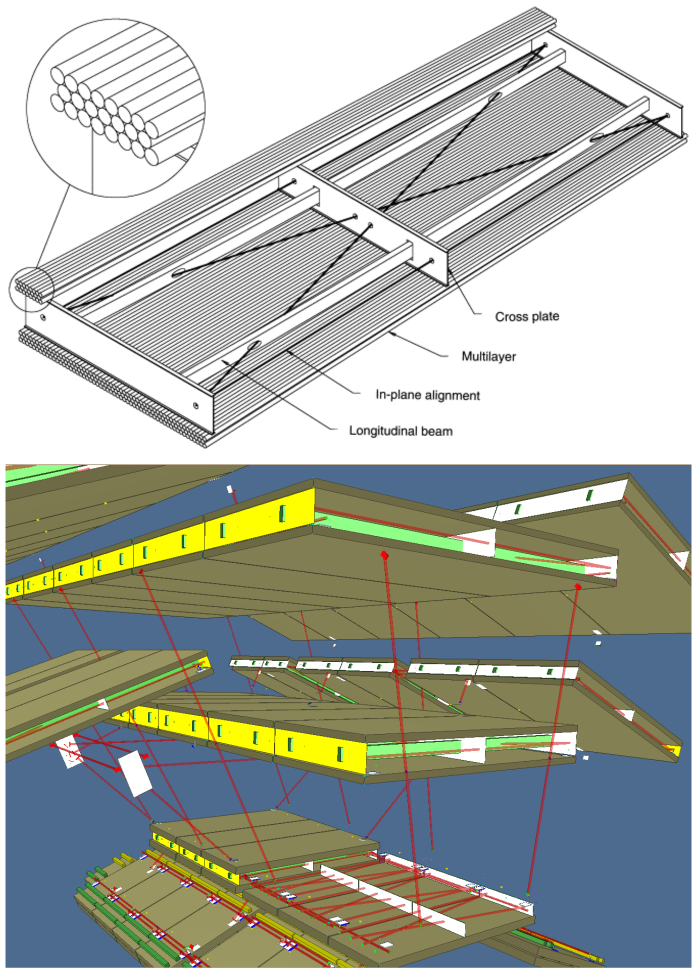

Figure 3.14: The ATLAS MDT (a) and RASNIK system (b) used for MDT alignment.

- Level 2 (L2) trigger is based on software algorithms elaborating the information of different regions (RoI) stored by the L1. All the events at this stage are partially reconstructed by an Event Builder and sent to the the Event Filter. The L2 reduces the event rate to about 5 kHz.

- Event Filter (EF) is based on software algorithms and it decides, according to the information acquired by the L2, if the event should be stored for offline analysis or not. To do this selection the EF fully reconstructs the events passing the first two trigger levels. The final rate of the trigger system is about 300 Hz. When events pass certain sets of criteria in the EF they are written into specific trigger stream. The different trigger stream are connected to the different physics signature of the events and they can be used by different offline analysis according to the study to be performed. For example the analysis described in chapter 5 is based on fully leptonic final states and in particular on final states with electrons and muons. This means that for the analysis the electron and muon streams will be used.

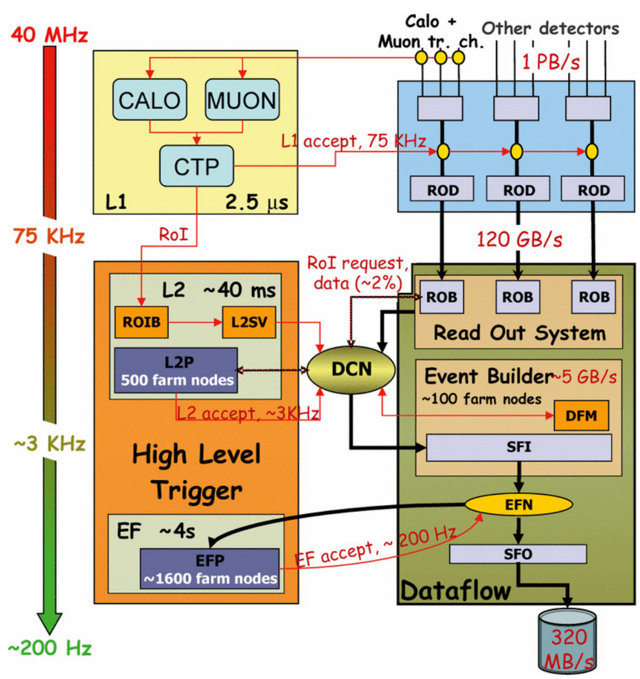

Figure 3.15: The ATLAS trigger system.

Chapter 4

Object Reconstruction

Before going into the details of the analysis it is useful to introduce how the physical objects are reconstructed in the ATLAS detector. In particular in the ATLAS apparatus, information from several sub systems could be used alone or combined to derive the properties of physical objects. For example a physical object to be called electron should have a track in the ID and a corresponding energy deposit in the EM calorimeter system. In high luminosity collision environment there are thousands tracks left by particles traveling through the detector. Also in the EM calorimeter, because of the high number of particles, several energy deposits can be in overlap. Due to the high number of tracks and hits it is possible to reconstruct fake particles clustering together, in a single object, information from different particles.

The performance is measured through two parameters: the reconstruction efficiency and the purity. The reconstruction efficiency is the probability to successfully reconstruct a candidate object while the purity (or fake rejection efficiency) is the probability of a reconstructed object to be a real object and not to be a fake one. In this chapter we will focus in the reconstruction of the objects used in the WH analysis: vertex, tracks, electrons, muons, jets and missing transverse momentum. In particular in section 4.1 the vertex and track reconstruction in the ATLAS detector will be reported while electron and muon objects are described in section 4.2 and 4.3 respectively. In section 4.4 the jets reconstruction algorithms are presented while in section 4.5 the reconstruction of missing transverse momentum is detailed.

4.1 Tracks and vertex Reconstruction

Charged particles traveling in the ATLAS apparatus leave series of hits in the different subdetectors of the ID (section 3.2.3). The hits of Pixel, SCT and TRT are

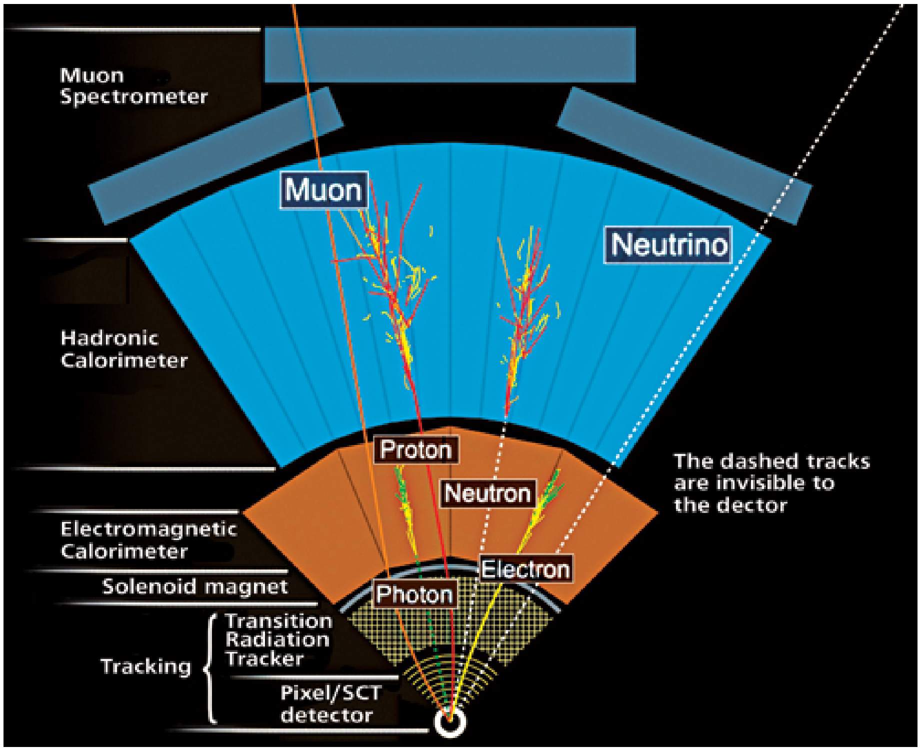

Figure 4.1: Particles detection in ATLAS.
(from http://www.atlas.ch/photos/how-atlas-works.html)

reconstructed into tracks. The reconstructed tracks are used to reconstruct vertices and to identify the primary vertex (PV). In the ATLAS's ID the track reconstruction is split in several steps, taking into account information from different detectors. In the first step seed tracks are reconstructed using the Pixel and SCT information. In particular the three layers of the pixel detector and the first SCT layer are used. The seeds are then extended through all the SCT layers to collect additional hits, tracks are then reconstructed again. To remove fake tracks and solve the ambiguities between clusters shared by tracks at this stage a score is computed for each track. Tracks with few hits and not passing quality criteria are rejected. The remaining tracks are extended to the TRT to collect new hits and the tracks are refit with the new information. Once the tracks are computed using all the information of the ID they can be used for other reconstruction process, including electron (section 4.2) and muon (section 4.3) identification. In the ATLAS detector the vertices are reconstructed associating the reconstructed tracks to a particular vertex candidate and performing a fit to determine the exact vertex position. In the fit a covariance matrix is computed to check the quality of the fits. The ATLAS collaboration implemented two approaches to find the vertex: "fitting-after-finding" and "finding-trough-fitting" [54] [55]. The first clusters the tracks according to their z-impact parameter position. The clusters are then fitted and iteratively cleaned from outliers. With the "fitting-after-finding" the number of vertices is fixed at the seeding stage. The tracks rejected from a given vertex candidate are not used in any other vertex reconstruction. In the "finding-trough-fitting" approach after a selection of tracks, a single vertex seed is created fitting these tracks. The tracks considered outliers in the first fit are used to create a second vertex seed and the two seeds are fitted simultaneously. The two vertices during the second fit compete to obtain more tracks. This is an iterative procedure and the number of vertices is not fixed a prior.

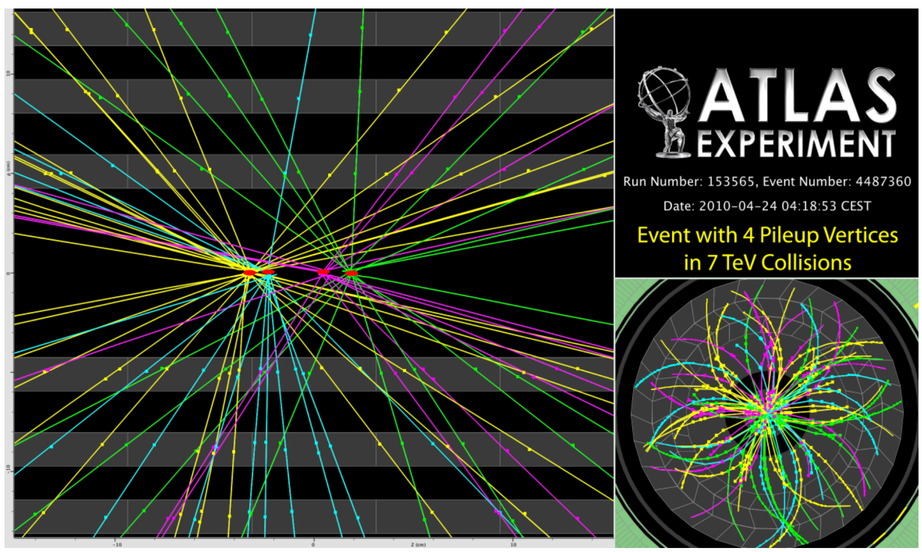

Figure 4.2: The vertex reconstruction in ATLAS allows to associate each charged particle to the interaction also in presence of multiple interactions.
(from https://twiki.cern.ch/twiki/bin/view/AtlasPublic/EventDisplayPublicResults)

4.2 Electrons

An electron is a charged particle that leaves hits in the ID, forming a track, and deposits all of its energy in the EM calorimeter. In the ATLAS detector a particle is considered as electron if the energy deposit in the EM is identified as electron-like, there is a reconstructed track pointing to the electromagnetic cluster and the track satisfies quality criteria related to number of Pixel hits, SCT hits and impact parameter. In particular the reconstruction of electron candidates begins with a seed cluster in the second layer of the electromagnetic calorimeter (if $E_T > 2.5$ GeV). A track matching the EM cluster is searched amongst all the tracks with $p_T > 0.5$ GeV/c reconstructed in the ID. The closest-matched track to the barycenter of the cluster is considered as the electron candidate. The electron candidate transverse energy is taken as the energy in the calorimeter cluster. In ATLAS three different electron identification definitions are used, according to the quality criteria required to the EM clusters and to the tracks in the ID. The three definitions give different values of purity and reconstruction efficiency and are labeled loose++, medium++ and tight++.

- Loose++: provides high and uniform identification efficiency but a low background rejection. It's based on calorimeter information, both EM and hadronic. In particular it uses the electromagnetic shower shape in the second layer of the EM calorimeter (in which an electron is expected to deposit 80% of its energy). The requirement are on:

  1. absence of energy deposits in the hadronic calorimeter (the electron deposits all the energy in the EM).
  2. lateral width of the shower (should be compatible with the Moliere radius)
  3. ratio between two set of clusters centered in the electron cluster position defined using also the ID information (one small cluster, 3x7 and one large cluster, 7x7)

- Medium++: compared to loose++ the fake rejection increases by a factor four but the identification efficiency decreases of about 10%. This quality provides additional rejection against the hadrons and in particular against $\pi^0 \to \gamma\gamma$. This is done using the information of the first layer of the EM calorimeter and information from the ID. The requirement are on:

  1. number of hits in the pixel detector ≥ 1
  2. number of hits in the pixel detector plus semiconductor tracker ≥ 9
  3. transverse impact parameter of the associated track < 1 mm
  4. cut on a matching track variable between the cluster and the track extrapolated to the first layer of the EM

5. cuts on the first and second largest energy deposits
6. total shower width
7. cut on the fraction of energy outside the central cone (three strips) and within seven strips

- Tight++: this definition, compared to the previous, allow a higher background rejection but has a looser identification efficiency. The tight++ selections allow to discriminate, better than medium++, the charged hadrons and photon converting to electrons. The requirement are on:

  1. number of hits in the TRT
  2. tight impact-parameter requirement
  3. difference in η and ϕ between cluster and track
  4. ratio between cluster energy and track momentum (E/p)
  5. Cut on a conversion-flagging algorithm, using pixel detector information, to reduce electrons from conversions
  6. ratio between the transverse energy in a cone $\Delta\text{R} < 0.2$ and the total cluster transverse energy.

All the charged particles and in particular, due to the low mass, the electrons lose energy when deflected or decelerated. This is due to the electromagnetic radiation emitted by Bremsstrahlung. The particles also lose energy traveling through the matter. In the ATLAS detector an electron loses 20%-50% of its energy passing through the ID and hence an algorithm taking into account all the energy lost is necessary. The Gaussian Sum Filter (GSF) [56] it's an algorithm that refits the track taking into account the electron energy loss. To do it the algorithm assumes that the electron's trajectory can be approximated by a sum of weighted Gaussians. This produces a probability density function that describes the new track.

4.3 Muons

The muon is a charged particle weakly interacting that penetrates, losing a small quantity of energy, through all the ATLAS apparatus and travels reaching the MS. In the ATLAS detector a particle is considered as a muon if it deposits a small amount of energy in the calorimeter system and if it leaves charged tracks or in the ID or in the MS or in both these detectors. According to the information used to identify the muons [57], the particles are divided in four categories:

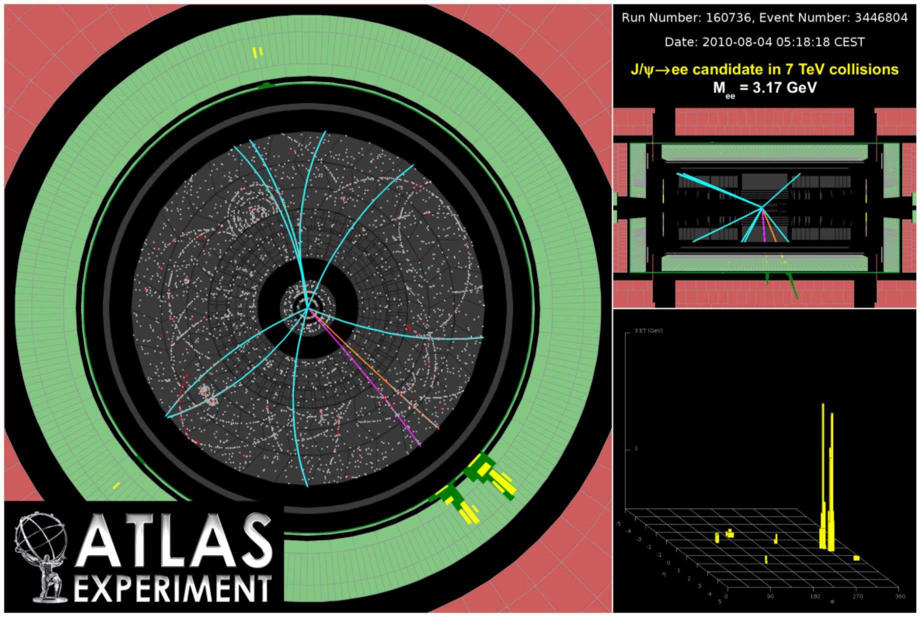

Figure 4.3: Example of electron reconstruction in ATLAS.
(from https://twiki.cern.ch/twiki/bin/view/AtlasPublic/EventDisplayPublicResults)

- Stand Alone muons (SA): if using only the information related to the MS
- Calorimeter tagged: using information coming from the ID and from the calorimeters. Efficient in recovering muons in the region near $|\eta| \approx 0$
- Combined: using information from both the ID and the MS. The tracks can be fitted combining seed tracks from inner detector and MS.
- Segment tagged muons: using information from both the ID and the MS segments. A muon is identified by matching an high momentum track in the ID with a segment of the MS (only one layer of the MS is necessary). This category allows to recover muons in regions poorly covered by the MS and muons with low transverse momentum

4.4 Jets

In the ATLAS detector a jet is reconstructed using track information from the ID and energy information from the calorimeter. In particular, in the calorimeter, clusters of

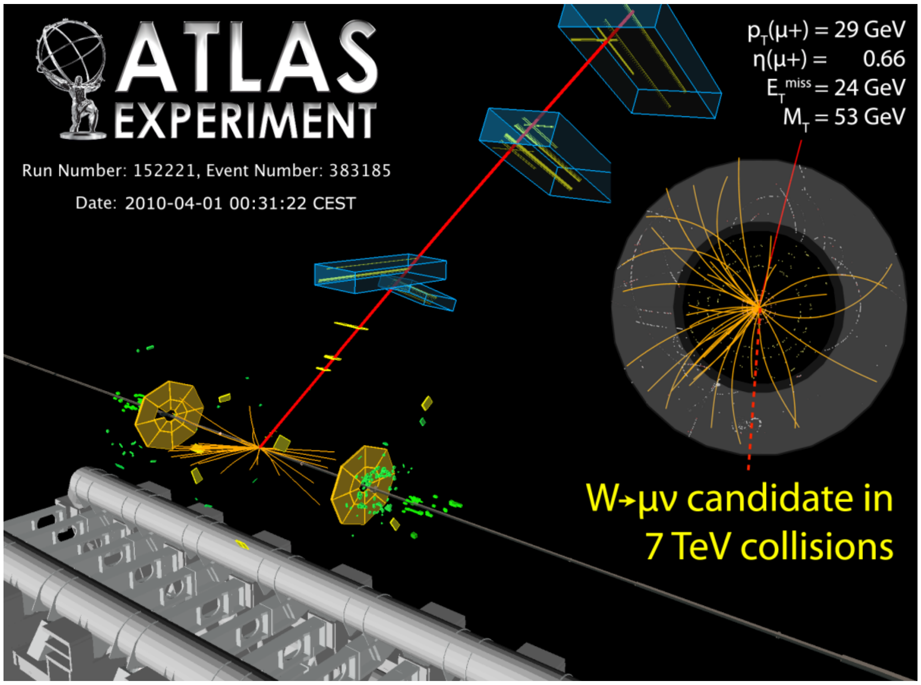

Figure 4.4: Example of muon reconstruction in ATLAS.
(from https://twiki.cern.ch/twiki/bin/view/AtlasPublic/EventDisplayPublicResults)

energy deposit are considered. Algorithms for jet reconstruction have to be collinear and infrared safe.
The collinear safety is connected to how the transverse momentum is distributed among the collinear decay products. For example a reconstructed jet should not depend on the decay of a particle into two collinear particles.
The infrared safety is connected to the sensitivity of an algorithm to the presence of an additional soft particle not related to the fragmentation of the hadronized particle. For example if there is a low energy cluster between two high energy clusters separated, the algorithm should have the possibility to discriminate between the two high energy clusters and define it as two separated objects. All the algorithms used by the analysis in ATLAS are basically connected to the energy deposits in the calorimeter. In particular there is a cut on the calorimeter deposits connected to the signal significance defined as the ratio between the energy in the calorimeter's cell and the average noise in the cell itself. ATLAS uses mainly two algorithms to reconstruct a jet: the Fixed Cone method and the k_T algorithm. The Fixed Cone method sums the four vectors of the particles within a cone of ΔR (typically 0.4 or 0.6) into an

object, called jet. The center of the cone is taken as the largest energy calorimeter cluster. All the objects within the defined cone are added to the jet. In a second iteration the jet center is recomputed taking into account the information within the cone. This procedure continues until the center of the object does not change. All the particles in the final cone are considered part of the jet and removed from the list of particles. Once the first jet is defined, if there is another energy cluster larger than a certain threshold, the same procedure is applied to all the particles in the new list of particles. This algorithm is really fast but is not infrared safe since a small energy cluster could induce the algorithm to merge two different jet. An algorithm slower than the Fixed Cone but infrared and collinear safe is the k_T algorithm. This method is based on the distance between two calorimeter clusters. In particular for each pair i,j of calorimeter objects the metric

$$d_{ij} = min(p_{Ti}^{2m}, p_{Tj}^{2m})\frac{(\Delta R)_{ij}^2}{R^2} \tag{4.1}$$

is computed together with the single metric

$$d_i = p_{Ti}^{2m} \tag{4.2}$$

In the k_T algorithm "m" is chosen equal to 1 while R is typically 0.4 or 0.6, depending on the analysis. The method sum the individual particles i and j in a jet object if the minimum of the d_{ij} and d_i is from the pair. In a second iteration the new jet object is considered as one single particle and the procedure is applied again. The iterations continue until the value of d_i is smaller than d_{ij}, when it's the case the object corresponding to the d_i is considered as a jet and the procedure starts over with another pair of particles. This process is repeated until no clusters are left. In certain analyses, like in the one discussed in this thesis, an algorithm similar to the k_T is used, it's called anti-k_T [58]. The difference between the k_T and the anti-k_T is the choice of the value for the parameter "m". In anti-k_T "m" is equal to -1. The procedure is the same and the results depends on the value of R. In the WH analysis, as described in chapter 5, the value chosen for R is 0.4.

Jets originating from b quarks can be separated from lighter ones using dedicated algorithms called b-taggers. To identify the b-jets is interesting because they are present in final states of process such as the ones related to the top quarks, like $t\bar{t}$ and single top. For the WH with H decaying in two W bosons analysis the top related background is one of the most important ones and that's why the flavor tagging has an important role in this channel. Due to the long life of the B-hadrons the jet connected to this kind of particles typically contain particles from a secondary vertex. Such hadrons can propagate from the point of origin for about 450 μm. The b-jets could have also a tertiary vertex connected to the c-decay. In the ATLAS detector the position of the secondary vertices is used to discriminate between light jet and b-jet. In particular tracks related to a b-jet will have an impact parameter, defined as the distance of closest approach of the track to the primary vertex, inconsistent with the primary vertex.

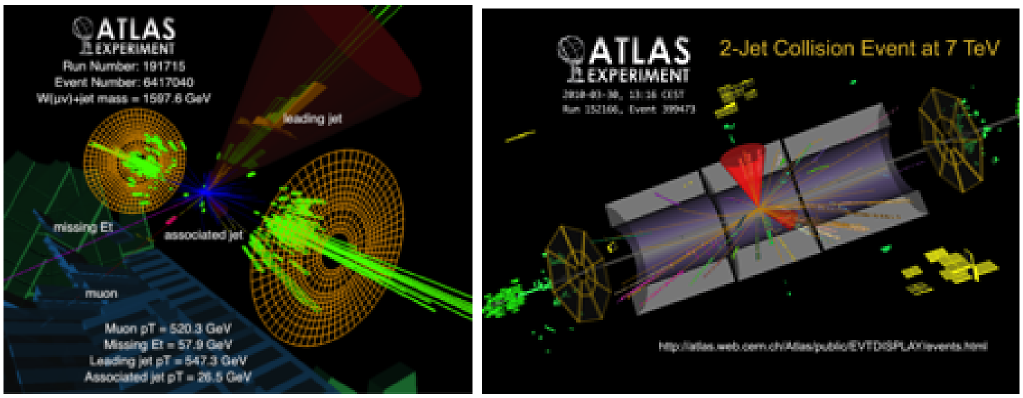

(a) (b)

Figure 4.5: Examples of jet reconstruction in ATLAS. Two different views are shown in (a) and (b).
(from https://twiki.cern.ch/twiki/bin/view/AtlasPublic/EventDisplayPublicResults)

In ATLAS several algorithms are used to identify and reconstruct the b-jet. All of them are based mainly on parameter related to the tracks after quality selections focused on rejecting the tracks related to long lived particles as the K.

Examples of b-jet tagging algorithm using the impact parameters of tracks can be find in Ref. [59]. One of them is the IP3D, an algorithm using a likelihood ratio technique to discriminate between b-jet and light-jet using the d_0/σ_{d_0}, where d_0 is the transverse impact parameter, and the z_0/σ_{z_0}, where z_0 is the longitudinal impact parameter. There are also algorithms, like SV0 and SV1, based on secondary vertices and tracks in the jet cone information. ATLAS has also an algorithm, JetFitter, based on the decay chain inside the jet. This method is based on the line of flight of the particles related to the b and c quarks and on variables similar to the ones used in the secondary vertices methods. The previous algorithms can be combined to achieve better performance. For example it's possible to create an artificial neural network using a combination of JetFitter and IP3D.

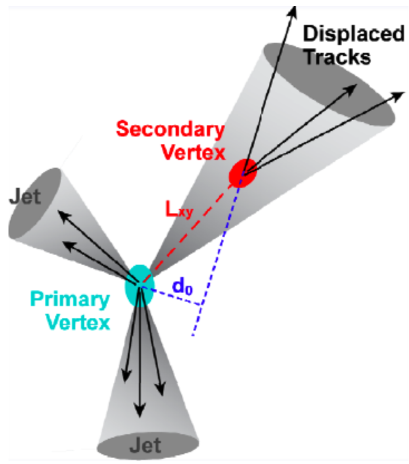

Figure 4.6: Example of event with a secondary vertex related to a b-tagged jet.

4.5 Missing transverse momentum

Due to the momentum conservation and negligible beam divergence, the total transverse momentum of the events should be exactly zero. From the experimental point of view the total transverse momentum can be reconstructed for all particles but for neutrinos and similarly weakly or non interacting particles. In the presence of this kind of particles it's possible to observe an imbalance of the reconstructed transverse momentum that means a sum of transverse momentum measured in the detector different from zero. It's possible to construct a non-zero transverse momentum or missing transverse momentum E_T^{Miss}. The missing transverse momentum could be defined as

$$E_T^{Miss} = \sqrt{E_x^{Miss^2} + E_y^{Miss^2}} \tag{4.3}$$

where $E_{x(y)}^{Miss}$ are the x and y projections of E^{Miss} respectively. The two projections can be found looking at the information of all the detectors of the apparatus. The $E_{x(y)}^{Miss}$ can be defined as

$$E_{x(y)}^{Miss} = E_{x(y)}^{Miss,Calo} + E_{x(y)}^{Miss,Muon} \tag{4.4}$$

The $E_{x(y)}^{Miss,Calo}$ is measured from the clusters information connected to physical objects, like electrons, muons and jets reconstructed as explained in the previous sections. The deposits not associated to a physical object are not take into account unless they form clusters with an energy larger than a threshold. The $E_{x(y)}^{Miss,Muon}$ is computed from the momentum of the tracks reconstructed in the muon spectrometer. Muons entering in this calculation should have a matching with a track in the inner detector to reduce the contribution due to fake muons.

Fake leptons can affect the missing transverse momentum measurement introducing a fake missing transverse momentum. From the analysis point of view it's really difficult to discriminate between real and fake missing transverse momentum and this is the reason why a precise measurement of this quantity is important. Further contributions due to electrons, photons, taus and jets are included in the calibration of the E_T^{Miss} together with a term taking into account the possible energy loss of physical objects traveling into the matter. The analysis described in chapter 5 is related to WH with H decaying into two W bosons events with a fully leptonic final state. In this channel signal events have real missing transverse momentum due to the presence of neutrinos coming from the three W bosons decays. In topologies like that it becomes really important a precise measurement and calibration of the real missing transverse momentum to discriminate between signal and background events.

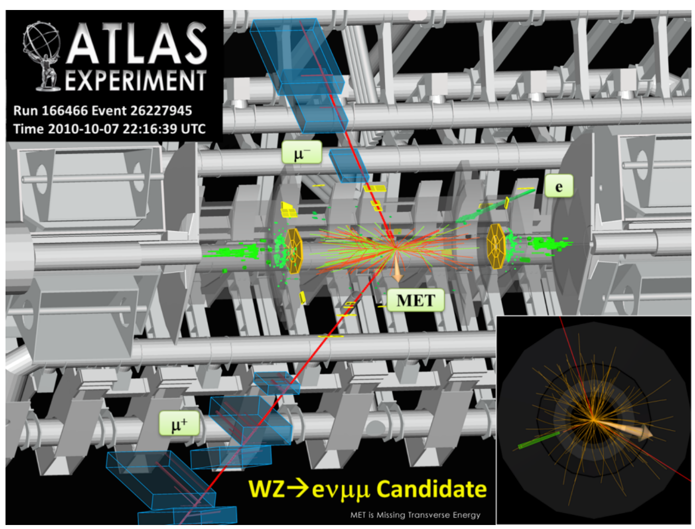

Figure 4.7: Example of missing transverse momentum reconstruction in ATLAS. (from https://twiki.cern.ch/twiki/bin/view/AtlasPublic/EventDisplayPublicResults)

Chapter 5

$WH \to WWW^{(*)} \to l\nu l\nu l\nu$ analysis

In this chapter a study of the production of a Higgs boson in association with a W boson with a fully leptonic final state is presented. Only muons and electrons are considered in the final state. The study is done using the data collected in the 2012 at $\sqrt{s} = 8$ TeV by the ATLAS experiment. The analysis goal is to study the WH production, hereafter called 3-lepton analysis, focusing on a Higgs boson mass hypothesis of 125 GeV. The event topology is described in section 5.1 and it is mainly related to events with a lepton total charge of ± 1 and with real missing transverse momentum. The analysis has also some acceptance for a Higgs boson produced in association with a Z boson as well as for a Higgs boson, produced in association with a W boson, decaying to a pair of tau leptons. The 3-lepton analysis result will also be combined (chapter 6) with a study performed by the ATLAS collaboration on the ZH production [60]. In this case the Higgs boson decay analyzed is the $H \to WW^{(*)}$ with a fully leptonic final state. Hereafter we will refer to the ZH analysis as the 4-lepton analysis. The results will be presented taking into account these channels for Higgs boson mass hypotheses between 110 and 200 GeV, though the selections were optimized for a Higgs boson mass $m_H = 125$ GeV. In section 5.2 a description of the data sample and the simulated samples is reported while the trigger and object definitions are discussed in section 5.3. The event selection adopted in the analysis and the comparison between data and expectations are reported in sections 5.5 and 5.6-5.9 respectively. The sources of systematic uncertainties are discussed in section 5.10.

As described in section 5.4 the 3-lepton analysis overlaps in a small phase space corner with the Higgs boson search in the WW$^{(*)}$ decay channels [61], hereafter called 2-lepton analysis, since in the WH analysis events with exactly three leptons are selected while in 2-lepton analysis candidates are requested to have exactly two leptons. The requirement of additional high transverse momentum leptons allows the 3-lepton analysis to have looser lepton quality criteria. The overlap comes from events with exactly two leptons satisfying the tighter quality criteria presented in Ref. [61] and exactly one failing them but satisfying the selections of the WH analysis. The analysis presented was optimized for WH irrespectively from the overlap, but in order to allow a statistical combination of the results presented here with the 2-lepton analysis, the events in overlap were explicitly removed in the 3-lepton analysis.

5.1 Physics Process

The event's signature studied in this analysis is related to three leptons and high missing transverse momentum. This topology is common to different physics processes, which represent the background to the WH signal. The backgrounds with three isolated real leptons are mainly Standard Model diboson productions of $W\gamma^{(*)}$ and $WZ^{(*)}$, together with $ZZ^{(*)}$ production with an undetected lepton, and cannot be reduced by the application of tight lepton identification criteria. Due to the presence of one neutral particle (Z or γ) these backgrounds are characterized by the presence of at least one pair of same flavor opposite sign (SFOS) leptons. To suppress these backgrounds and obtain a better significance, the analysis distinguishes events with SFOS leptons from events without any such pair, in *Z-enriched* and *Z-depleted* samples, respectively. Final states with fewer than three prompt leptons and/or without real missing transverse momentum may enter as backgrounds in the presence of fake leptons and resolution effects. Fake leptons are defined as both misidentified leptons and real leptons from light flavor, beauty and charm decays. Background processes with two prompt leptons, such as WW, Z and $t\bar{t}$ production, must be accompanied by a fake lepton to enter either the *Z-enriched* or *Z-depleted* samples. They can therefore be significantly reduced by isolation requirements on the three leptons. Final states with only one prompt lepton, such as W boson or single top production, would require two fake leptons in addition to the real lepton and are heavily suppressed by isolation requirements. At a significantly lower rate, but comparable with the signal, the triboson Standard Model production VVV, in particular the $WWW^{(*)}$ process, represent an irreducible background. The *Z-enriched* sample contains 3/4 of the signal, but suffers from all the backgrounds listed above, while the *Z-depleted* sample contains only 1/4 of the signal but is affected mainly by those backgrounds that are reducible through lepton identification and/or isolation criteria. Due to the different background composition of the *Z-enriched* and *Z-depleted* samples, the selection criteria are optimized separately.

Helicity conservation in the decay of the two W bosons from a scalar Higgs boson leads in general to a small opening angle between the leptons originating from the Higgs boson decay, while the lepton from the decay of the recoiling W boson tends to be at a large angle with respect to the other two. Hence it is possible to discriminate between irreducible background and signal events using the opening angle between leptons.

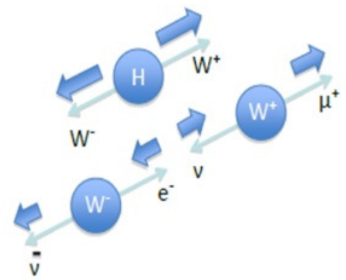

Figure 5.1: Helicity conservation in $H \to WW^{(*)}$. Due to the spin 0 nature of a SM Higgs boson the opening angle between the leptons coming from the WW$^{(*)}$ decay is small.

Process	Information	Cross Section (pb)
WH	three leptons	0.150
ZH	Z to all + H to two leptons	0.085
ttH	three leptons	0.028
WZ	three leptons	12.670
Wγ^*	three leptons	7.811
VVV	three leptons	0.007

Table 5.1: Main signal and background processes cross sections.

5.2 Data sample and simulated events

In this section a description of the data sample used in the analysis is reported in section 5.2.1 while a detailed explanation of the MC generators used for the simulated events is reported in section 5.2.2.

5.2.1 Data sample

The analysis described here uses proton-proton LHC collision data at a center-of-mass energy of 8 TeV collected with the ATLAS detector between April and September 2012. The data were collected using inclusive single-muon and single-electron triggers. The two main triggers require the transverse momentum (p_T) of the lepton, with respect to the beam line, to exceed 24 GeV and the lepton to be isolated: the scalar sum of the p_T of charged particles within a cone of $\Delta R = \sqrt{\Delta\phi^2 + \Delta\eta^2} = 0.2$ of the lepton direction is required to be less than 0.12 and 0.10 times the lepton p_T for the muon and electron, respectively. Auxiliary non-isolated triggers are used both for electrons and muons. The trigger efficiencies are measured as a function of p_T, η and data-taking period using Z boson events. The efficiencies are approximately 95% for electrons and 90% (70%) for muons in the endcap (barrel) with respect to the offline reconstructed leptons. Stringent detector and data quality requirements are applied, resulting in a data set corresponding to an integrated luminosity of 20.7 fb^{-1}.

5.2.2 Simulated events

In this analysis several MC generators have been used following as much as possible the MC samples used in Ref. [61]. In particular simulated signal events are generated using PYTHIA8 [62] but the cross-sections used in this analysis are taken from Ref. [12]. Higher-order corrections have been computed up to next-to-next-to-leading order (NNLO) in QCD for both the WH and ZH production (here and after called VH when considered together) processes [63]. Electroweak radiative corrections are applied up to next-to-leading order (NLO) to the VH decays [64]. The Higgs boson decay branching ratios are computed with HDECAY [65]. Concerning the background samples, to model the production of W boson and Z/$\gamma^{(*)}$ bosons decaying to charged leptons in association with jets (the latter is also referred to below as the Drell-Yan process), ALPGEN [66] , interfaced to HERWIG [67] and the MLM matching scheme [68] is used. To model the parton shower and the hadronization of $\mathrm{t\bar{t}}$ events MC@NLO [69] with HERWIG are used. Parton showering is performed by HERWIG while JIMMY [70] is used for the simulation of the underlying event. POWHEG [71] is used for the generation of ZZ$^{(*)}$ and WW. An additional contribution to the WW continuum background from gluon-initiated diagrams is modeled using gg2WW [72] interfaced with HERWIG. Wγ production is modeled with ALPGEN while MADGRAPH [73, 74] is used for W$\gamma^{(*)}$ [75], and for the triboson productions WWW$^{(*)}$, WWZ$^{(*)}$ and ZZZ$^{(*)}$. The different choices for the generators of the WZ$^{(*)}$ process compared with the $H \to WW^{(*)} \to l\nu l\nu$ analysis is due to the need in the WH case to well model the relative ratio between events with zero and one associated jets and three good leptons. For the Wγ production ALPGEN is employed. ACERMC [76] is used for the generation of single top events in the t-channel, using PYTHIA for showering and hadronization. MC@NLO is used for the Wt and single top events in the s-channel production channels. $t\bar{t}W$ and $t\bar{t}Z$ events are generated with MADGRAPH. The CT10 parton distribution function (PDF) set [77] is used for the MC@NLO samples; CTEQ6L1 [78] is used for the ALPGEN, MADGRAPH and PYTHIA8 samples, but with the ALPGEN $Z/\gamma^{(*)}$ sample reweighted to the MRSTMCal [79] PDF set, as MRSTMCal better models the lepton kinematics. To take into account the pile-up all MC simulated samples are generated with multiple proton-proton interactions. These simulated events are re-weighted so that the distribution of the number of interactions per bunch crossing matches the one observed in the data. Acceptances and efficiencies based on a full simulation of the ATLAS detector [80] are introduced processing the simulated samples with the GEANT4 [81] software.

5.3 Trigger and Physics objects

This section is deeply related to the event selection (section 5.4) and it describes the triggering criteria and the definitions of the physics objects. These are really important for the analysis since it's necessary to solve the ambiguity due to overlaps between different reconstructed objects and because one of the most relevant issues, for all the analyses involving lepton final states, is the misidentification of fake leptons as real leptons. A typical example of this problem is the $H \to WW^{(*)} \to l\nu l\nu$ analysis where one important and deeply investigated source of background is the W boson produced in association with one or more jets (hereafter called W+jets) with a fake lepton coming from the jet. In the 3-lepton analysis the fake lepton problem becomes relevant for the Z boson produced in association with one or more jets (hereafter called Z+jets) background but fortunately it is possible to suppress these events requiring an invariant mass of a same flavor opposite sign lepton pair far from the Z boson peak. As discussed briefly in the introduction of this chapter the basic signatures of 3-lepton candidate events are:

- the presence of three leptons with high transverse momentum
- total charge for the leptons of $\pm$ 1
- presence of large missing transverse momentum (E_T^{Miss}) due to the leptonic decay of the three W bosons
- low jet activity and no b-tagged jet

As described in section 5.1 the helicity conservation leads in general to a small opening angle between the leptons originating from the Higgs boson. Because of the charge 0 of a Standard Model Higgs boson, the leptons coming from the decays of the W bosons produced by the Higgs boson have to be opposite in charge. For these reasons the leptons are classified according to the charge and the opening angles: lep_0 and lep_1 are defined as the leptons coming from the Higgs boson decay while lep_2 is the lepton coming from the recoiling W boson decay. Then events are classified by identifying lep_0 as the lepton with unique charge (assumed to be from the Higgs boson), lep_1 as the lepton closer in ΔR to lep_0 (due to the helicity conservation), and lep_2 as the remaining one.

5.3.1 Trigger

In the ATLAS experiment several types of trigger have been defined. In this analysis the candidate events are recorded with unprescaled single lepton triggers and the final state considered involves only electrons and muons. In channels where all the leptons carry the same flavor (eee and $\mu\mu\mu$) only the electron or muon triggers are required while in other channels an OR of the electron and muon triggers is performed. This requirement allows to increase the acceptance. The trigger naming scheme used by the ATLAS collaboration summarizes the information related to the trigger itself. The electron trigger has the suffix EF_e (Event Filter). This suffix is followed by a number representing the nominal p_T threshold, expressed in GeV. The electron triggers used in this analysis are EF_e24 and EF_e60. In the electron trigger naming there is also a tag concerning the tightness in the electron identification. The electrons could be tight, medium or loose according to the description given in chapter 3. In some cases a tag "vhi" is added in the trigger name, it means that the trigger has η dependent p_T thresholds and a hadronic leakage cut at L1 as well as an isolation requirement in terms of scalar sum of p_T of the charged tracks around electrons at Event Filter. For electrons, the OR between two triggers, EF_e24vhi_medium1 and EF_e60_medium1, is used in the analysis. The naming convention for the muon trigger is similar to the electron one. The name starts with a suffix EF_mu followed by the nominal p_T threshold. In the 3-lepton analysis the p_T triggers thresholds are set to 24 GeV and 36 GeV. In particular, for muons, the OR of EF_mu24i_tight and EF_mu36_tight is used in the analysis. The suffix tight indicates that the triggers use L1_MU15 at Level 1. An isolation requirement in terms of scalar sum of p_T of the charged tracks around muons is applied at Event Filter in EF_mu24i_tight. Table 5.2 shows the list of triggers used in the analysis.

In the analysis, trigger matching is attempted for leptons with $p_T > 25$ GeV with

electron trigger	muon trigger
EF_e24vhi_medium1 || EF_e60_medium1	EF_mu24i_tight || EF_mu36_tight

Table 5.2: Triggers used in the analysis. In the first column the electron triggers while in the second column the muon triggers.

$\Delta R = 0.15$. If all of the leptons selected by the analysis fail the trigger matching, the event is discarded. As the identification cuts for electron triggers were changed during the data taking, a luminosity weight using a random number method is applied. To account for possible differences in efficiency between data and MC a per-event correction factor, also called Scale Factor (SF), is computed based on the per-lepton SFs as

$$\text{per}-\text{event SF} \;=\; \left[1-\prod_{i=0}^{2}\left(1-\epsilon^{i}_{MC}\times SF^{i}\right)\right]/\left[1-\prod_{i=0}^{2}\left(1-\epsilon^{i}_{MC}\right)\right]. \qquad (5.1)$$

here ϵ^{i}_{MC} is the per-lepton trigger efficiency and SF^{i} is the per-lepton SF for lepton i. To estimate the per-lepton SF a tag-and-probe method with $Z \to ll$ events is used. A description of this method is found in Ref. [82]. The per-lepton efficiency is assumed to be zero for leptons with $p_T < 25$ GeV.

5.3.2 Reconstructed objects

Following the definitions given in chapter 4, in this section a description of the physics objects defined in the analysis is reported. In particular the definitions of muons, electrons, missing transverse momentum and jets are presented.

Muon

Muons considered in this analysis are reconstructed using a standard ATLAS algorithm [83] which employs a statistical combination approach to combine the two tracks reconstructed in the inner tracking detectors and in the muon detector (defined as combined muons in section 4.3). All combined muons are required to fulfill criteria based on the number of hits. The fiducial region is defined by the $|\eta|$ computed from the combined muon's track parameters ($|\eta| < 2.5$). Within this angular region, muons are required to have $p_T > 10$ GeV. To select muons generated by prompt decays of the W bosons the distance in z between the reconstructed primary vertex and the nominal interaction point (z_0) together with the transverse impact parameter (d_0) are considered. To take into account the difference in muon identification efficiency, p_T scale and resolution between data and MC, correction procedures are applied. To reject muons resulting from the fragmentation of jets, especially b-jets, an isolation criteria, taking into account the ratio between the muon p_T and the track p_T or energy within a ΔR cone centered on the muon track, is applied. Moreover a procedure of overlap-removal is employed: if a muon overlaps with a jet in a cone with $\Delta R = 0.3$, the muon is not considered as a lepton candidate for the analysis but its momentum is still taken into account in the missing transverse momentum calculation.

Electron

Electrons in this analysis are reconstructed using a standard algorithm of the ATLAS experiment and are required to satisfy the Medium++ identification criteria described in section 4.2. The fiducial region is defined by the direction of an electron based on the reconstructed cluster energy $|\eta_{cluster}|$. In particular the fiducial acceptance is $|\eta_{cluster}| < 2.47$, with the barrel-endcap transition region of $1.37 < |\eta_{cluster}| < 1.52$ vetoed to ensure good energy and position resolutions. Within this region, electrons are required to have $E_T > 10$ GeV. To select electrons generated by the prompt decays of the W bosons, as for the muons, the z_0 and d_0 are considered. To take into account the difference in electron identification efficiency, E_T scale and resolution between data and Monte Carlo, correction procedures are applied. To reject electrons resulting from misidentified jets, an isolation criterion, taking into account the ratio between the electron energy and the calorimeters' energy deposits within a ΔR cone centered on the electron track, is applied. Electron clusters containing a problematic cell are not considered in the analysis. A procedure of overlap-removal is employed: electron-electron overlaps in a cone with $\Delta R < 0.1$ are resolved in favor of electron with higher transverse energy. Moreover electron-muon overlaps in a cone with $\Delta R < 0.1$ are resolved in favor of muon.

Jets

In this analysis jets are reconstructed using the anti-k_t algorithm [58], based on topological calorimeter clusters with radius $R = 0.4$. The fiducial acceptance is defined by $|\eta_{jet}| < 4.5$. The jets in this region are required to have a p_T larger than 25 GeV. The only exception is for the jets in the forward part of the apparatus ($|\eta| > 2.4$) in which the p_T threshold is raised to 30 GeV. All the jets are required to pass a loose quality selection recommended by the ATLAS collaboration [84]. This selections have an efficiency above 99%. Jet reconstruction is affected by the pile-up. To reduce this effect, the fraction of tracks which are associated to the primary vertex in a given jet with $p_T < 50$ GeV is required to be larger than 0.5 for all jets except those with no associated track. The flavor tagging is provided by an algorithm which is based on a neural network ("MV1"). It uses as input the output weights of the JetFitter+IP3D, IP3D and SV1 algorithms, described in section 4.4 and in Ref. [59]. The algorithm is tuned to achieve 85% of b-tagging efficiency using a sample of $t\bar{t}$ events with jet $p_T > 20$ GeV and $|\eta| < 2.5$. Like in the electron and muon cases, also for the jet an overlap-removing criteria is applied. In particular if a jet overlaps with an electron in a cone with $\Delta R = 0.3$, the jet is discarded.

Missing Momentum

As introduced in section 4.5 the E_T^{Miss} is obtained as the opposite of the vector sum of the transverse momenta of the reconstructed objects [85]. The physics objects include muons, electrons, taus, photons, jets and calorimeter clusters which are not associated with these objects.

To take into account a possible correlation between the E_T^{Miss} and a not well reconstructed object, in this analysis a new variable is introduced: the $E_{T,rel}^{Miss}$

$$E_{T,rel}^{Miss} = E_T^{Miss} \sin \Delta\phi_{\min}, \tag{5.2}$$

with $\Delta\phi_{\min} \equiv \min(\Delta\phi, \frac{\pi}{2})$. Here $\Delta\phi_{\min}$ is the angle between the missing transverse momentum and the nearest lepton or jet which passed the selection criteria described in the previous sections. The main purpose of this modified definition of missing transverse momentum is to reduce the impact of mismeasurements of high p_T leptons and jets on the total missing transverse momentum.

5.4 Event Selection

In this section the selections performed in this analysis, together with a first definition of analysis regions and background, is reported. The selections adopted will be presented splitted in two categories:

- Pre-Selection
- Analysis Selection

The pre-selection is mainly focused on removing non-collision events or events with a number of reconstructed tracks different from three, while the analysis selection is optimized to suppress background events with a topology similar to the one described in section 5.1. Concerning the background definition, in section 5.4.2 a categorization of the main sources of background and of the events will be reported.

5.4.1 Pre-Selection

These selections are chosen aiming to remove the non-collision or out of time events, together with cosmic ray events. Pre-selection is based on primary vertex, tracks and luminosity information. A Good Run List (GRL), prepared by a group of data quality expert, is used to take into account only the data taking period with real proton-proton collisions and good ATLAS apparatus performance. This list of events is useful to remove non-collision events, such as cosmic rays or events with possible problems in the objects reconstruction or in the trigger. To ensure the selection of collision events at a pre-selection stage also a requirement on the track number and p_T is imposed. The primary vertex should have at least three associated tracks of $p_T > 400$ MeV. At the pre-selection level also cuts on the reconstructed objects are requested. For the topology described in section 5.1 events should contain exactly three isolated leptons with $p_T >$15 GeV and a total charge of ± 1. The isolation criteria is based on both calorimeter and tracking information. In particular for track-based isolation, the scalar sum of the transverse momenta of tracks coming from the primary vertex, in a cone of $\Delta R = 0.4$ around the candidate lepton track, is required to be less than 5% of the p_T of the track itself while for calorimeter-based isolation, the scalar sum of the transverse energy in the calorimeters cells within a cone around the lepton track is required to be less than 10% of the lepton p_T. For low p_T leptons ($15 < p_T <$20 GeV), the cut on the scalar sum of the calorimeter cells' transverse energy, in a cone around the lepton track, is modified and it is required to be less than 5% of the lepton p_T. Moreover one of the three leptons should be matched to the trigger described in section 5.3.1. The pre-selection suppresses completely some background sources which will not be discussed further in the following. These are mainly events of inclusive W boson production and production of $\mathrm{b\bar{b}}$ pairs. The charge flipping probability was investigated but it was found negligible hence also events with three leptons of the same sign, as for example the $\mathrm{WWW}^{(*)}$ sample with a fully leptonic final state, are suppressed. A contribution from single top production, despite the reduction due the isolation requirements, is still present after the pre-selection. It will be treated in plots and tables together with the $\mathrm{t\bar{t}}$ background, since they are both related to fake lepton. The fusion of single top and $t\bar{t}$ samples will be called hereafter "Top" sample.

5.4.2 Background definitions and analysis regions

Before going into the details of the event selections it is interesting to discuss the signal and background definitions used in this analysis. The possible background sources could be divided in two main groups:

- Z and DY related background (hereafter called Z-related): events with at least one 1 SFOS lepton pair.
- Fake lepton background: events with a fake lepton reconstructed as real.

The number of events corresponding to the first category is orders of magnitude larger than the second one. This is mainly due to the cross section of the background forming the two categories and the suppression due to the pre-selection described above. To gain in significance also the signal events are splitted in two categories. These categories are called:

- *Z-enriched*: events with at least 1 SFOS lepton pair
- *Z-depleted*: events with no SFOS lepton pair

Z-enriched **region**

The events with the presence of at least one pair of same flavor opposite sign leptons (combinations with 1 SFOS and 2 SFOS are possible) are defined as *Z-enriched*. The name has been chosen because they are related to the presence of a Z or γ bosons.

The main background processes related to this region are:

- Drell-Yan production
- $WZ^{(*)}$ production
- $W\gamma^{(*)}$ production
- $ZZ^{(*)}$ production (with a lepton not identified)
- Z+jets production (with a fake lepton coming from a jet)

The number of background events in this region is huge and, besides the Z+jets, they cannot be suppressed using tighter lepton isolation criteria or cut on lepton p_T because of the presence of real high p_T leptons with total charge ± 1. Fortunately, due to the presence of a Z boson like lepton pair it is possible to suppress this background selecting a dilepton invariant mass window far from the Z peak. The Drell-Yan background is suppressed requiring to the smallest dilepton invariant mass to be greater than 12 GeV. In the *Z-enriched* also fake lepton backgrounds are present but, due to the suppression obtained with the isolation criteria at the pre-selection stage, these sources of background are less important than the Z-related ones. Concerning the signal it is easy to demonstrate, counting the possible final states involving only muons and electrons, that 75% of the signal events lie in the *Z-enriched* region. According to this calculation the *Z-enriched* seems to be the region with the largest significance, but it is not true since it is affected by the Z-related backgrounds, that have a large cross section. The presence of 1 SFOS or 2 SFOS is related to different sources of backgrounds, hence to gain in significance, the *Z-enriched* region it is also divided in two regions according to the number of possible same flavor opposite sign leptons pairs.

Z-depleted **region**

The events, for both signal and background, with no SFOS lepton pair belong to the *Z-depleted* region. In this region only the 25% of the total signal events is present but the background gives smaller contribution than in the *Z-enriched* region. For this reason the contribution of the *Z-depleted* region to the total significance, despite the small number of signal events, is more important than the contribution of the *Z-enriched* regions. Due to the Z-related background suppression, the main sources of background in this region are connected to the events in which a fake lepton is reconstructed as real:

- single top production
- $t\bar{t}$ production
- Z+jets production

The advantage of the *Z-depleted* is that, contrary to the *Z-enriched*, the background could be suppressed using the isolation criteria described above. The isolation criteria affect in a marginal way the signal events so, the *Z-depleted* region, remain pure and with a good ratio between suppression of background and acceptance of the signal. Due to the topology of the events in this region another relevant source of background, not related to the presence of fake lepton, is the $\mathrm{WWW}^{(*)}$. In this analysis the triboson background $\mathrm{WWW}^{(*)}$, together with the other triboson source of background ($\mathrm{WWZ}^{(*)}$ and $\mathrm{ZZZ}^{(*)}$) will be named VVV. Due to the requirement of only three leptons the main contribution to the VVV comes from the $\mathrm{WWW}^{(*)}$, followed by the $\mathrm{WWZ}^{(*)}$ with a lepton missing. Because of the VVV topology, and in particular of the $\mathrm{WWW}^{(*)}$, this source of background will appear in both the *Z-depleted* and *Z-enriched* regions, but it's relative weight is more significant in the first region.

5.5 Analysis Selection

As described in the previous section, in this analysis the events are splitted in two orthogonal regions, *Z-enriched* and *Z-depleted*, according to the presence or not of a SFOS lepton pair. Due to the different background composition, the analysis selections are optimized separately for the two regions. However due the similar topology of the signal events in the two regions several selection are shared between the *Z-enriched* and *Z-depleted*. As introduced during the backgrounds composition discussions, in both the regions, there is a component defined as fake lepton background. One of the main sources of background in this category is the Top production. For this reason in all the regions, in order to reduce the Top background, events are required to contain at most one jet of transverse momentum above 25 GeV, which should not be b-tagged. This requirement will be referred to as b-veto in the following.

In figures 5.2 and 5.3 the expected number of jets and b-tagged jets distributions in the *Z-enriched* and *Z-depleted* samples after the pre-selection are shown. In the figures only MC events are presented in order to show the distribution for each source of background and for the signal (defined as the sum of WH and ZH production mechanisms' events). Due to the presence of neutrinos in the the fully leptonic final state of the $WH \rightarrow WWW^{(*)} \rightarrow l\nu l\nu l\nu$ channel, a selection on the missing transverse momentum is applied. In order to suppress events with low missing transverse momentum, $E_{T,rel}^{Miss}$ is required to be above 25 GeV for the *Z-depleted* sample and above 40 GeV for the *Z-enriched* sample. In figure 5.4 the expected $E_{T,rel}^{Miss}$ distributions in the *Z-enriched* and *Z-depleted* after b-tagged jets selection are shown. Only MC events are presented in order to show the distribution for each source of background. The different transverse momentum selection between *Z-enriched* and *Z-depleted* is due to the different background composition. In particular the Z+jets events, present mainly in the *Z-enriched* region, have a large cross section and an $E_{T,rel}^{Miss}$ distribution peaked a lower value compared with other sources of backgrounds. In the *Z-enriched* region, where the Z-related background contribution is present and

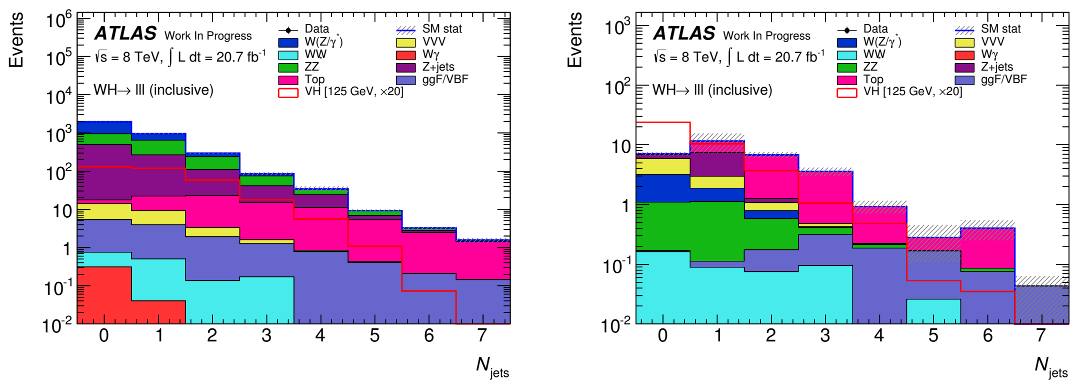

(a) (b)

Figure 5.2: Distributions of number of jets in the (a) *Z-enriched* and (b) *Z-depleted* samples after the pre-selection. In figure only MC events are presented in order to show the distribution for each source of background. The signal events, considered as SM Higgs boson for a mass hypothesis of 125 GeV, are multiplied by a factor 20 and superimposed. The different sources of background are stacked. In plots the statistical error is presented for each bin.

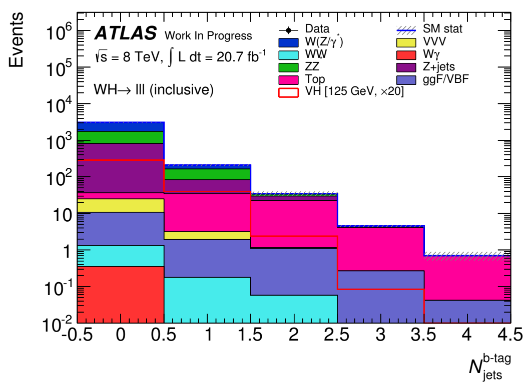

(a)

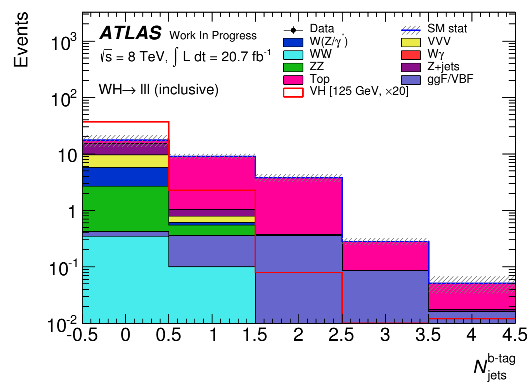

(b)

Figure 5.3: Distributions of number of b-tagged jets in the (a) *Z-enriched* and (b) *Z-depleted* samples after the pre-selection. In figure only MC events are presented in order to show the distribution for each source of background. The signal events, considered as SM Higgs for a boson mass hypothesis of 125 GeV, are multiplied by a factor 20 and superimposed. The different sources of background are stacked. In plots the statistical error is presented for each bin.

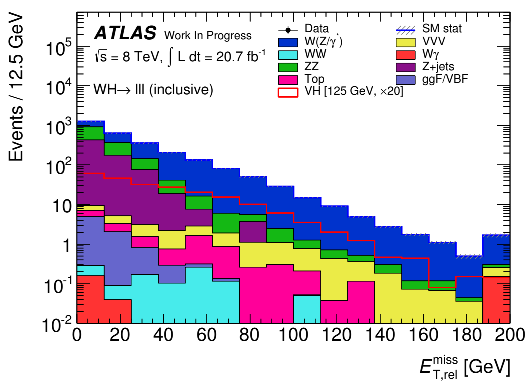

(a)

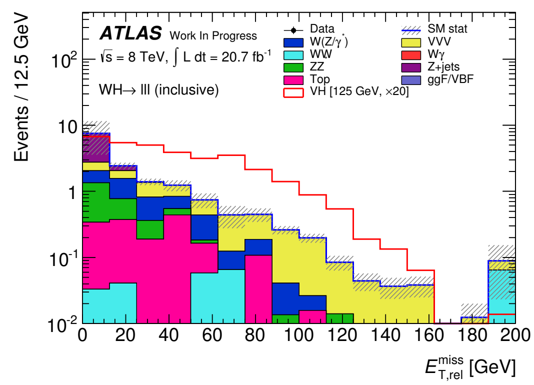

(b)

Figure 5.4: Distributions of $E_{T,rel}^{Miss}$ in the (a) *Z-enriched* and (b) *Z-depleted* samples after b-tagged jets selection. In figure only MC events are presented in order to show the distribution for each source of background. The signal events, considered as SM Higgs boson for a mass hypothesis of 125 GeV, are multiplied by a factor 20 and superimposed. The different sources of background are stacked. In plots the statistical error is presented for each bin.

dominates, the masses of all SFOS pairs are required to be at least 25 GeV away from the Z boson pole. This requirement suppresses particularly the WZ$^{(*)}$ and ZZ$^{(*)}$ irreducible backgrounds. Due the presence of W$\gamma^{(*)}$ and Drell-Yan events in both the *Z-depleted* and *Z-enriched* regions a lower cut is set on the smallest invariant mass of opposite sign leptons at 12 GeV, independently of their flavor. This selection reduces the W$\gamma^{(*)}$ and Drell-Yan backgrounds and rejects events from a region which could be populated by heavy flavor backgrounds. In figure 5.5 the expected dilepton invariant mass $M_{lep0,lep1}$ and $M_{lep0,lep2}$ distributions in the *Z-enriched* and *Z-depleted* after the $E_{T,rel}^{Miss}$ selection are shown. Only MC events are presented in order to show the distribution for each source of background. In figure 5.6 the expected dilepton invariant mass $M_{lep1,lep2}$ distributions in the *Z-enriched* and *Z-depleted* after the $E_{T,rel}^{Miss}$ selection are shown. Only MC events are presented in order to show the distribution for each source of background. As previously described another possible discriminant between signal and background events, in case of a SM Higgs boson, is the opening angle between the leptons coming from the Higgs boson decay. Due to helicity conservation, the leptons defined in the analysis as lep_0 and lep_1 should have an angular separation ($\Delta R(lep_0, lep_1)$) distribution different from the background. In particular the $\Delta R(lep_0, lep_1)$ is expected to be peaked at low values in the signal sample. Optimizing the selection for a SM Higgs boson mass hypothesis of 125 GeV, the best working point has been found to be $\Delta R(lep_0, lep_1) < 2$. In figure 5.7 the expected $\Delta R(lep_0, lep_1)$ distributions in the *Z-enriched* and *Z-depleted* before the $\Delta R(lep_0, lep_1)$ selection are shown. Only MC events are presented in order to show the distribution for each source of background. This selection favors the Higgs decay topology with respect to that of W$\gamma^{(*)}$ and WZ$^{(*)}$ events. Aiming at a combination with the gluon-gluon fusion and vector-boson fusion analyses involving the $H \to WW^{(*)} \to l\nu l\nu$ decay channel, considered together and called hereafter 2-lepton analysis, it is necessary to take into account possible overlaps between the three analyses. Even if a different number of leptons is requested at a pre-selection stage (two and only two leptons are required in the 2-lepton analysis) an overlap is possible due to different electron and muon definitions. As an example, if at pre-selection stage different cuts on leptons p_T are applied, as it is the case, an event could be considered in both the analyses. To avoid this problem and easily combine the two analyses, the events selected by the 2-lepton analysis are removed. In all the tables this additional selection, not related to the topology of the events, will be referred to as "lvlv OR". In figure 5.8 the expected $\Delta R(lep_0, lep_1)$ distributions in the *Z-enriched* and *Z-depleted* after the overlap removal with the 2-lepton analysis are shown. Only MC events are presented in order to show the distribution for each source of background. Table 5.3 summarizes the selection criteria describing the

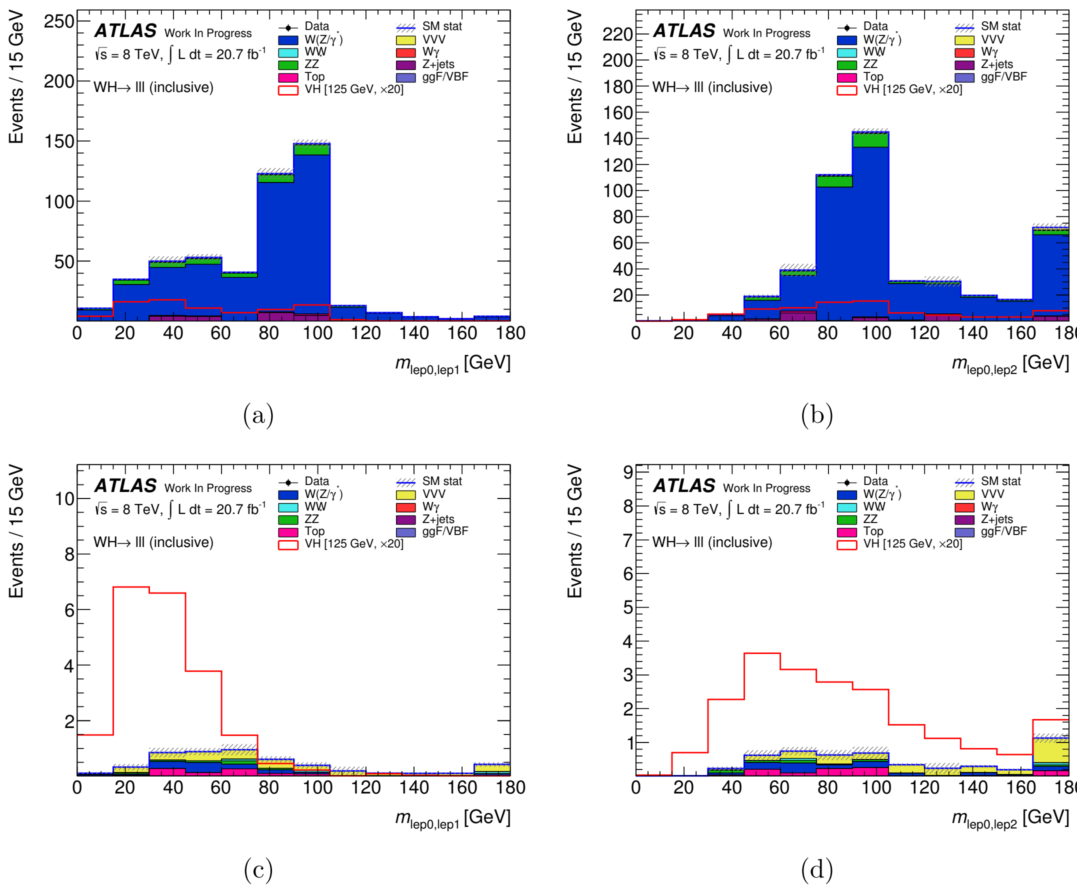

Figure 5.5: Distributions of dilepton invariant mass (a) $M_{lep0,lep1}$ and (b) $M_{lep0,lep2}$ for the *Z-enriched* sample after the $E_{T,rel}^{Miss}$ selection. In figures (c) the $M_{lep0,lep1}$ and in (d) the $M_{lep0,lep2}$ distributions for the *Z-depleted* sample after the $E_{T,rel}^{Miss}$ selection. In figure only MC events are presented in order to show the distribution for each source of background. The signal events, considered as SM Higgs boson for a mass hypothesis of 125 GeV, are multiplied by a factor 20 and superimposed. The different sources of background are stacked. In plots the statistical error is presented for each bin.

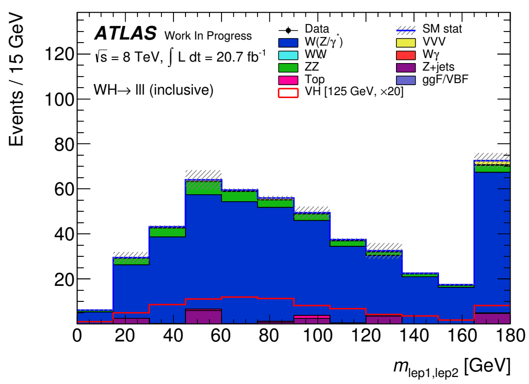

(a)

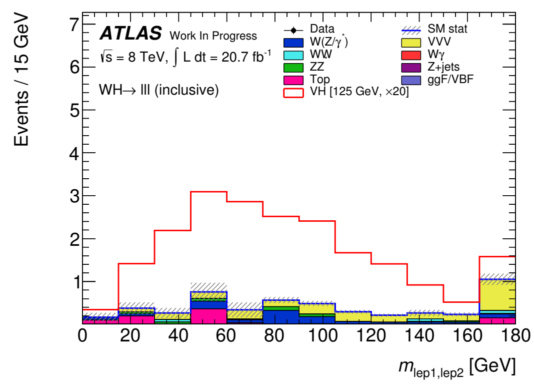

(b)

Figure 5.6: Distributions of dilepton invariant mass $M_{lep1,lep2}$ in the (a) *Z-enriched* and (b) *Z-depleted* samples. In figure only MC events are presented in order to show the distribution for each source of background. The signal events, considered as SM Higgs boson for a mass hypothesis of 125 GeV, are multiplied by a factor 20 and superimposed. The different sources of background are stacked. In plots the statistical error is presented for each bin.

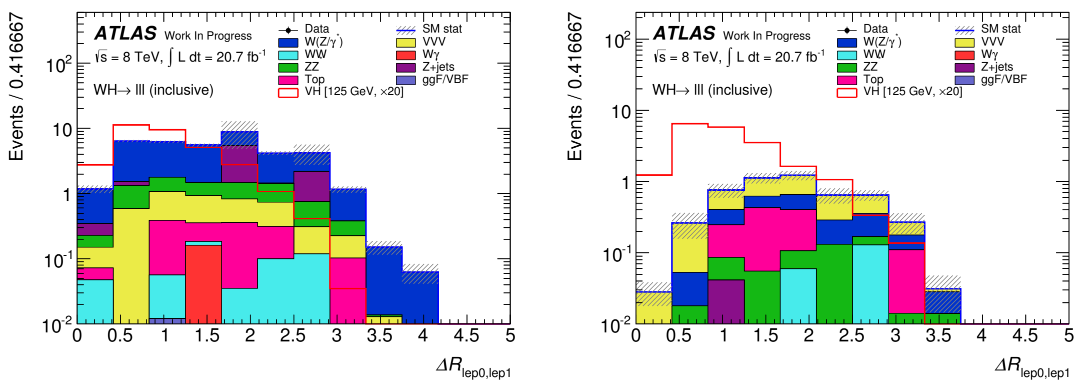

(a) (b)

Figure 5.7: Distributions of $\Delta R(lep_0, lep_1)$ in the (a) *Z-enriched* and (b) *Z-depleted* samples before the $\Delta R(lep_0, lep_1)$ selection. In figure only MC events are presented in order to show the distribution for each source of background. The signal events, considered as SM Higgs boson for a mass hypothesis of 125 GeV, are multiplied by a factor 20 and superimposed. The different sources of background are stacked. In plots the statistical error is presented for each bin.

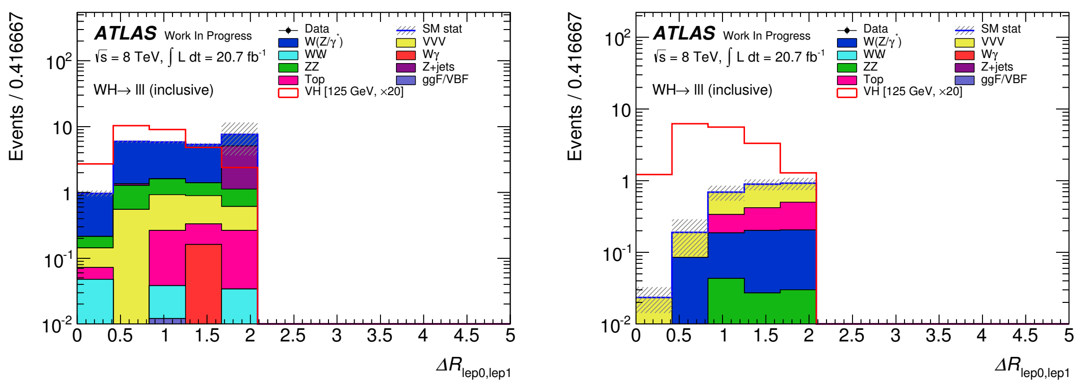

(a) (b)

Figure 5.8: Distributions of $\Delta R(lep_0, lep_1)$ in the (a) *Z-enriched* and (b) *Z-depleted* samples after the overlap removal with the 2-lept on analysis. In figure only MC events are presented in order to show the distribution for each source of background. The signal events, considered as SM Higgs boson for a mass hypothesis of 125 GeV, are multiplied by a factor 20 and superimposed. The different sources of background are stacked. In plots the statistical error is presented for each bin.

Z-depleted and *Z-enriched* signal regions. Moreover the *Z-enriched* signal region will be splitted in two signal regions, according to the number of SFOS lepton pairs.

Signal Selections		
Cut	*Z-enriched*	*Z-depleted*
Jet multiplicity	$N_{jet} \leq 1$	
b-veto	$N_{b-\mathrm{tag}} = 0$	
$E_{T,rel}^{Miss}$ cut	$E_{T,rel}^{Miss} > 40$ GeV	$E_{T,rel}^{Miss} > 25$ GeV
Dilepton mass cuts	$\|m_{ll} - m_Z\| > 25$ GeV and $m_{ll} > 12$ GeV	$m_{ll} > 12$ GeV
Angular cut	$\Delta R_{01} < 2.0$	
Overlap removal	remove overlap with $H \to WW^{(*)}$ analysis [61]	

Table 5.3: Summary of the selection criteria defining the 3-lepton signal regions.

5.6 Control Samples

In this section a method to verify the modeling of the MC samples will be discussed. This is a crucial point for all the high energy physics experiments and in particular in analyses in which the number of signal and background events expected is small. In general to observe the presence of a new particle, such as the Higgs boson, it is necessary to observe a discrepancy between the expected events, in case of no signal events, and the data observed. In this kind of approach the modeling of the background composition becomes really important. Not taking into account possible mismodelings could affect the result and create discrepancies between data and MC, faking the presence of new particles. There are several methods to analyze the reliability of simulated samples and this analysis is based on the Control Region (CR). In this method regions orthogonal to the signal regions, described in section 5.5, are defined. Each CR is dominated by a background source. In each region the ratio between the observed data and the number of expected simulated events is checked and a scale factor (SF) is computed. This SF is then applied to scale the MC prediction in the the signal region. In general the SF is computed as:

$$SF = \frac{SimulatedEvents(MC)}{DataEvents(data)} \tag{5.3}$$

but in this analysis, as explained below, a more precise computation is performed, taking into account several control regions in the same calculation.

5.6.1 Control Regions

Background contributions to final states with three isolated leptons are mainly WZ$^{(*)}$, ZZ$^{(*)}$, Z+jets and Top. In order to verify the modeling, in particular the normalization, of these components by the simulation, CRs have been defined with selections aimed at ensuring high purity for the background under study and orthogonality between the CR and signal regions. Three CRs are built to directly normalize the three major backgrounds, the fourth is meant to bound the ZZ$^{(*)}$ contribution whose normalization is correlated to the Z+jets one. Due to the topology of the backgrounds all the CRs are defined for the *Z-enriched* region. Nevertheless all the SF computed in the several regions are applied also to the *Z-depleted* events since the control sample analysis aim to cure possible mismodeling of the backgrounds, mismodeling that can appear in both the signal regions. However the introduction of the *Z-depleted* events in the SF calculation was tested and, due to the low number of WZ$^{(*)}$, ZZ$^{(*)}$, Z+jets and Top events in this region, the effect of the normalization was found negligible. In the next sections a brief description of the selections used to define the CRs is reported. Each control region is constructed to be as close as possible to the signal region so most of the selection criteria are shared between signal and control regions. This choice has been made to avoid SF extrapolation problem between the regions. More the CRs are close to the signal region less the impact of a different phase space is relevant for the SF value. Table 5.4 summarizes the selections defining the control regions.

WZ$^{(*)}$ CR

The WZ$^{(*)}$ CR is obtained selecting events with the same criteria of the *Z-enriched*, with the exception of the Z veto and $E_{T,rel}^{Miss}$ selections. The request of at most one jet with $p_T > 25$ GeV and not b-tagged suppresses the Top background while the cut on the smallest invariant mass of opposite sign leptons, independently of their flavor, suppresses the Drell-Yan background. To obtain a CR in a phase space close to SR, hence avoid extrapolation problem, the selection on the opening angle between lep_0 and lep_1 it is the same described in 5.5. Due to the presence of a Z boson, the Z mass pole selection in the WZ$^{(*)}$ CR is reverted compared to the signal region. This selection allows the WZ$^{(*)}$ CR to be orthogonal to the signal region and rich in WZ$^{(*)}$ events, usually suppressed by the Z veto. Reverting the Z mass pole selection, other Z-related background, in particular ZZ$^{(*)}$ and Z+jets, enter in the WZ$^{(*)}$ CR making the CR less pure. To suppress these background sources a selection on the missing transverse momentum is applied. In particular instead of the usual $E_{T,rel}^{Miss} > 40$ GeV used in the signal region, for the WZ$^{(*)}$ CR $E_{T,rel}^{Miss} > 25$ GeV is used. The value is chosen to take into account the purity of the CR (remove most of the ZZ$^{(*)}$ and Z+jets events) and the number of WZ$^{(*)}$ events in the CR.

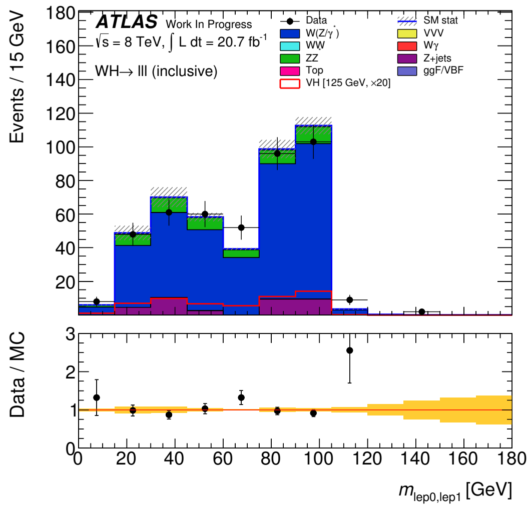

Figure 5.9: Distribution of the invariant mass of the lepton pair with smaller ΔR in the WZ$^{(*)}$ control region. Data (dots) are compared to expectations from the simulation of the background components (stacked filled histograms). Expectations for a Standard Model Higgs boson of mass $m_H = 125$ GeV are multiplied by a factor 20 and are presented as a non-stacked histogram (red line). In the bottom part of the plot the ratio between observed and expected events is presented. The error on dots is the statistical error on the data while the statistical simulation error is described by the yellow shadow.

ZZ$^{(*)}$ CR

The ZZ$^{(*)}$ is obtained selecting events with the same criteria of the *Z-enriched*, with the exception of the Z veto, the $E_{T,rel}^{Miss}$ and of the trilepton invariant mass selections. As in the previous CR the request of at most one jet with $p_T > 25$ GeV and not b-tagged to suppress the Top background and on the smallest invariant mass of opposite sign leptons, independently of their flavor, to suppress the Drell-Yan background, is applied. For the same reason of the WZ$^{(*)}$ CR a $\Delta R_{lep_0,lep_1} < 2$ selection is performed. Differently from the WZ$^{(*)}$ CR in this control region no Z mass pole selections are made, neither Z veto nor a reverted Z veto. Requiring no selection on the Z mass pole makes the ZZ$^{(*)}$ CR rich in ZZ$^{(*)}$, WZ$^{(*)}$ and Z+jets events. To suppress the

WZ$^{(*)}$ and to remain orthogonal to the signal region the selection on the $E_{T,rel}^{Miss}$ is reverted. The ZZ$^{(*)}$ CR is then obtained selecting the events in which the invariant mass of the three leptons is close to the Z mass ($|M_{lll} - M_Z| < 15$ GeV). This CR is populated mainly by Zγ events (included in the Z+jets simulated sample) but contains also a contribution from ZZ$^{(*)}$ due to "single resonant" Z decay with the loss of one of the four leptons.

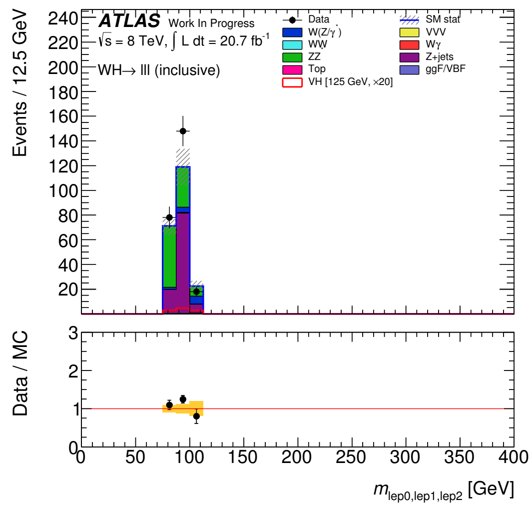

Figure 5.10: Distribution of the invariant mass of the three leptons in the ZZ$^{(*)}$ control region. Data (dots) are compared to expectations from the simulation of the background components (stacked filled histograms). Expectations for a Standard Model Higgs boson of mass m_H = 125 GeV are multiplied by a factor 20 and are presented as a non-stacked histogram (red line). In the bottom part of the plot the ratio between observed and expected events is presented. The error on dots is the statistical error on the data while the statistical simulation error is described by the yellow shadow.

Z+jets CR

Due to the similar topology of events and to the presence of Zγ sample in the Z+jets background definition, the Z+jets CR and the ZZ$^{(*)}$ CR share most of the selections. In particular the selections on jets activities, smallest invariant mass of opposite sign leptons and $\Delta R_{lep_0,lep_1}$ are the same. These two control regions share also the $E_{T,rel}^{Miss}$

selection. This selection allows the Z+jets CR to be orthogonal to the signal region and removes a great part of the $WZ^{(*)}$ events. Differently from the $ZZ^{(*)}$ CR, in this control region a three lepton invariant mass selection is not applied. To select events near to the Z mass pole a reverted Z mass selection, like in the $WZ^{(*)}$ control region, is applied.

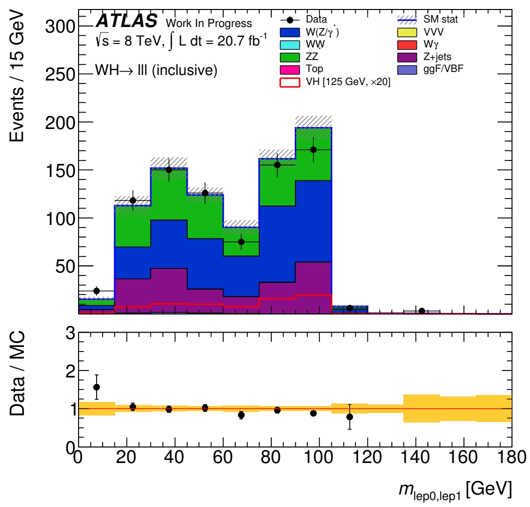

Figure 5.11: Distribution of the invariant mass of the lepton pair with smaller ΔR in the Z+jets control region. Data (dots) are compared to expectations from the simulation of the background components (stacked filled histograms). Expectations for a Standard Model Higgs boson of mass $m_H = 125$ GeV are multiplied by a factor 20 and are presented as a non-stacked histogram (red line). In the bottom part of the plot the ratio between observed and expected events is presented. The error on dots is the statistical error on the data while the statistical simulation error is described by the yellow shadow.

Top

The Top CR is obtained using the same topological selections of the *Z-enriched* signal region but for the requirements on the jet activity. In particular in the Top control region, in which both the single top and the $t\bar{t}$ contribute, at least one jet with $p_T > 25$ GeV is required to take into account the high hadronic activity of these samples moreover this jet should be b-tagged to account for the presence of a b quark in each top decay. Additionally, due to the topology of the top quark decay, mainly in $t \to W + b$, at least one b-tagged jet with $p_T > 25$ GeV is required. Due to the isolation criteria, required at the pre-selection stage, the top and the $t\bar{t}$ events are suppressed. For this reason the Top CR is poor in statistics. However the requirements of high jet activity and at least one b-tagged jet suppress all the other sources of background. This allow the Top CR to have a pure Top background composition.

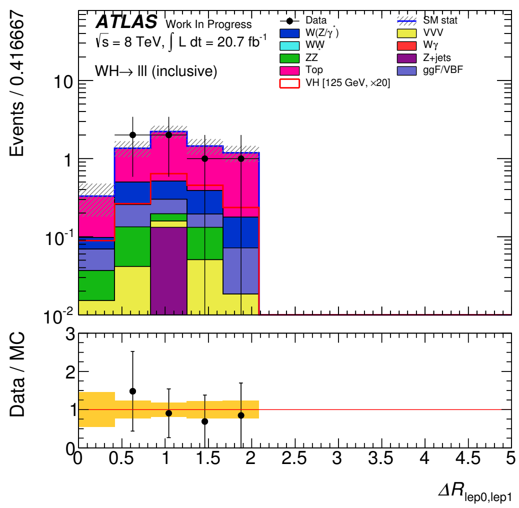

Figure 5.12: Distribution of the distance in ΔR of the lepton pair with smaller ΔR in Top CR. Data (dots) are compared to expectations from the simulation of the background components (stacked filled histograms). Expectations for a Standard Model Higgs boson of mass $m_H = 125$ GeV are multiplied by a factor 20 and are presented as a non-stacked histogram (red line). In the bottom part of the plot the ratio between observed and expected events is presented. The error on dots is the statistical error on the data while the statistical simulation error is described by the yellow shadow.

Control Region	Selections	
$WZ^{(*)}$ CR	at most one jet with $p_T > 25$ GeV;	$E_{T,rel}^{Miss} > 25$ GeV at least one SFOS lepton pair with $\lvert m_{ll} - m_Z \rvert < 25$ GeV
$ZZ^{(*)}$ CR	no b-tagged jets with $p_T > 25$ GeV;	$E_{T,rel}^{Miss} < 40$ GeV $\lvert m_{lll} - m_Z \rvert < 15$ GeV
Z+jets CR	$m_{ll,min} > 12$ GeV; $\Delta R_{01} < 2.0$	$E_{T,rel}^{Miss} < 40$ GeV; at least one SFOS lepton pair with $\lvert m_{ll} - m_Z \rvert < 25$ GeV
Top CR	at least one b-tagged jet with $p_T > 25$ GeV $m_{ll,min} > 12$ GeV; $\Delta R_{01} < 2.0$	$E_{T,rel}^{Miss} > 40$ GeV all SFOS lepton pairs with $\lvert m_{ll} - m_Z \rvert > 25$ GeV

Table 5.4: Summary of the selection criteria defining the control regions. A bar over a selection means that it is reversed compared with the signal selection.

5.6.2 The Scale Factors calculation procedure

As described before, a scale factor for a certain background is obtained by the ratio between the expected simulated events and the data in the corresponding background control region. For example the $\mathrm{SF}_{WZ^{(*)}}$ could be extracted from the $\mathrm{WZ}^{(*)}$ CR according to the equation 5.3. To take into account the contamination of different backgrounds in several control regions, a simultaneous fit, taking into account all the information coming from the CRs described above, is performed. Since the Z+jets background is expected to be significantly different between the case with a fake electron and a fake muon, two different scale factors, SF_e and SF_μ, have been introduced. They will be applied to the $N_e = N_{\mu\mu e} + N_{eee}$ and to $N_\mu = N_{\mu\mu\mu} + N_{ee\mu}$ samples respectively. The samples division has not be applied to the Top control region since it is not enough populated. The scale factors are then computed by a χ^2 minimization of the differences between the number of events in MC and data in all the above defined control regions through the procedure shown below.

$$\chi^2 = \sum_{all\ samples, all\ CR} \left(N_l^{data} - N_l^{MC} \right) / error, \qquad l = e, \mu \tag{5.4}$$

where the sum is done on all control regions and samples ($\mu\mu e + eee$, $\mu\mu\mu + ee\mu$) considered, and

$$N_l^{MC} = N_l^{Zjets} \cdot SF_l^{Zjets} + N_l^{ZZ^{(*)}} \cdot SF^{ZZ^{(*)}} + N_l^{WZ^{(*)}} \cdot SF^{WZ^{(*)}} + N_l^{Top} \cdot SF^{Top} \tag{5.5}$$

with l = e, μ. Only for Top control region

$$N^{MC} = N^{Zjets} \cdot \frac{1}{2}(SF_e^{Zjets} + SF_\mu^{Zjets}) + N^{ZZ^{(*)}} \cdot SF^{ZZ^{(*)}} + N^{WZ^{(*)}} \cdot SF^{WZ^{(*)}} \tag{5.6}$$

Table 5.5 summarizes the minimized scale factors as obtained by the simultaneous fit procedure. Statistical and systematic uncertainties are quoted. The systematic error is computed studying the result of the fit procedure for all the experimental systematics variations described in section 5.10. All the results obtained for a certain SF, considered together, give a Gaussian like distribution. The error quoted as systematic, for each SF, is the standard deviation of the Gaussian obtained with this procedure. The statistical error is computed studying the χ^2 distribution obtained by the fit. In particular the error quoted in the table is the SF variation obtained varying the χ^2 distribution around the minimum found by the simultaneous fit. This procedure is applied for all the SF separately.

$WZ^{(*)}$	$0.92 \pm 0.03 \pm 0.02$
$ZZ^{(*)}$	$2.33 \pm 0.30 \pm 0.10$
Z+jets (electrons)	$0.72^{+0.1}_{-0.03} \pm 0.04$
Z+jets (muons)	$0.76 \pm 0.80 \pm 0.04$
Top	$1.15 \pm 0.70 \pm 0.03$

Table 5.5: The scale factors used in the analysis for relevant samples. The normalization of the component in the *Z-depleted* region is taken from the estimation performed in the *Z-enriched* one. The quoted uncertainties include both statistical (first) and systematic (second) uncertainties.

The expected background composition after the application of the normalization factors described in table 5.5, the expected signal contamination and the data observed in the four CRs are presented in table 5.6.

Figure 5.13 details the expected composition in each CR.

Check on the scale factor calculation

Due the relevant impact of SF values on the analysis, several checks have been performed. First of all, correlations between the several scale factors have been analyzed but they appear to be negligible. The main one being the anti-correlation between the Z+jets and the $ZZ^{(*)}$ components which is however small and will not be taken into account in the final statistical treatment. Another check performed was on the large value of the $ZZ^{(*)}$ SF. A large normalization factor on the $ZZ^{(*)}$ component was expected. In this analysis, where the final state is composed by three leptons, the $ZZ^{(*)}$ background contributes when one of the leptons is lost. The MC simulated sample used has a cut on the mass of the $Z/\gamma^{(*)}$ above 4 GeV. A large contribution from very low mass $Z/\gamma^{(*)}$, a phase space in which there is a high probability to lose a lepton, was therefore not included. This is confirmed by the analysis of three lepton events included in the $ZZ^{(*)}$ control region in presence of a 4^{th} lepton candidate with looser lepton and isolation criteria.

	Data	MC	Data/MC	VVV	$WZ^{(*)}$	WW	$ZZ^{(*)}$	Z+jets	Top
$WZ^{(*)}$ CR	439	438 ± 24	1.00 ± 0.07	2.95 ± 0.13	350 ± 10	0.21 ± 0.12	48 ± 4	36 ± 13	0.8 ± 0.4
$ZZ^{(*)}$ CR	244	210 ± 40	1.15 ± 0.23	0.25 ± 0.04	12.3 ± 0.7	0.05 ± 0.05	90 ± 4	110 ± 40	0.57 ± 0.29
Z+jets CR	828	860 ± 40	0.96 ± 0.06	1.7 ± 0.1	351 ± 9	0.02 ± 0.04	290 ± 10	216 ± 30	0.50 ± 0.34
Top CR	6	6.2 ± 1.1	1.0 ± 0.4	0.15 ± 0.04	0.78 ± 0.31	0.00 ± 0.00	0.23 ± 0.08	0.13 ± 0.13	4.8 ± 0.8

Table 5.6: Number of observed events in data for the CRs compared to the total number of expected events normalized by the factors given in table 5.5 (indicated here as "MC"). The quoted uncertainties include both statistical and experimental systematic (described in section 5.10) uncertainties.

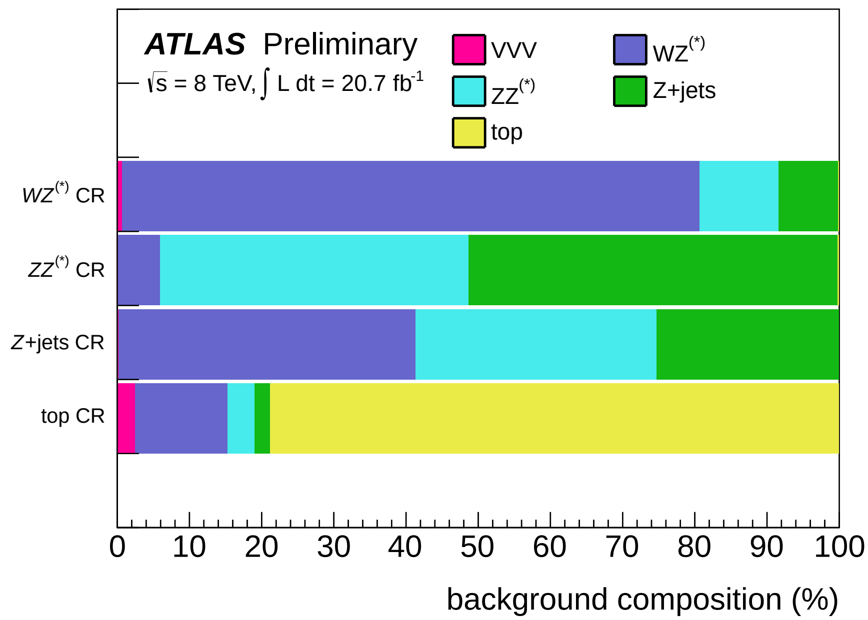

Figure 5.13: Expected background composition in each CR. Only the major background sources are shown. The contributions from other backgrounds and the VH signal are expected to be well below 1% in the $WZ^{(*)}$, $ZZ^{(*)}$ and Z+jets CRs, and at the level of 1% in the Top CR.

5.7 Blind analysis

The search for the Higgs boson produced in the associated modes deals with the very limited production cross-section and branching ratio of the signal and not small backgrounds. Excesses or deficits observed in the data with respect to the expectations may drive a fine tuning of the selections resulting in a biased result. In this analysis the samples have been "blinded" by removing from the data and MC samples all the events fulfilling the requirements for the signal regions, defined by applying simultaneously all the set of selections listed in table 5.3. As discussed in the previous section, most of the major background expectations are normalized to data in control regions. Control regions are all orthogonal to the signal regions hence no events are removed from the scale factor calculation because of the blinding, neither for data nor for simulation. In the following, the scale factors derived with the simultaneous fit using several control regions are applied to $W(Z/\gamma^{(*)})$, $ZZ^{(*)}$, Z+jets and Top simulated samples in all the plots and tables for both the *Z-enriched* and *Z-depleted*. Tables 5.7 and 5.8 summarize the event yield at the each stage of the selection with the signal regions blinded. The comparison with expectations from the Standard Model background processes is also shown.

As shown by table 5.7 after the first selections the events in the *Z-depleted* region are so few that it is difficult to assess whether the data follow the expectations or not. Figure 5.14 shows data to expectations comparison for the b-tagged jet multiplicity and the b-tagging flavor weight in the *Z-enriched* sample after requiring that the number of jets is less than or equal to one (Cut 1). Figure 5.15 shows data to expectations comparison for the transverse momentum, the pseudo-rapidity and azimuthal angle of jets in the *Z-enriched* sample after vetoing events with b-tagged jets (Cut 2). Figure 5.16 shows data to MC expectations comparison for the invariant mass of lep_0, lep_1 and lep_2 in the *Z-enriched* sample after requiring that the number of b-tagged jets equals to zero (Cut 2). The $ZZ^{(*)}$ control region is defined using this variable. Figures 5.17 to 5.22 present the distributions of the following lepton related quantities: the transverse momentum, the pseudo-rapidity, the azimuthal angle, the transverse impact parameter (d_0) significance, the colorimetric isolation variable and the tracking isolation variable, after vetoing the presence of b-tagged jets (Cut 2) for the *Z-enriched* sample. Each figure shows the properties of lep_0, lep_1 and lep_2 respectively.

Figures 5.23 to 5.28 present the distributions of the variables involved in the event selection, the $E_{T,rel}^{Miss}$ (both for *Z-enriched* and for *Z-depleted*), the invariant masses of pairs of leptons, the ΔR distances between pairs of leptons (both for *Z-enriched* and for *Z-depleted*) after the b-tagged jet veto (Cut 2) and the cut on $E_{T,rel}^{Miss}$ (Cut 3).

	$W(H \to WW)$	$Z(H \to WW)$	$W(H \to \tau\tau)$	$Z(H \to \tau\tau)$	VH	Obs.	Total Bkg.
Pre-selection	3.95 ± 0.12	10.26 ± 0.32	0.99 ± 0.05	0.85 ± 0.03	16.03 ± 0.44	3682	3342.51 ± 153.07
Z enriched $(eee + \mu\mu\mu)$	1.17 ± 0.05	4.99 ± 0.18	0.30 ± 0.02	0.39 ± 0.02	6.85 ± 0.21	1702	1603.56 ± 53.71
num. jets < 2 $(eee + \mu\mu\mu)$	1.01 ± 0.05	3.30 ± 0.16	0.25 ± 0.02	0.33 ± 0.02	4.89 ± 0.20	1377	1394.94 ± 52.50
top veto $(eee + \mu\mu\mu)$	0.97 ± 0.05	2.90 ± 0.15	0.24 ± 0.02	0.29 ± 0.02	4.40 ± 0.20	1312	1331.46 ± 53.87
$E_{T,Rel}^{miss} > 40$ GeV $(eee + \mu\mu\mu)$	0.30 ± 0.02	0.84 ± 0.07	0.05 ± 0.01	0.08 ± 0.01	1.27 ± 0.08	243	241.44 ± 11.67
Z mass veto $(eee + \mu\mu\mu)$	0.03 ± 0.01	0.01 ± 0.01	0.01 ± 0.00	0.00 ± 0.00	0.05 ± 0.01	5	4.90 ± 3.56
$m_{ll} > 12$ GeV $(eee + \mu\mu\mu)$	0.01 ± 0.00	0.01 ± 0.01	0.01 ± 0.00	0.00 ± 0.00	0.03 ± 0.01	3	3.57 ± 3.47
$\Delta R_{ll} < 2.0$ $(eee + \mu\mu\mu)$	0.00 ± 0.00	0.00 ± 0.00	0.00 ± 0.00	0.00 ± 0.00	0.00 ± 0.00	0	0.00 ± 0.00
lvlv OR $(eee + \mu\mu\mu)$	0.00 ± 0.00	0.00 ± 0.00	0.00 ± 0.00	0.00 ± 0.00	0.00 ± 0.00	0	0.00 ± 0.00
Z enriched $(ee\mu + \mu\mu e)$	2.10 ± 0.08	5.11 ± 0.20	0.49 ± 0.03	0.43 ± 0.02	8.13 ± 0.27	1952	1712.26 ± 117.99
num. jets < 2 $(ee\mu + \mu\mu e)$	1.77 ± 0.09	3.39 ± 0.19	0.44 ± 0.03	0.36 ± 0.02	5.96 ± 0.28	1546	1494.03 ± 116.97
top veto $(ee\mu + \mu\mu e)$	1.69 ± 0.09	3.02 ± 0.17	0.42 ± 0.03	0.32 ± 0.02	5.45 ± 0.26	1474	1431.34 ± 117.83
$E_{T,Rel}^{miss} > 40$ GeV $(ee\mu + \mu\mu e)$	0.36 ± 0.03	0.78 ± 0.07	0.05 ± 0.01	0.07 ± 0.01	1.26 ± 0.10	231	221.62 ± 12.36
Z mass veto $(ee\mu + \mu\mu e)$	0.08 ± 0.01	0.01 ± 0.01	0.01 ± 0.00	0.00 ± 0.00	0.11 ± 0.02	11	8.26 ± 2.13
$m_{ll} > 12$ GeV $(ee\mu + \mu\mu e)$	0.04 ± 0.01	0.01 ± 0.01	0.01 ± 0.00	0.00 ± 0.00	0.07 ± 0.01	8	7.12 ± 2.09
$\Delta R_{ll} < 2.0$ $(ee\mu + \mu\mu e)$	0.00 ± 0.00	0.00 ± 0.00	0.00 ± 0.00	0.00 ± 0.00	0.00 ± 0.00	0	0.00 ± 0.00
lvlv OR $(ee\mu + \mu\mu e)$	0.00 ± 0.00	0.00 ± 0.00	0.00 ± 0.00	0.00 ± 0.00	0.00 ± 0.00	0	0.00 ± 0.00
Z depleted	0.67 ± 0.04	0.16 ± 0.03	0.19 ± 0.02	0.02 ± 0.00	1.05 ± 0.06	28	26.70 ± 4.33
num. jets < 2	0.53 ± 0.04	0.07 ± 0.02	0.17 ± 0.02	0.02 ± 0.00	0.78 ± 0.05	8	15.41 ± 4.16
top veto	0.50 ± 0.03	0.06 ± 0.02	0.16 ± 0.02	0.02 ± 0.00	0.73 ± 0.05	6	11.79 ± 4.04
$E_{T,Rel}^{miss} > 25$ GeV	0.08 ± 0.01	0.01 ± 0.01	0.03 ± 0.01	0.00 ± 0.00	0.12 ± 0.02	2	1.82 ± 1.86
$m_{ll} > 12$ GeV	0.05 ± 0.01	0.01 ± 0.01	0.03 ± 0.01	0.00 ± 0.00	0.09 ± 0.01	2	1.80 ± 1.86
$\Delta R_{ll} < 2.0$	0.00 ± 0.00	0.00 ± 0.00	0.00 ± 0.00	0.00 ± 0.00	0.00 ± 0.00	0	0.00 ± 0.00
lvlv OR	0.00 ± 0.00	0.00 ± 0.00	0.00 ± 0.00	0.00 ± 0.00	0.00 ± 0.00	0	0.00 ± 0.00

Table 5.7: Blinded cutflow for the SM Higgs boson signal processes in three leptons final states. The number of observed events in data and expected events in the MC simulation is reported in the last two columns. The quoted uncertainties include both statistical and experimental systematic (described in section 5.10) uncertainties.

	VVV	$W(Z/\gamma^*)$	WW	ZZ^*	Z+jets	Top	$W\gamma$	$ggF \rightarrow ZZ$
Pre-selection	15.66 ± 0.42	1382.51 ± 26.87	1.51 ± 0.36	1008.74 ± 25.24	842.72 ± 102.39	80.71 ± 3.67	0.20 ± 0.16	10.13 ± 0.09
Z enriched ($eee + \mu\mu\mu$)	5.25 ± 0.16	712.05 ± 12.05	0.60 ± 0.19	505.76 ± 11.49	349.27 ± 36.31	25.20 ± 1.43	0.20 ± 0.16	5.16 ± 0.06
num. jets < 2 ($eee + \mu\mu\mu$)	4.47 ± 0.16	674.10 ± 12.42	0.43 ± 0.16	424.57 ± 11.49	281.98 ± 34.17	5.12 ± 0.93	0.20 ± 0.16	4.08 ± 0.06
top veto ($eee + \mu\mu\mu$)	4.15 ± 0.17	654.25 ± 14.88	0.43 ± 0.15	400.49 ± 11.63	266.31 ± 33.29	1.78 ± 0.63	0.20 ± 0.16	3.85 ± 0.05
$E_{T,Rel}^{miss} > 40$ GeV ($eee + \mu\mu\mu$)	1.86 ± 0.10	213.95 ± 5.48	0.25 ± 0.13	17.92 ± 1.67	6.74 ± 5.32	0.62 ± 0.49	0.00 ± 0.00	0.09 ± 0.01
Z mass veto ($eee + \mu\mu\mu$)	0.24 ± 0.04	3.51 ± 0.23	0.12 ± 0.08	0.96 ± 0.17	0.02 ± 3.20	0.06 ± 0.05	0.00 ± 0.00	0.00 ± 0.00
$m_{ll} > 12$ GeV ($eee + \mu\mu\mu$)	0.22 ± 0.03	2.47 ± 0.18	0.12 ± 0.08	0.67 ± 0.12	0.02 ± 3.20	0.06 ± 0.05	0.00 ± 0.00	0.00 ± 0.00
$\Delta R_{ll} < 2.0$ ($eee + \mu\mu\mu$)	0.00 ± 0.00	0.00 ± 0.00	0.00 ± 0.00	0.00 ± 0.00	0.00 ± 0.00	0.00 ± 0.00	0.00 ± 0.00	0.00 ± 0.00
lvlv OR ($eee + \mu\mu\mu$)	0.00 ± 0.00	0.00 ± 0.00	0.00 ± 0.00	0.00 ± 0.00	0.00 ± 0.00	0.00 ± 0.00	0.00 ± 0.00	0.00 ± 0.00
Z enriched ($ee\mu + \mu\mu e$)	7.87 ± 0.25	668.11 ± 15.06	0.46 ± 0.24	500.68 ± 13.90	487.79 ± 89.67	42.22 ± 2.55	0.00 ± 0.00	4.97 ± 0.06
num. jets < 2 ($ee\mu + \mu\mu e$)	6.85 ± 0.24	633.52 ± 14.97	0.33 ± 0.17	410.16 ± 13.92	428.41 ± 88.92	10.89 ± 1.76	0.00 ± 0.00	3.86 ± 0.05
top veto ($ee\mu + \mu\mu e$)	6.31 ± 0.24	614.75 ± 16.63	0.33 ± 0.17	382.59 ± 13.90	418.71 ± 88.47	5.02 ± 1.39	0.00 ± 0.00	3.63 ± 0.05
$E_{T,Rel}^{miss} > 40$ GeV ($ee\mu + \mu\mu e$)	2.58 ± 0.12	194.70 ± 6.09	0.15 ± 0.11	13.18 ± 1.25	8.97 ± 5.99	1.97 ± 0.99	0.00 ± 0.00	0.07 ± 0.01
Z mass veto ($ee\mu + \mu\mu e$)	0.71 ± 0.06	4.84 ± 0.29	0.10 ± 0.09	0.91 ± 0.15	1.43 ± 1.75	0.27 ± 0.31	0.00 ± 0.00	0.00 ± 0.00
$m_{ll} > 12$ GeV ($ee\mu + \mu\mu e$)	0.68 ± 0.06	3.92 ± 0.24	0.10 ± 0.09	0.73 ± 0.14	1.43 ± 1.75	0.25 ± 0.31	0.00 ± 0.00	0.00 ± 0.00
$\Delta R_{ll} < 2.0$ ($ee\mu + \mu\mu e$)	0.00 ± 0.00	0.00 ± 0.00	0.00 ± 0.00	0.00 ± 0.00	0.00 ± 0.00	0.00 ± 0.00	0.00 ± 0.00	0.00 ± 0.00
lvlv OR ($ee\mu + \mu\mu e$)	0.00 ± 0.00	0.00 ± 0.00	0.00 ± 0.00	0.00 ± 0.00	0.00 ± 0.00	0.00 ± 0.00	0.00 ± 0.00	0.00 ± 0.00
Z depleted	2.55 ± 0.12	2.36 ± 0.17	0.45 ± 0.19	2.30 ± 0.18	5.66 ± 4.03	13.28 ± 1.30	0.00 ± 0.00	0.01 ± 0.00
num. jets < 2	2.19 ± 0.11	2.14 ± 0.17	0.25 ± 0.13	1.77 ± 0.17	5.48 ± 4.04	3.57 ± 0.64	0.00 ± 0.00	0.01 ± 0.00
top veto	2.06 ± 0.11	2.08 ± 0.18	0.24 ± 0.12	1.61 ± 0.16	5.15 ± 3.96	0.64 ± 0.34	0.00 ± 0.00	0.01 ± 0.00
$E_{T,Rel}^{miss} > 25$ GeV	0.88 ± 0.07	0.57 ± 0.08	0.19 ± 0.12	0.20 ± 0.06	0.00 ± 0.00	-0.01 ± 1.72	0.00 ± 0.00	0.00 ± 0.00
$m_{ll} > 12$ GeV	0.85 ± 0.07	0.56 ± 0.08	0.19 ± 0.12	0.20 ± 0.06	0.00 ± 0.00	-0.01 ± 1.72	0.00 ± 0.00	0.00 ± 0.00
$\Delta R_{ll} < 2.0$	0.00 ± 0.00	0.00 ± 0.00	0.00 ± 0.00	0.00 ± 0.00	0.00 ± 0.00	0.00 ± 0.00	0.00 ± 0.00	0.00 ± 0.00
lvlv OR	0.00 ± 0.00	0.00 ± 0.00	0.00 ± 0.00	0.00 ± 0.00	0.00 ± 0.00	0.00 ± 0.00	0.00 ± 0.00	0.00 ± 0.00

Table 5.8: The blinded cutflow for the Monte Carlo background samples in three leptons final states. Z+jets contains the Z boson production associated with heavy flavor jets. Top contains $t\bar{t}$ and single top productions as well as the $t\bar{t}$ productions associated with a W or Z boson. The quoted uncertainties include both statistical and experimental systematic (described in section 5.10) uncertainties.

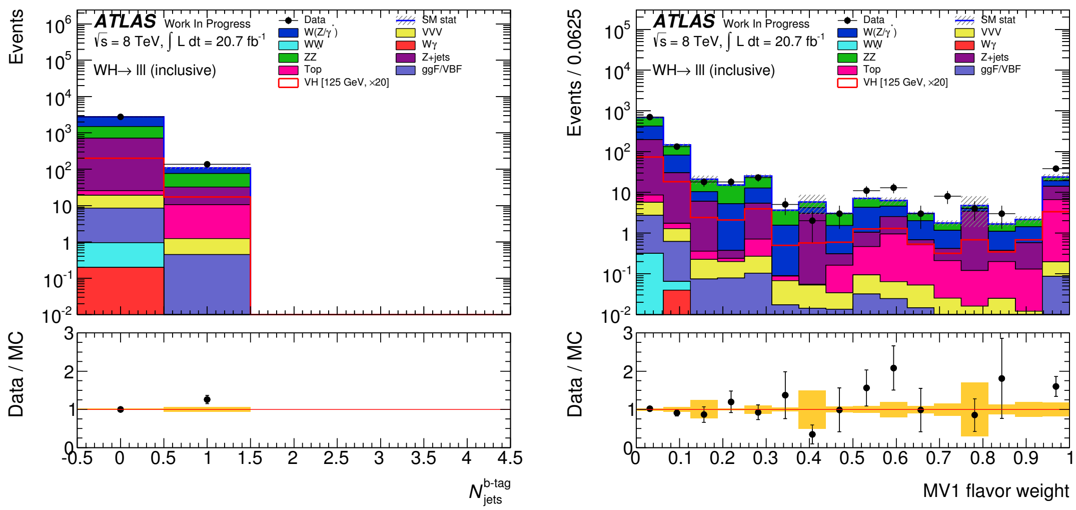

(a) (b)

Figure 5.14: Distribution of (a) the number of b-tagged jets with $p_T > 25$ GeV and (b) b-tagging flavor weight in the *Z-enriched* sample after the number of jets selection (Cut 1). Blinded data (dots) are compared to expectations from the simulation of the background components (stacked filled histograms). Expectations for the SM VH production with $m_H = 125$ GeV are multiplied by a factor 20 and presented as a non-stacked histogram (red line).

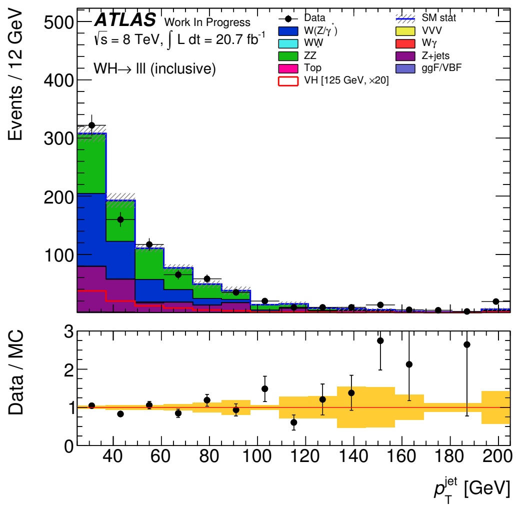

(a)

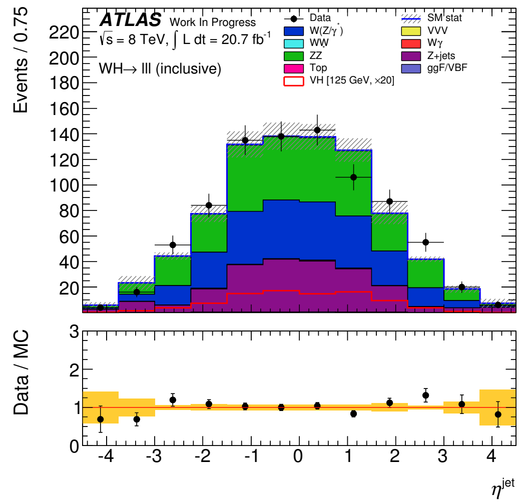

(b)

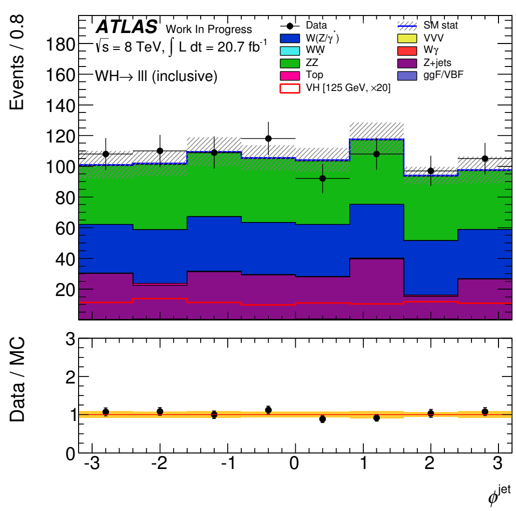

(c)

Figure 5.15: Distributions of (a) the transverse momenta, (b) the pseudo-rapidity and (c) the azimuthal angle of jets in the *Z-enriched* sample after vetoing the presence of b-tagged jets (Cut 2). Blinded data (dots) are compared to expectations from the simulation of the background components (stacked filled histograms). Expectations for the SM VH production with m_H = 125 GeV are multiplied by a factor 20 and presented as a non-stacked histogram (red line).

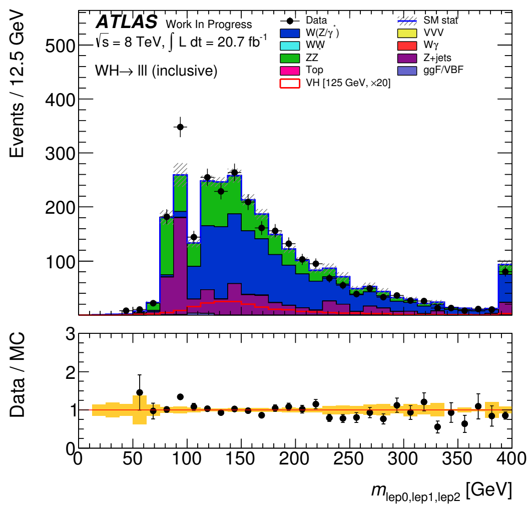

Figure 5.16: Distribution of the trilepton invariant mass in the *Z-enriched* sample after vetoing the presence of b-tagged jets (Cut 2). Blinded data (dots) are compared to expectations from the simulation of the background components (stacked filled histograms). Expectations for the SM VH production with $m_H = 125$ GeV are multiplied by a factor 20 and presented as a non-stacked histogram (red line).

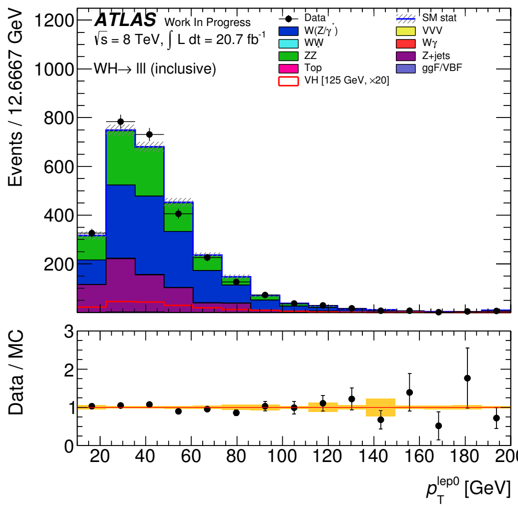

(a)

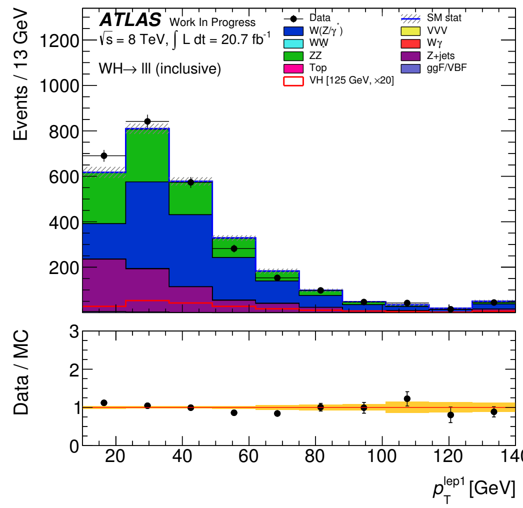

(b)

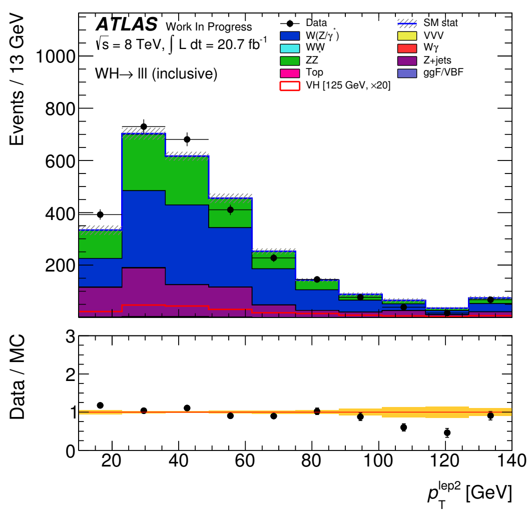

(c)

Figure 5.17: Distributions of the transverse momenta of (a) lep_0, (b) lep_1 and (c) lep_2 in the *Z-enriched* after vetoing the presence of b-tagged jets (Cut 2). Blinded data (dots) are compared to expectations from the simulation of the background components (stacked filled histograms). Expectations for the SM VH production with m_H = 125 GeV are multiplied by a factor 20 and presented as a non-stacked histogram (red line).

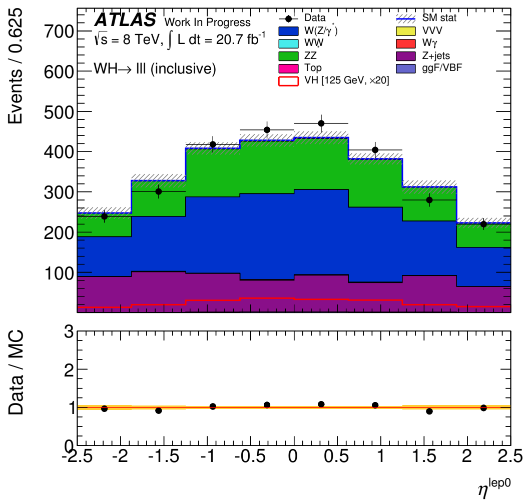

(a)

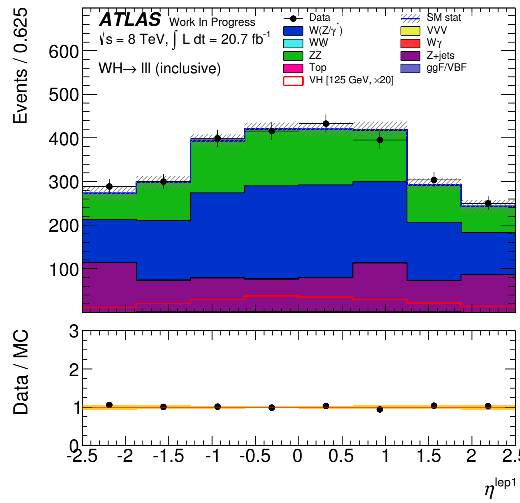

(b)

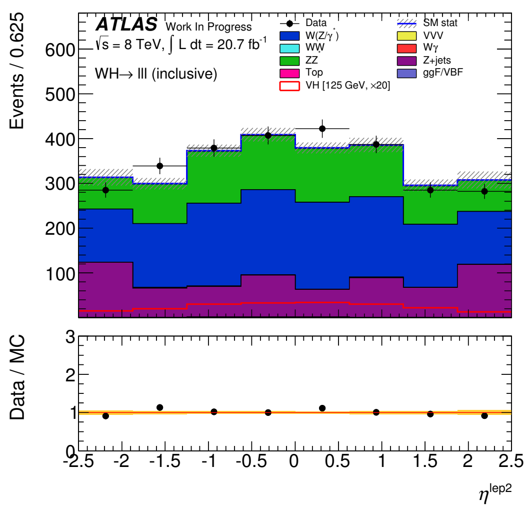

(c)

Figure 5.18: Distributions of the pseudo-rapidity of (a) lep_0, (b) lep_1 and (c) lep_2 in the *Z-enriched* sample after vetoing the presence of b-tagged jets (Cut 2). Blinded data (dots) are compared to expectations from the simulation of the background components (stacked filled histograms). Expectations for the SM VH production with $m_H = 125$ GeV are multiplied by a factor 20 and presented as a non-stacked histogram (red line).

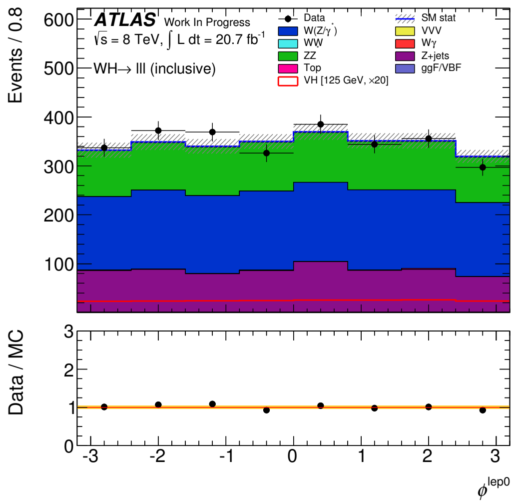

(a)

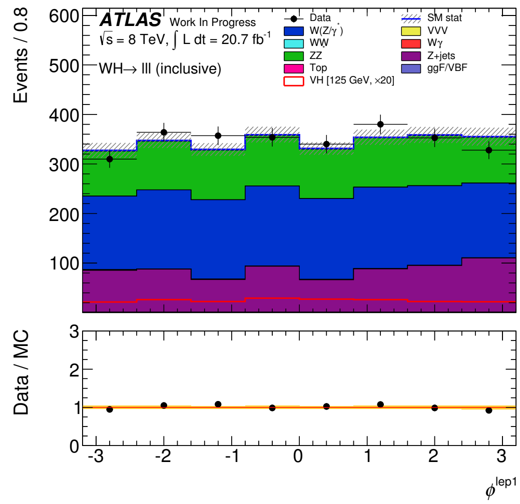

(b)

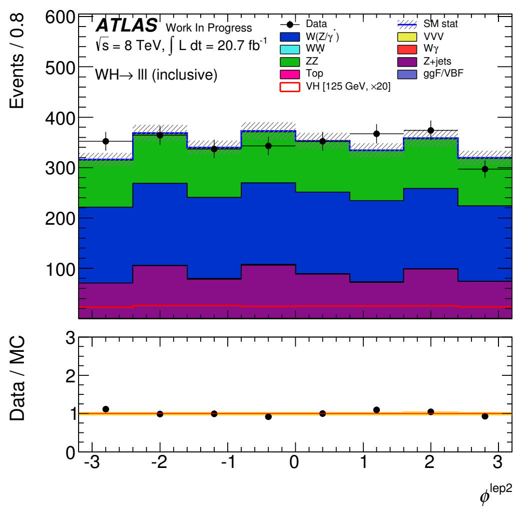

(c)

Figure 5.19: Distributions of the azimuthal angle of (a) lep_0, (b) lep_1 and (c) lep_2 in the *Z-enriched* sample after vetoing the presence of b-tagged jets (Cut 2). Blinded data (dots) are compared to expectations from the simulation of the background components (stacked filled histograms). Expectations for the SM VH production with m_H = 125 GeV are multiplied by a factor 20 and presented as a non-stacked histogram (red line).

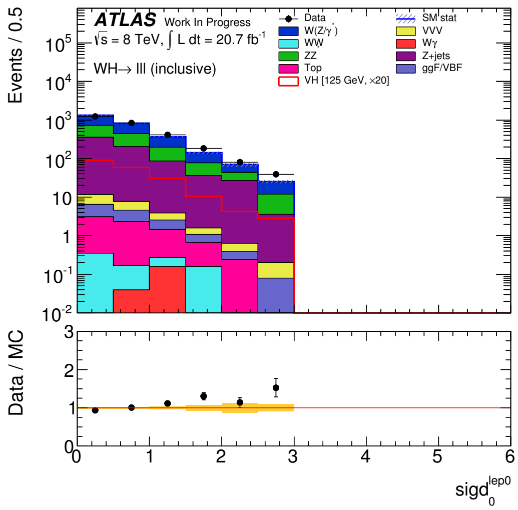

(a)

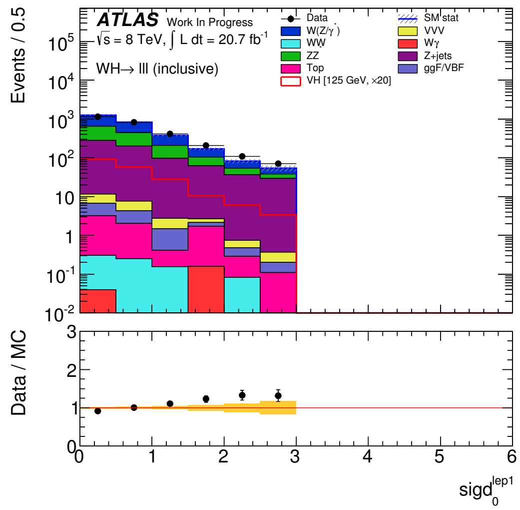

(b)

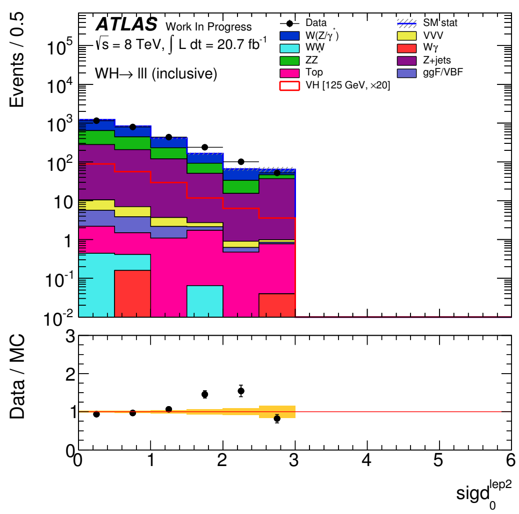

(c)

Figure 5.20: Distributions of the transverse impact parameter significance of (a) lep_0, (b) lep_1 and (c) lep_2 in the *Z-enriched* sample after vetoing the presence of b-tagged jets (Cut 2). Blinded data (dots) are compared to expectations from the simulation of the background components (stacked filled histograms). Expectations for the SM VH production with $m_H = 125$ GeV are multiplied by a factor 20 and presented as a non-stacked histogram (red line).

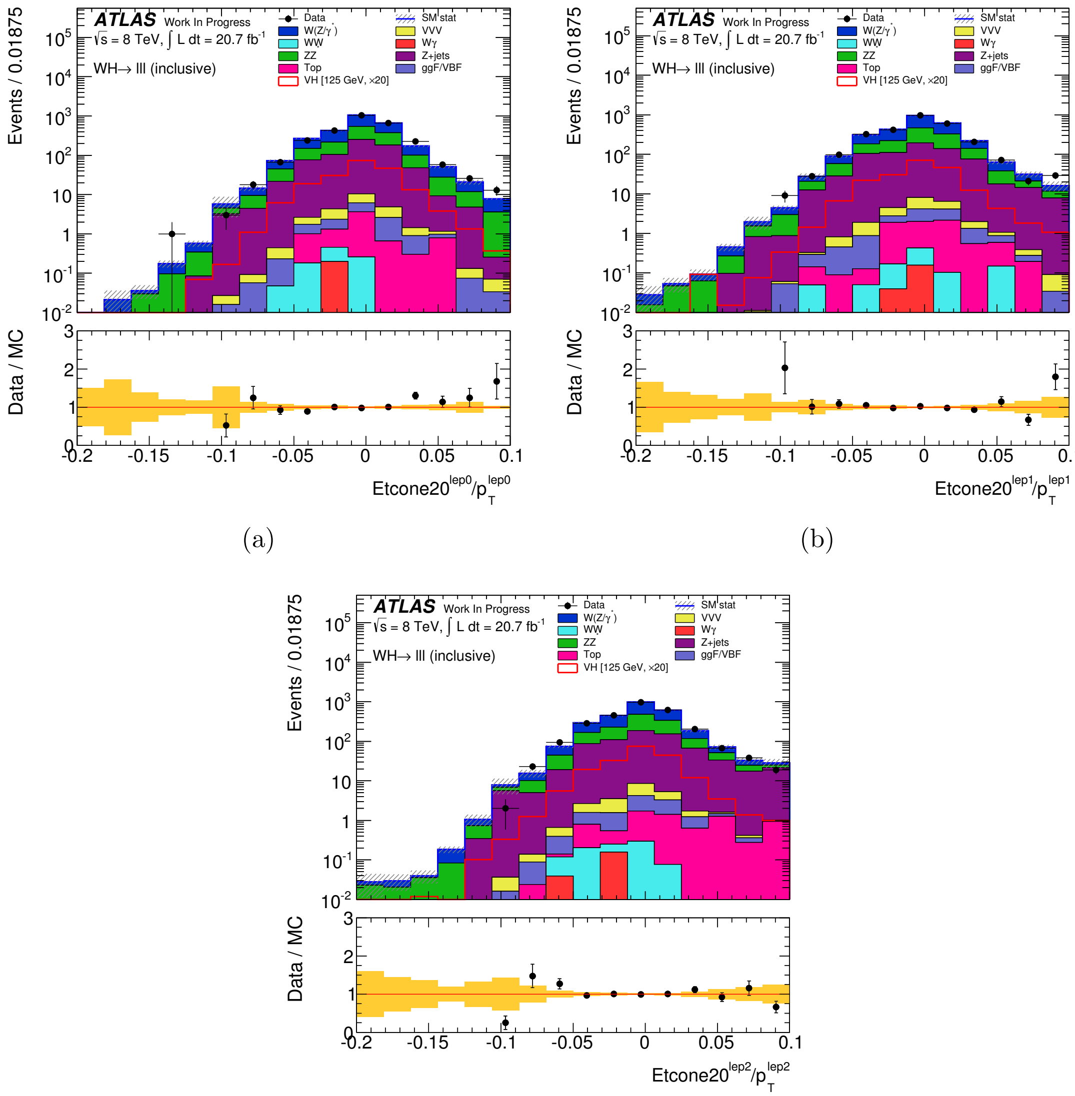

(a) (b)

(c)

Figure 5.21: Distributions of the calorimetric isolation variable of (a) lep_0, (b) lep_1 and (c) lep_2 in the *Z-enriched* sample after vetoing the presence of b-tagged jets (Cut 2). Blinded data (dots) are compared to expectations from the simulation of the background components (stacked filled histograms). Expectations for the SM VH production with m_H = 125 GeV are multiplied by a factor 20 and presented as a non-stacked histogram (red line).

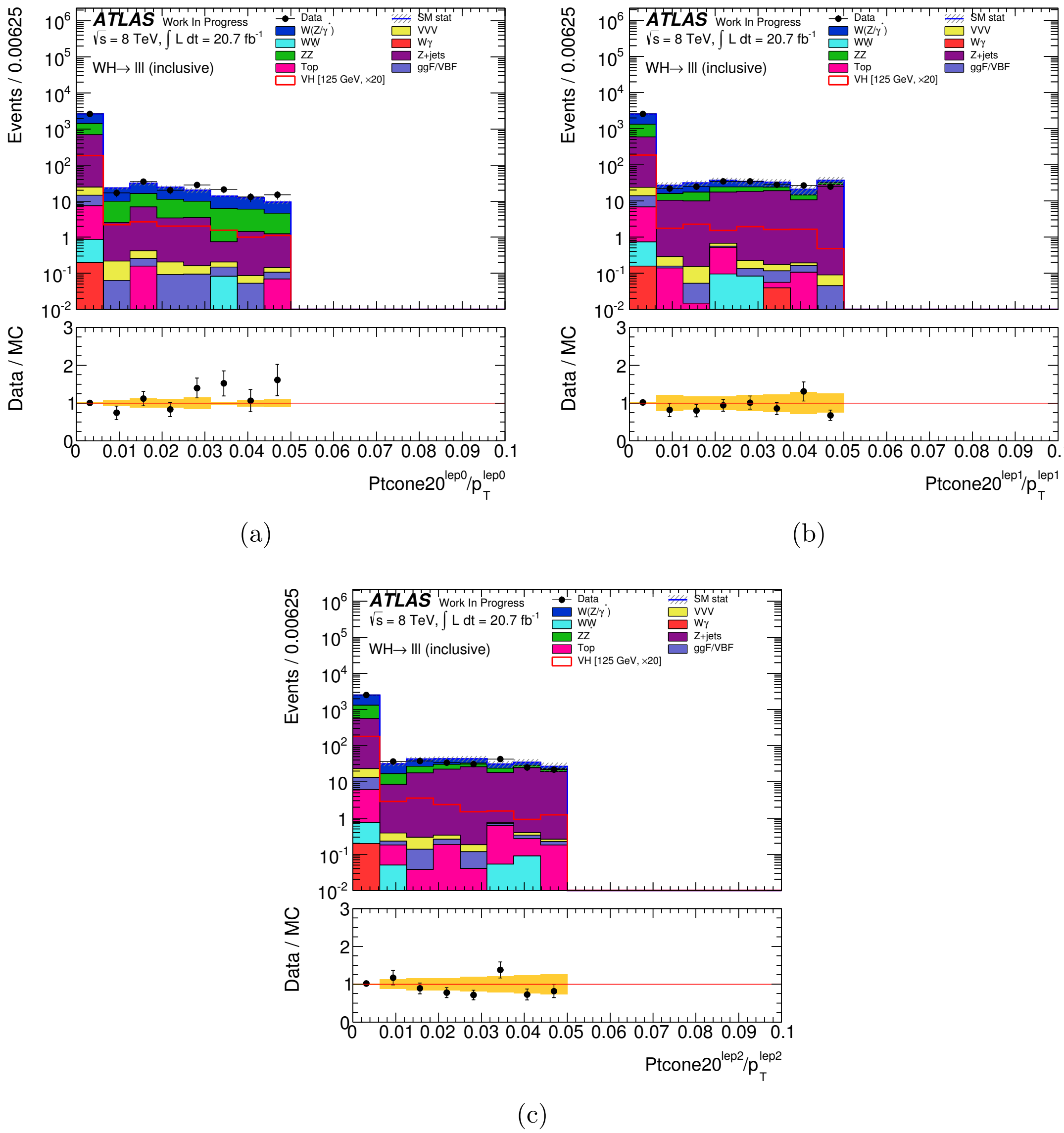

Figure 5.22: Distributions of the tracking isolation variable of (a) lep_0, (b) lep_1 and (c) lep_2 in the *Z-enriched* sample after vetoing the presence of b-tagged jets (Cut 2). Blinded data (dots) are compared to expectations from the simulation of the background components (stacked filled histograms). Expectations for the SM VH production with $m_H = 125$ GeV are multiplied by a factor 20 and presented as a non-stacked histogram (red line).

The blinded region is excluded from these plots both in data and MC.

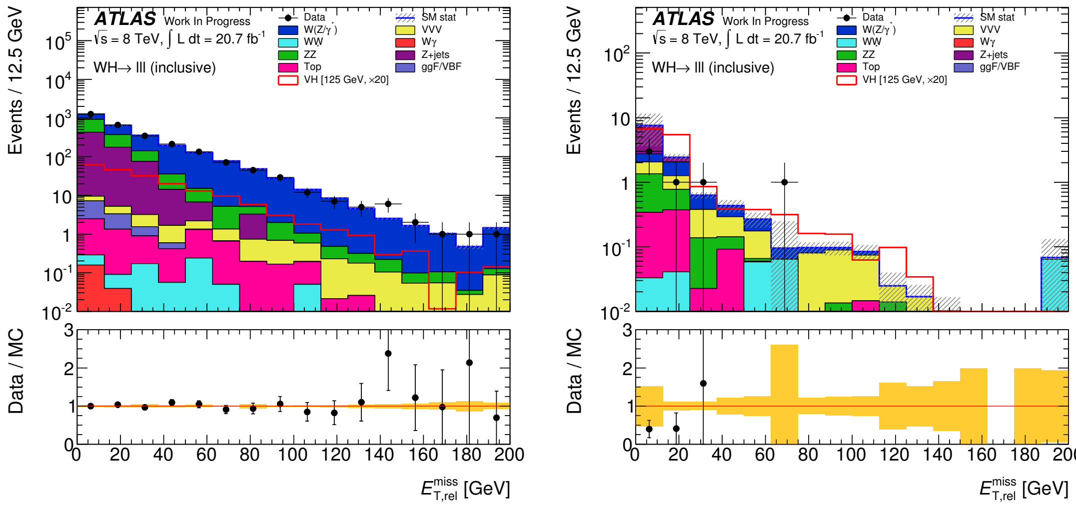

(a) (b)

Figure 5.23: Distributions of $E_{T,rel}^{Miss}$ in the (a) *Z-enriched* and (b) *Z-depleted* sample after vetoing the presence of b-tagged jets (Cut 2). Blinded data (dots) are compared to background expectation from the simulation of the background components (stacked filled histograms). Expectations for the SM VH production with $m_H = 125$ GeV are multiplied by a factor 20 and presented as a non-stacked histogram (red line).

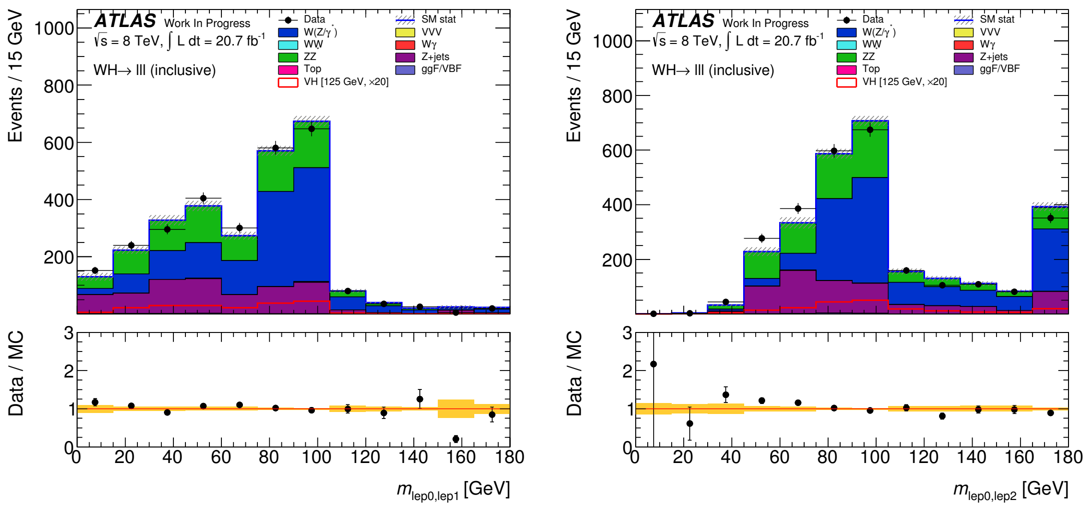

(a) (b)

Figure 5.24: Distributions of the invariant masses of the two opposite sign lepton pairs in the *Z-enriched* sample after vetoing the presence of b-tagged jets (Cut 2): (a) the pair with smaller distance ΔR and (b) the one with larger ΔR. Blinded data (dots) are compared to expectations from the simulation of the background components (stacked filled histograms). Expectations for the SM VH production with m_H = 125 GeV are multiplied by a factor 20 and presented as a non-stacked histogram (red line).

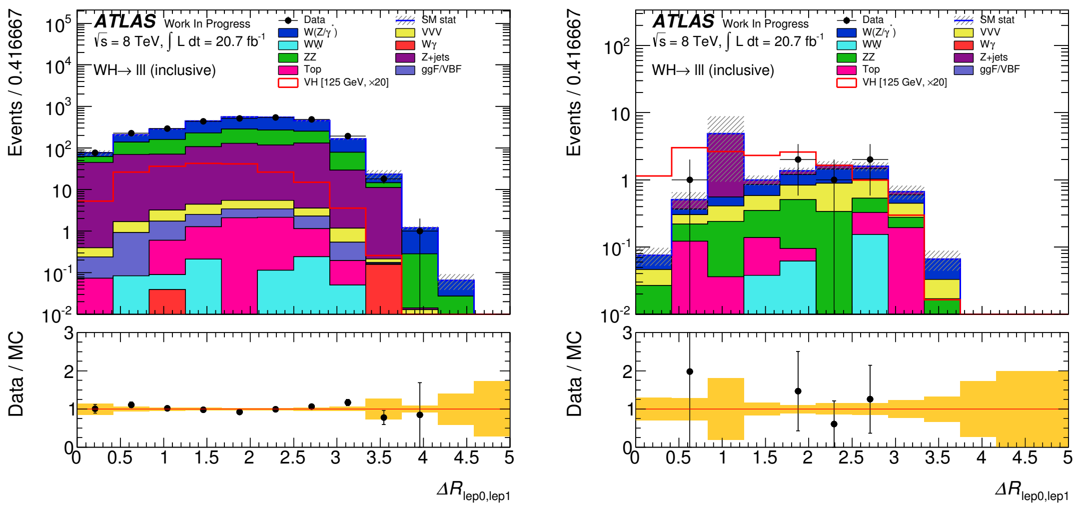

(a) (b)

Figure 5.25: Distributions of $\Delta R(lep_0, lep_1)$ in the (a) *Z-enriched* and (b) *Z-depleted* sample after vetoing the presence of b-tagged jets (Cut 2). Blinded data (dots) are compared to expectations from the simulation of the background components (stacked filled histograms). Expectations for the SM VH production with $m_H = 125$ GeV are multiplied by a factor 20 and presented as a non-stacked histogram (red line).

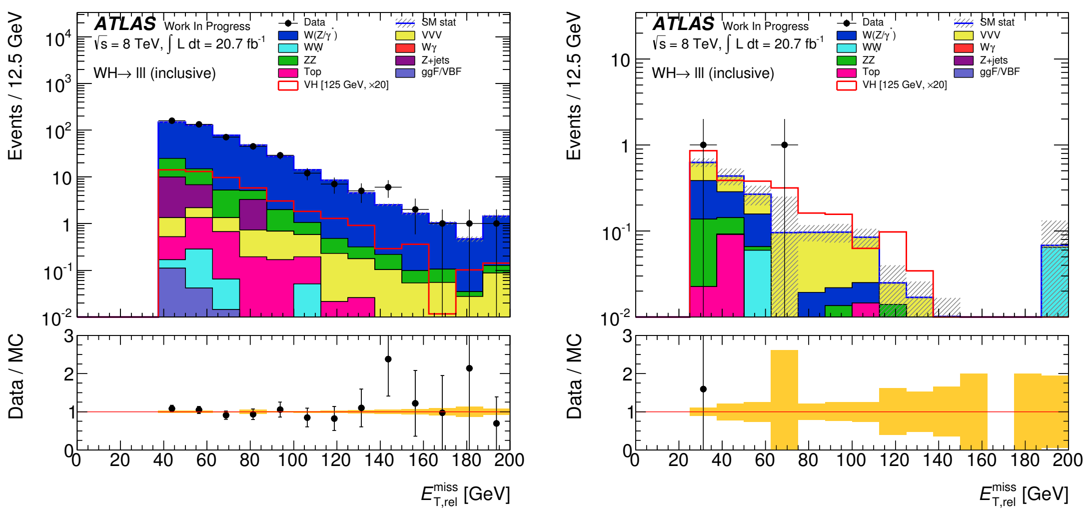

(a) (b)

Figure 5.26: Distributions of $E_{T,rel}^{Miss}$ in the (a) *Z-enriched* and (b) *Z-depleted* sample after the cut on $E_{T,rel}^{Miss}$ (Cut 3). Blinded data (dots) are compared to background expectation from the simulation of the background components (stacked filled histograms). Expectations for the SM VH production with $m_H = 125$ GeV are multiplied by a factor 20 and presented as a non-stacked histogram (red line).

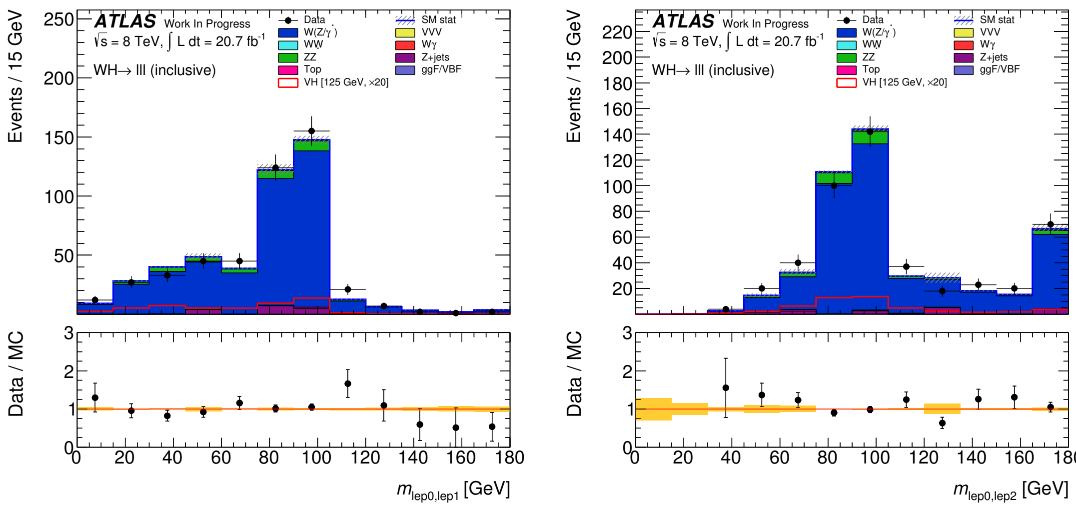

(a) (b)

Figure 5.27: Distributions of the invariant masses of the two opposite sign lepton pairs in the *Z-enriched* sample after the cut on $E_{T,rel}^{Miss}$ (Cut 3): (a) the pair with smaller distance ΔR and (b) the one with larger ΔR. Blinded data (dots) are compared to expectations from the simulation of the background components (stacked filled histograms). Expectations for the SM VH production with $m_H = 125$ GeV are multiplied by a factor 20 and presented as a non-stacked histogram (red line).

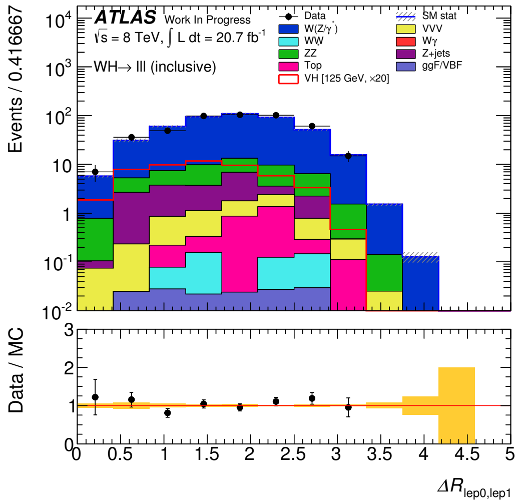

(a)

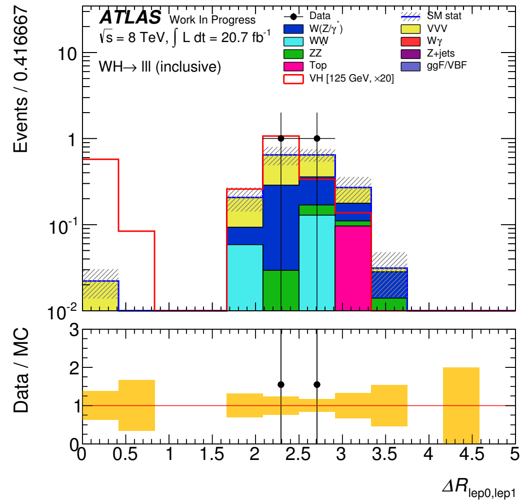

(b)

Figure 5.28: Distributions of $\Delta R(lep_0, lep_1)$ in the (a) *Z-enriched* and (b) *Z-depleted* sample after the cut on $E_{T,rel}^{Miss}$ (Cut 3). Blinded data (dots) are compared to expectations from the simulation of the background components (stacked filled histograms). Expectations for the SM VH production with $m_H = 125$ GeV are multiplied by a factor 20 and presented as a non-stacked histogram (red line).

5.8 Unblinded data comparison to expectations

In the last two sections several comparisons between data and MC simulation have been presented. Having established that there is a reasonable agreement between data and expectations in the control regions and with the blinded data, the blinding veto was removed and all data have been analyzed. Figures 5.29 to 5.42 present the distributions of the variables involved in the event selection for both *Z-enriched* and *Z-depleted*. Along the cutflow starting from the $E_{T,rel}^{Miss}$ (Cut 3) up to the overlap removal with the 2-lepton analysis (Cut 7) the $E_{T,rel}^{Miss}$ itself, the invariant masses of pairs of leptons, the ΔR distances between pairs of leptons are shown in the next pages. In table 5.9, splitted according to the regions, an unblinded comparison between data and simulations along all the cutflow is presented. All the possible contributions to the signal are taken into account while the backgrounds sources are added together in the “Total Background” column. The data observed are reported in the “Observed” column.

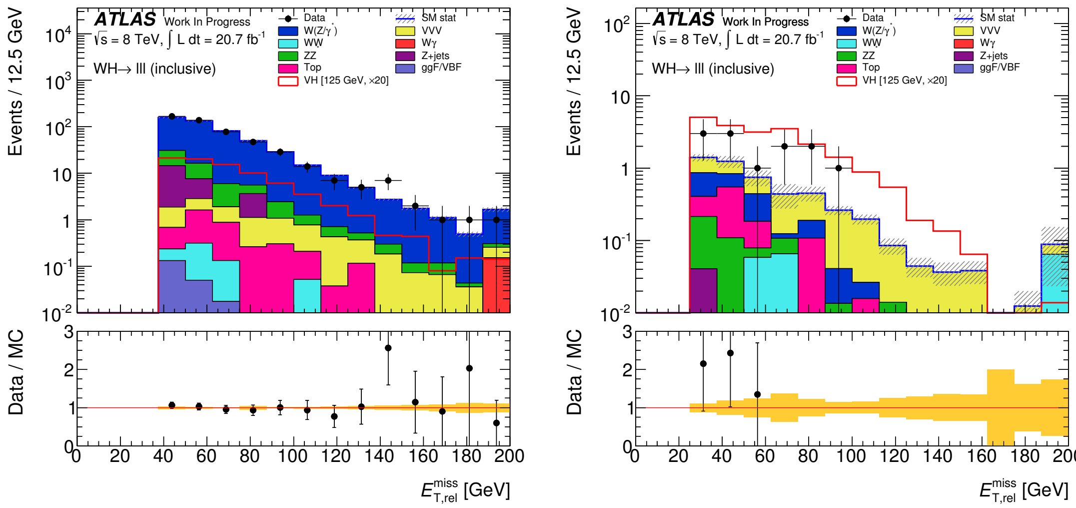

(a) (b)

Figure 5.29: Distributions of $E_{T,rel}^{Miss}$ in the (a) *Z-enriched* and (b) *Z-depleted* sample after the cut on $E_{T,rel}^{Miss}$ (Cut 3). Unblinded data (dots) are compared to background expectation from the simulation of the background components (stacked filled histograms). Expectations for the SM VH production with $m_H = 125$ GeV are multiplied by a factor 20 and presented as a non-stacked histogram (red line).

As shown in the last stage of the cutflow in table 5.9 an excess in data with respect to the expectations in the *Z-depleted* was observed. Due to the relevance of the excess further investigations are needed. In next section 5.9 the checks performed on this discrepancy between data and expectations are reported.

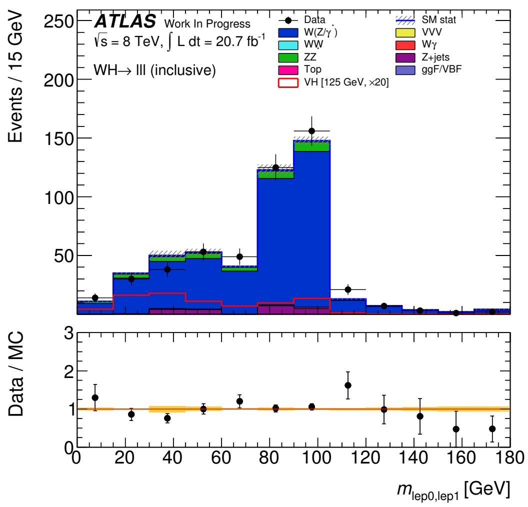

(a)

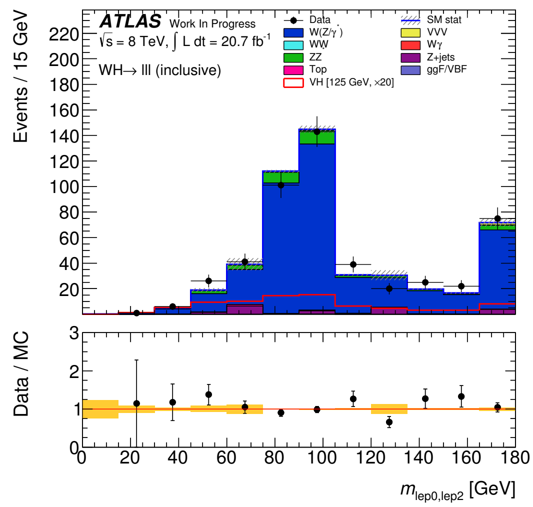

(b)

Figure 5.30: Distributions of the invariant masses of the two opposite sign lepton pairs in the *Z-enriched* samples after the cut on $E_{T,rel}^{Miss}$ (Cut 3): (a) the pair with smaller distance ΔR and (b) the one with larger ΔR. Unblinded data (dots) are compared to expectations from the simulation of the background components (stacked filled histograms). Expectations for the SM VH production with $m_H = 125$ GeV are multiplied by a factor 20 and presented as a non-stacked histogram (red line).

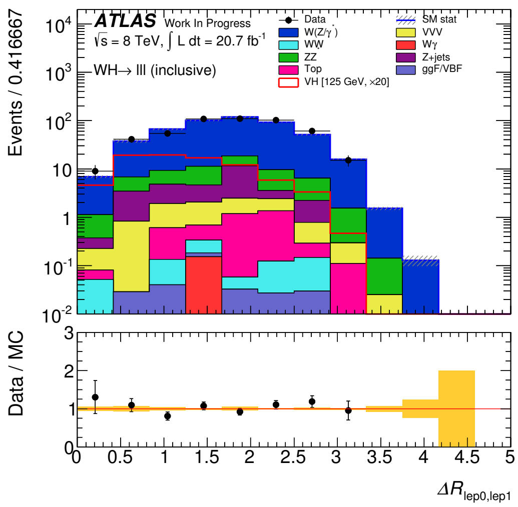

(a)

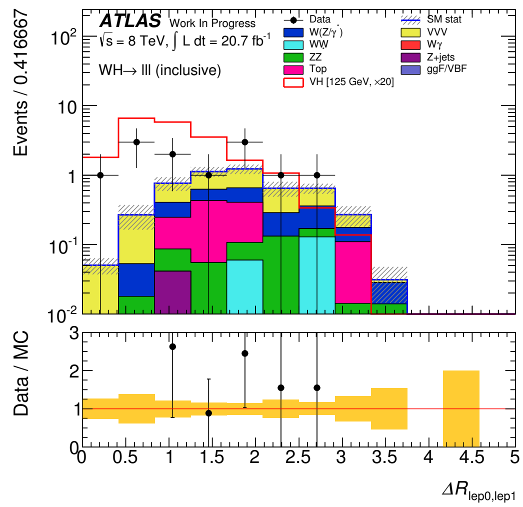

(b)

Figure 5.31: Distributions of $\Delta R(lep_0, lep_1)$ in the (a) *Z-enriched* and (b) *Z-depleted* sample after the cut on $E_{T,rel}^{Miss}$ (Cut 3). Unblinded data (dots) are compared to expectations from the simulation of the background components (stacked filled histograms). Expectations for the SM VH production with $m_H = 125$ GeV are multiplied by a factor 20 and is presented as a non-stacked histogram (red line).

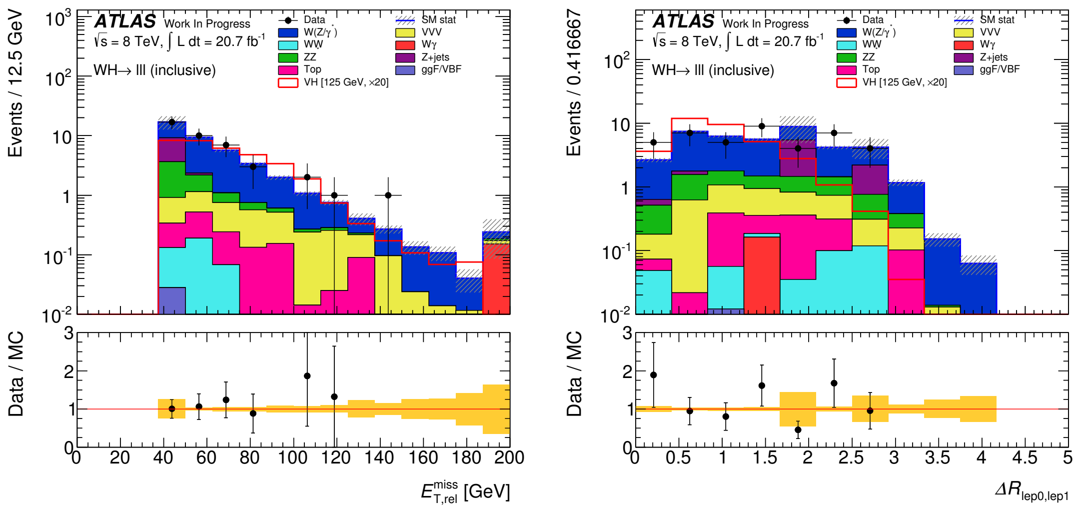

(a) (b)

Figure 5.32: Distributions of the $E_{T,rel}^{Miss}$ (a) and of the $\Delta R(lep_0, lep_1)$ (b) in the *Z-enriched* sample after vetoing oppositely signed lepton pairs with an invariant mass near to the Z peak (Cut 4). Unblinded data (dots) are compared to background expectation from the simulation of the background components (stacked filled histograms). Expectations for the SM VH production with $m_H = 125$ GeV are multiplied by a factor 20 and is presented as a non-stacked histogram (red line).

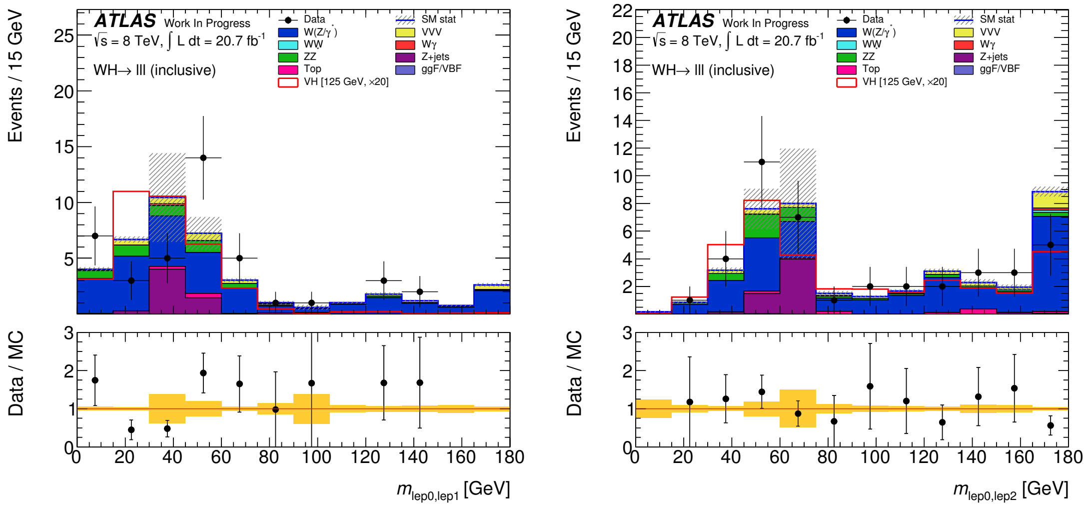

(a)

(b)

Figure 5.33: Distributions of the invariant masses of the two opposite sign lepton pairs in the *Z-enriched* samples after vetoing oppositely signed lepton pairs with an invariant mass near to the Z peak (Cut 4): (a) the pair with smaller distance ΔR and (b) the one with larger ΔR. Unblinded data (dots) are compared to expectations from the simulation of the background components (stacked filled histograms). Expectations for the SM VH production with $m_H = 125$ GeV are multiplied by a factor 20 and is presented as a non-stacked histogram (red line).

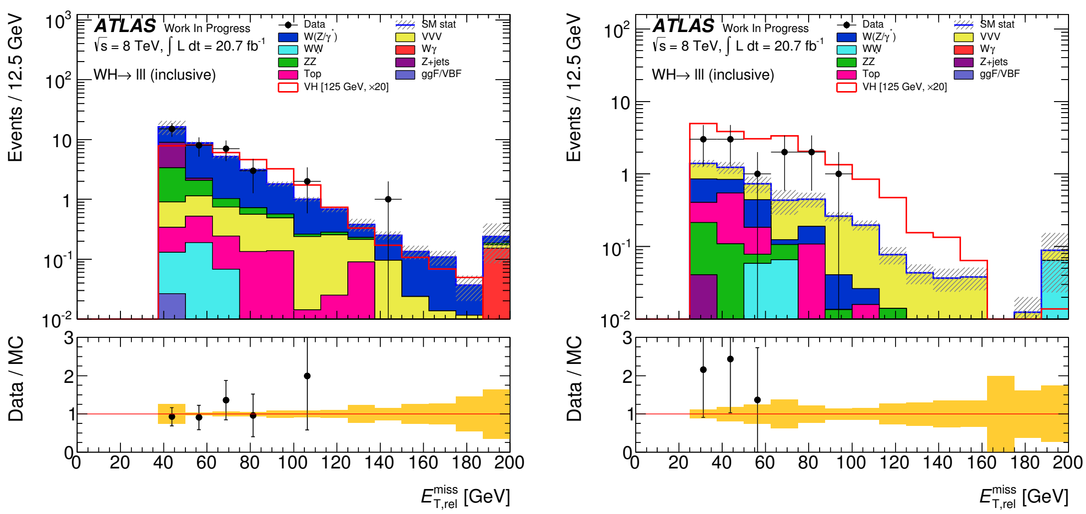

(a) (b)

Figure 5.34: Distributions of $E_{T,rel}^{Miss}$ in the (a) *Z-enriched* and (b) *Z-depleted* sample after the requirement on the smallest invariant mass of oppositely signed lepton pairs (Cut 5). Unblinded data (dots) are compared to background expectation from the simulation of the background components (stacked filled histograms). Expectations for the SM VH production with $m_H = 125$ GeV are multiplied by a factor 20 and is presented as a non-stacked histogram (red line).

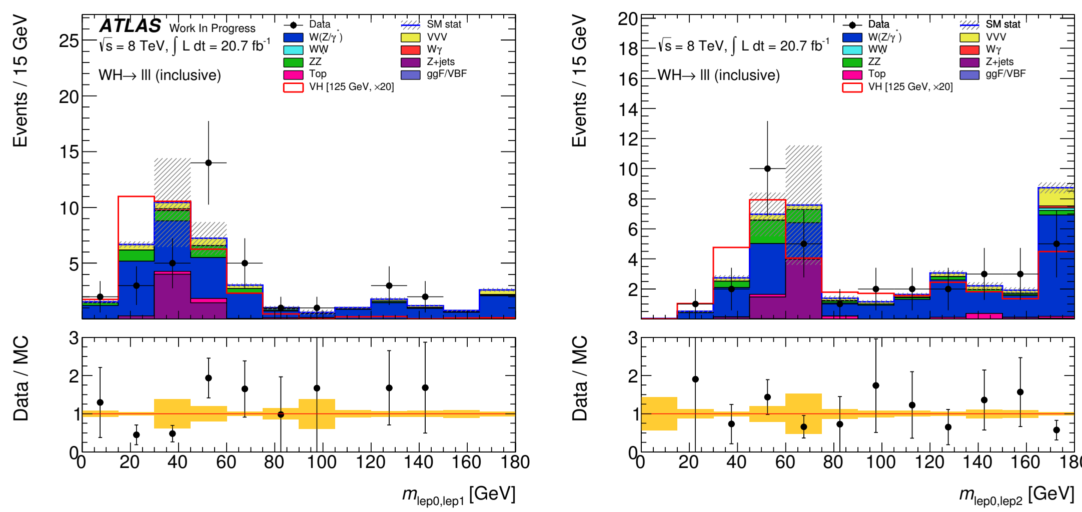

(a) (b)

Figure 5.35: Distributions of the invariant masses of the two opposite sign lepton pairs in the *Z-enriched* samples after the requirement on the smallest invariant mass of oppositely signed lepton pairs (Cut 5): (a) the pair with smaller distance ΔR and (b) the one with larger ΔR. Unblinded data (dots) are compared to expectations from the simulation of the background components (stacked filled histograms). Expectations for the SM VH production with $m_H = 125$ GeV are multiplied by a factor 20 and is presented as a non-stacked histogram (red line).

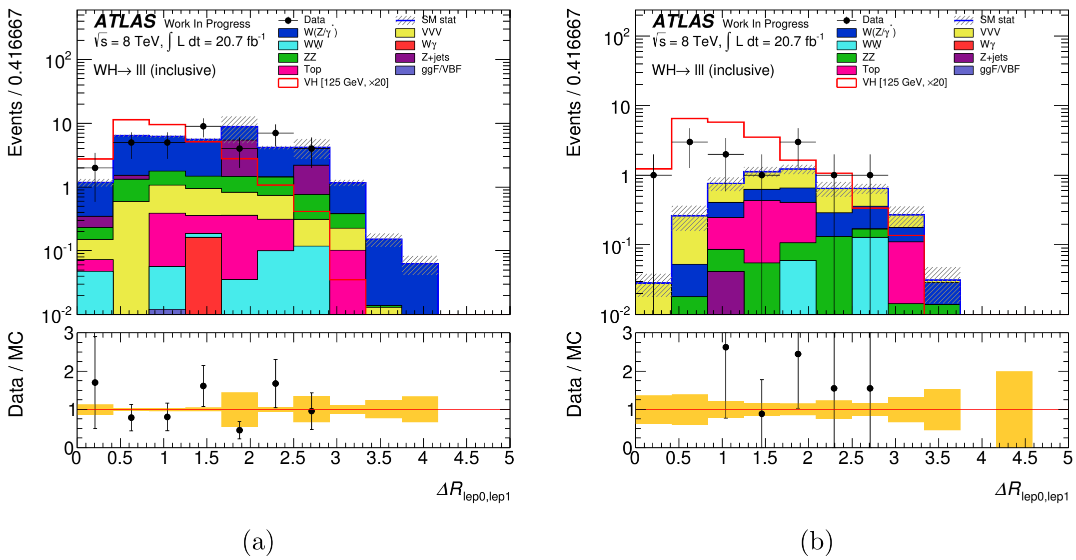

Figure 5.36: Distributions of $\Delta R(lep_0, lep_1)$ in the (a) *Z-enriched* and (b) *Z-depleted* sample after the requirement on the smallest invariant mass of oppositely signed lepton pairs (Cut 5). Unblinded data (dots) are compared to expectations from the simulation of the background components (stacked filled histograms). Expectations for the SM VH production with $m_H = 125$ GeV are multiplied by a factor 20 and is presented as a non-stacked histogram (red line).

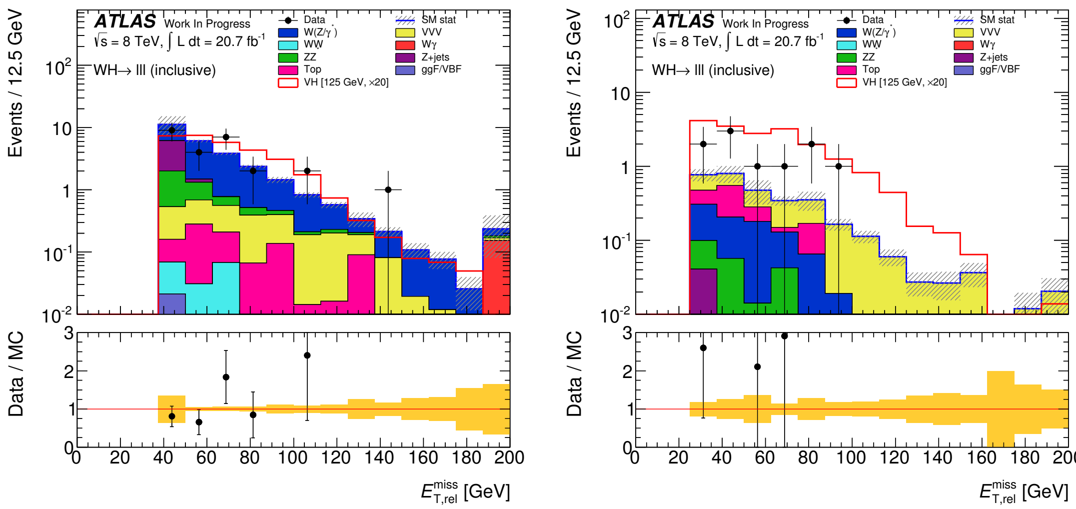

(a) (b)

Figure 5.37: Distributions of $E_{T,rel}^{Miss}$ in the (a) *Z-enriched* and (b) *Z-depleted* sample after the requirement on the smallest angular distance of oppositely signed lepton pairs (Cut 6). Unblinded data (dots) are compared to background expectation from the simulation of the background components (stacked filled histograms). Expectations for the SM VH production with $m_H = 125$ GeV are multiplied by a factor 20 and is presented as a non-stacked histogram (red line).

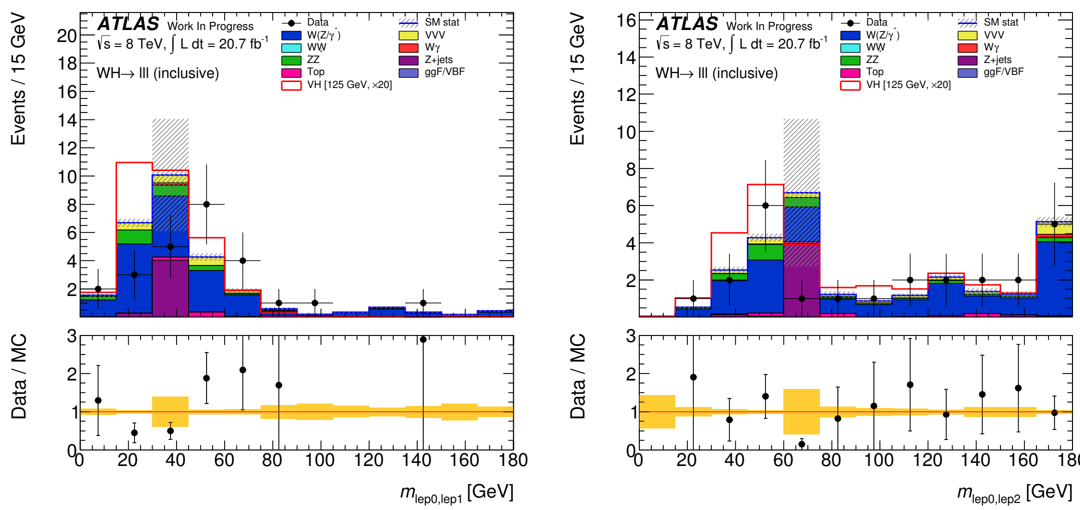

(a)

(b)

Figure 5.38: Distributions of the invariant masses of the two opposite sign lepton pairs in the *Z-enriched* samples after the requirement on the smallest angular distance of oppositely signed lepton pairs (Cut 6): (a) the pair with smaller distance ΔR and (b) the one with larger ΔR. Unblinded data (dots) are compared to expectations from the simulation of the background components (stacked filled histograms). Expectations for the SM VH production with $m_H = 125$ GeV are multiplied by a factor 20 and is presented as a non-stacked histogram (red line).

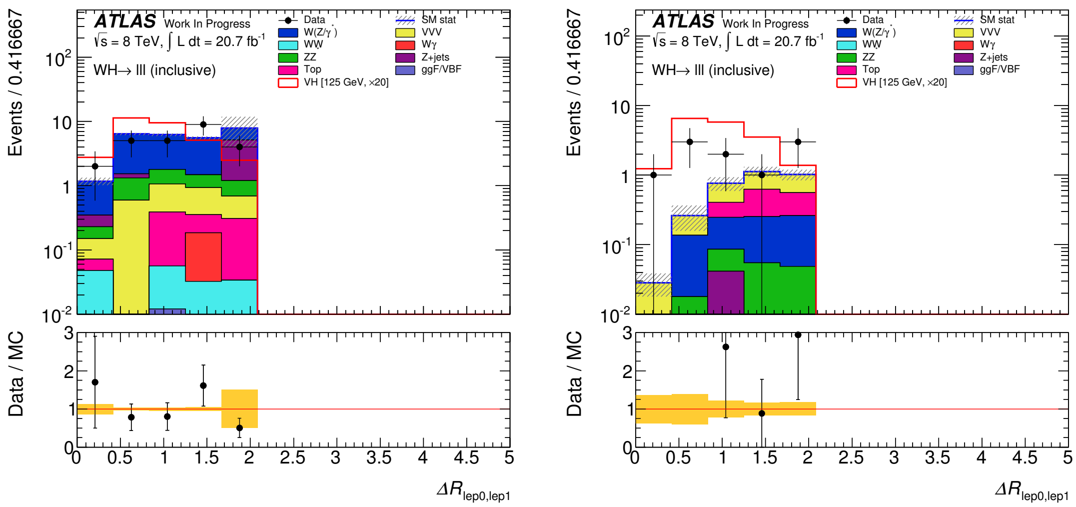

(a) (b)

Figure 5.39: Distributions of $\Delta R(lep_0, lep_1)$ in the (a) *Z-enriched* and (b) *Z-depleted* sample after the requirement on the smallest angular distance of oppositely signed lepton pairs (Cut 6). Unblinded data (dots) are compared to expectations from the simulation of the background components (stacked filled histograms). Expectations for the SM VH production with $m_H = 125$ GeV are multiplied by a factor 20 and is presented as a non-stacked histogram (red line).

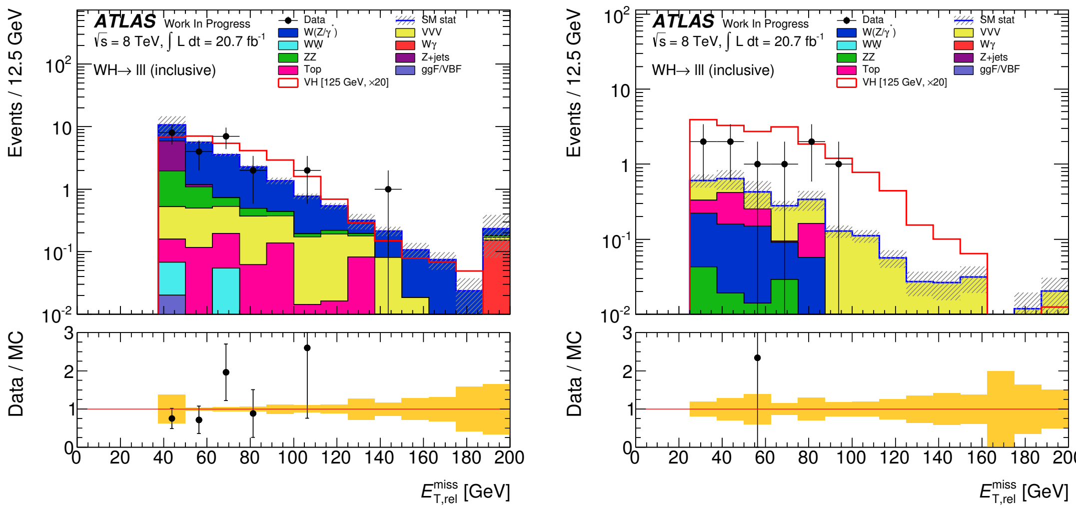

(a) (b)

Figure 5.40: Distributions of $E_{T,rel}^{Miss}$ in the (a) *Z-enriched* and (b) *Z-depleted* sample after the overlap removal with the 2-lepton analysis (Cut 7). Unblinded data (dots) are compared to background expectation from the simulation of the background components (stacked filled histograms). Expectations for the SM VH production with $m_H = 125$ GeV are multiplied by a factor 20 and is presented as a non-stacked histogram (red line).

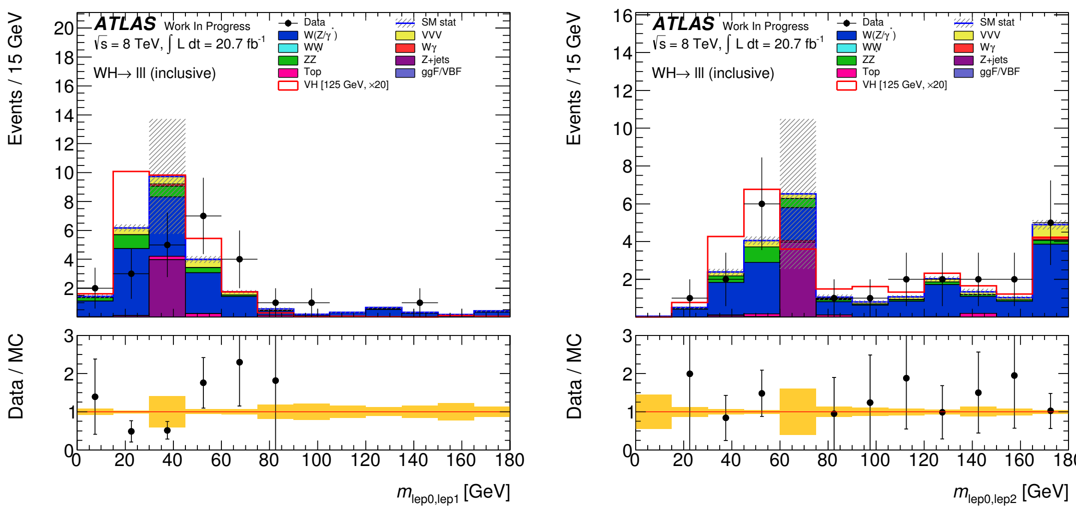

(a) (b)

Figure 5.41: Distributions of the invariant masses of the two opposite sign lepton pairs in the *Z-enriched* samples after the overlap removal with the 2-lepton analysis (Cut 7): (a) the pair with smaller distance ΔR and (b) the one with larger ΔR. Unblinded data (dots) are compared to expectations from the simulation of the background components (stacked filled histograms). Expectations for the SM VH production with m_H = 125 GeV are multiplied by a factor 20 and is presented as a non-stacked histogram (red line).

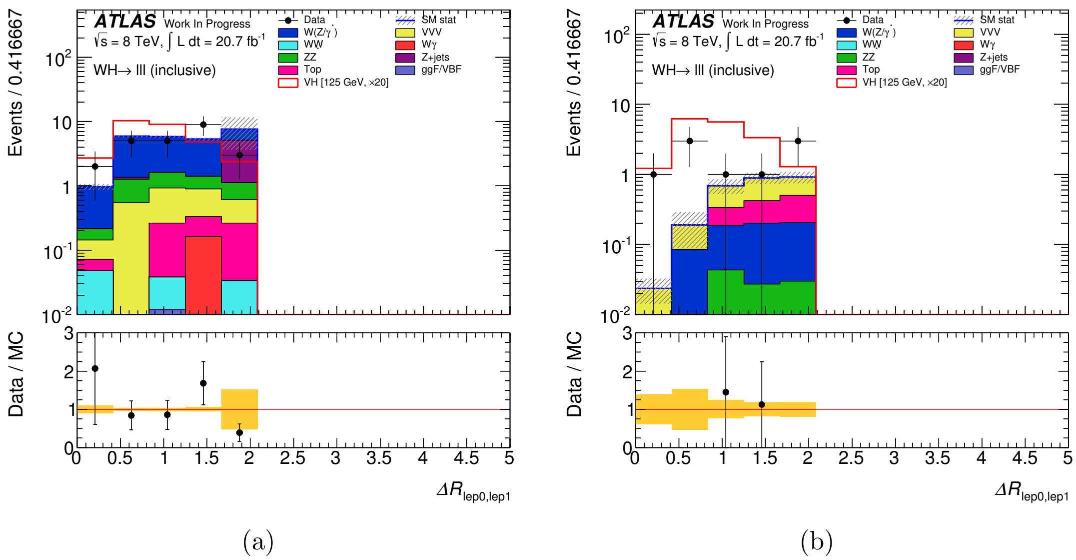

Figure 5.42: Distributions of $\Delta R(lep_0, lep_1)$ in the (a) *Z-enriched* and (b) *Z-depleted* sample after the overlap removal with the 2-lepton analysis (Cut 7). Unblinded data (dots) are compared to expectations from the simulation of the background components (stacked filled histograms). Expectations for the SM VH production with $m_H = 125$ GeV are multiplied by a factor 20 and is presented as a non-stacked histogram (red line).

	$W(H \to WW)$	$Z(H \to WW)$	$W(H \to \tau\tau)$	$Z(H \to \tau\tau)$	VH	Obs.	Total Bkg.
Pre-selection	6.10 ± 0.17	10.48 ± 0.33	1.10 ± 0.05	0.86 ± 0.03	18.53 ± 0.50	3717	3373.07 ± 153.79
Z enriched $(eee + \mu\mu\mu)$	1.55 ± 0.06	5.04 ± 0.18	0.32 ± 0.02	0.39 ± 0.02	7.31 ± 0.22	1711	1617.67 ± 54.15
num. jets < 2 $(eee + \mu\mu\mu)$	1.39 ± 0.06	3.35 ± 0.16	0.27 ± 0.02	0.33 ± 0.02	5.34 ± 0.21	1386	1409.06 ± 53.03
top veto $(eee + \mu\mu\mu)$	1.35 ± 0.06	2.96 ± 0.15	0.25 ± 0.02	0.30 ± 0.02	4.85 ± 0.21	1321	1345.52 ± 54.43
$E_{T,Rel}^{miss} > 40$ GeV $(eee + \mu\mu\mu)$	0.68 ± 0.04	0.90 ± 0.07	0.07 ± 0.01	0.08 ± 0.01	1.72 ± 0.09	252	255.50 ± 12.72
Z mass veto $(eee + \mu\mu\mu)$	0.41 ± 0.03	0.07 ± 0.02	0.02 ± 0.01	0.00 ± 0.00	0.50 ± 0.04	14	18.96 ± 5.65
$m_{ll} > 12$ GeV $(eee + \mu\mu\mu)$	0.39 ± 0.03	0.06 ± 0.02	0.02 ± 0.01	0.00 ± 0.00	0.48 ± 0.03	12	17.63 ± 5.58
$\Delta R_{ll} < 2.0$ $(eee + \mu\mu\mu)$	0.38 ± 0.03	0.05 ± 0.02	0.02 ± 0.01	0.00 ± 0.00	0.45 ± 0.03	9	14.06 ± 4.04
lvlv OR $(eee + \mu\mu\mu)$	0.36 ± 0.03	0.04 ± 0.01	0.02 ± 0.00	0.00 ± 0.00	0.42 ± 0.03	8	13.54 ± 4.03
Z enriched $(ee\mu + \mu\mu e)$	3.07 ± 0.10	5.21 ± 0.21	0.53 ± 0.03	0.43 ± 0.02	9.25 ± 0.29	1968	1725.48 ± 118.35
num. jets < 2 $(ee\mu + \mu\mu e)$	2.74 ± 0.12	3.49 ± 0.18	0.48 ± 0.03	0.36 ± 0.02	7.07 ± 0.30	1562	1507.25 ± 117.38
top veto $(ee\mu + \mu\mu e)$	2.66 ± 0.12	3.12 ± 0.17	0.46 ± 0.03	0.32 ± 0.02	6.56 ± 0.29	1490	1444.50 ± 118.24
$E_{T,Rel}^{miss} > 40$ GeV $(ee\mu + \mu\mu e)$	1.33 ± 0.07	0.88 ± 0.08	0.09 ± 0.01	0.08 ± 0.01	2.37 ± 0.13	247	234.78 ± 12.91
Z mass veto $(ee\mu + \mu\mu e)$	1.05 ± 0.05	0.11 ± 0.02	0.05 ± 0.01	0.01 ± 0.00	1.22 ± 0.06	27	21.42 ± 2.65
$m_{ll} > 12$ GeV $(ee\mu + \mu\mu e)$	1.00 ± 0.05	0.11 ± 0.02	0.05 ± 0.01	0.01 ± 0.00	1.17 ± 0.06	24	20.28 ± 2.61
$\Delta R_{ll} < 2.0$ $(ee\mu + \mu\mu e)$	0.97 ± 0.05	0.10 ± 0.02	0.04 ± 0.01	0.00 ± 0.00	1.11 ± 0.06	16	13.16 ± 0.87
lvlv OR $(ee\mu + \mu\mu e)$	0.91 ± 0.05	0.10 ± 0.02	0.03 ± 0.01	0.00 ± 0.00	1.04 ± 0.06	16	12.16 ± 0.82
Z depleted	1.48 ± 0.06	0.23 ± 0.03	0.25 ± 0.02	0.03 ± 0.00	1.98 ± 0.08	38	29.92 ± 4.34
num. jets < 2	1.33 ± 0.06	0.13 ± 0.02	0.23 ± 0.02	0.02 ± 0.00	1.71 ± 0.08	18	18.63 ± 4.23
top veto	1.29 ± 0.06	0.12 ± 0.02	0.22 ± 0.02	0.02 ± 0.00	1.66 ± 0.08	16	14.99 ± 4.11
$E_{T,Rel}^{miss} > 25$ GeV	0.88 ± 0.05	0.08 ± 0.02	0.09 ± 0.01	0.00 ± 0.00	1.05 ± 0.06	12	5.02 ± 0.67
$m_{ll} > 12$ GeV	0.85 ± 0.05	0.07 ± 0.02	0.09 ± 0.01	0.00 ± 0.00	1.01 ± 0.05	12	4.99 ± 0.67
$\Delta R_{ll} < 2.0$	0.80 ± 0.04	0.07 ± 0.02	0.06 ± 0.01	0.00 ± 0.00	0.92 ± 0.05	10	3.20 ± 0.47
lvlv OR	0.76 ± 0.04	0.07 ± 0.02	0.06 ± 0.01	0.00 ± 0.00	0.88 ± 0.05	9	2.71 ± 0.43

Table 5.9: Unblinded cutflow for the SM Higgs boson signal processes in three leptons final states. The number of observed events in data and expected events in the MC simulation is reported in the last two columns. The quoted uncertainties include both statistical and experimental systematic (described in section 5.10) uncertainties.

	VVV	$W(Z/\gamma^*)$	WW	ZZ^*	Z+jets	Top	$W\gamma$	$ggF \to ZZ$
Pre-selection	19.54 ± 0.50	1400.20 ± 27.29	1.65 ± 0.37	1011.51 ± 25.32	847.05 ± 102.52	82.27 ± 3.71	0.35 ± 0.22	10.16 ± 0.09
Z enriched ($eee + \mu\mu\mu$)	5.89 ± 0.18	719.72 ± 12.20	0.61 ± 0.19	507.09 ± 11.51	353.55 ± 36.62	25.36 ± 1.44	0.20 ± 0.16	5.17 ± 0.06
num. jets < 2 ($eee + \mu\mu\mu$)	5.11 ± 0.18	681.77 ± 12.62	0.43 ± 0.16	425.90 ± 11.55	286.26 ± 34.49	5.29 ± 0.94	0.20 ± 0.16	4.09 ± 0.06
top veto ($eee + \mu\mu\mu$)	4.79 ± 0.19	661.88 ± 15.11	0.43 ± 0.15	401.82 ± 11.69	270.59 ± 33.62	1.94 ± 0.65	0.20 ± 0.16	3.87 ± 0.05
$E_{T,Rel}^{miss} > 40$ GeV ($eee + \mu\mu\mu$)	2.51 ± 0.13	221.59 ± 5.72	0.25 ± 0.13	19.24 ± 1.83	11.02 ± 6.64	0.78 ± 0.51	0.00 ± 0.00	0.11 ± 0.01
Z mass veto ($eee + \mu\mu\mu$)	0.88 ± 0.07	11.14 ± 0.51	0.12 ± 0.08	2.29 ± 0.34	4.30 ± 5.10	0.22 ± 0.14	0.00 ± 0.00	0.02 ± 0.00
$m_{ll} > 12$ GeV ($eee + \mu\mu\mu$)	0.86 ± 0.07	10.11 ± 0.46	0.12 ± 0.08	2.00 ± 0.29	4.30 ± 5.10	0.22 ± 0.14	0.00 ± 0.00	0.02 ± 0.00
$\Delta R_{ll} < 2.0$ ($eee + \mu\mu\mu$)	0.64 ± 0.06	7.63 ± 0.37	0.00 ± 0.00	1.33 ± 0.20	4.28 ± 3.97	0.16 ± 0.13	0.00 ± 0.00	0.01 ± 0.00
lvlv OR ($eee + \mu\mu\mu$)	0.63 ± 0.06	7.42 ± 0.36	0.00 ± 0.00	1.28 ± 0.20	4.05 ± 3.97	0.15 ± 0.13	0.00 ± 0.00	0.01 ± 0.00
Z enriched ($ee\mu + \mu\mu e$)	9.54 ± 0.29	677.43 ± 15.31	0.60 ± 0.25	501.94 ± 13.95	487.80 ± 89.67	42.86 ± 2.58	0.15 ± 0.15	4.98 ± 0.06
num. jets < 2 ($ee\mu + \mu\mu e$)	8.52 ± 0.29	642.84 ± 15.26	0.46 ± 0.17	411.43 ± 13.99	428.42 ± 88.92	11.53 ± 1.79	0.15 ± 0.15	3.88 ± 0.05
top veto ($ee\mu + \mu\mu e$)	7.97 ± 0.29	624.03 ± 16.95	0.46 ± 0.17	383.85 ± 13.97	418.71 ± 88.47	5.66 ± 1.41	0.15 ± 0.15	3.65 ± 0.05
$E_{T,Rel}^{miss} > 40$ GeV ($ee\mu + \mu\mu e$)	4.24 ± 0.19	203.98 ± 6.44	0.28 ± 0.14	14.44 ± 1.36	8.98 ± 5.99	2.61 ± 1.03	0.15 ± 0.15	0.09 ± 0.01
Z mass veto ($ee\mu + \mu\mu e$)	2.37 ± 0.13	14.12 ± 0.65	0.23 ± 0.14	2.17 ± 0.27	1.44 ± 1.75	0.91 ± 0.39	0.15 ± 0.15	0.02 ± 0.00
$m_{ll} > 12$ GeV ($ee\mu + \mu\mu e$)	2.35 ± 0.13	13.20 ± 0.61	0.23 ± 0.14	1.99 ± 0.26	1.44 ± 1.75	0.90 ± 0.39	0.15 ± 0.15	0.02 ± 0.00
$\Delta R_{ll} < 2.0$ ($ee\mu + \mu\mu e$)	1.67 ± 0.11	9.28 ± 0.47	0.14 ± 0.10	1.26 ± 0.20	0.01 ± 0.01	0.64 ± 0.22	0.15 ± 0.15	0.02 ± 0.00
lvlv OR ($ee\mu + \mu\mu e$)	1.56 ± 0.11	8.61 ± 0.44	0.10 ± 0.10	1.21 ± 0.19	0.00 ± 0.00	0.50 ± 0.20	0.15 ± 0.15	0.01 ± 0.00
Z depleted	4.10 ± 0.16	3.05 ± 0.20	0.45 ± 0.18	2.48 ± 0.19	5.70 ± 4.03	14.04 ± 1.33	0.00 ± 0.00	0.01 ± 0.00
num. jets < 2	3.75 ± 0.16	2.83 ± 0.21	0.25 ± 0.15	1.94 ± 0.17	5.52 ± 4.04	4.32 ± 0.77	0.00 ± 0.00	0.01 ± 0.00
top veto	3.61 ± 0.16	2.77 ± 0.21	0.24 ± 0.14	1.78 ± 0.16	5.19 ± 3.96	1.39 ± 0.53	0.00 ± 0.00	0.01 ± 0.00
$E_{T,Rel}^{miss} > 25$ GeV	2.42 ± 0.12	1.26 ± 0.13	0.19 ± 0.14	0.37 ± 0.08	0.04 ± 0.04	0.74 ± 0.44	0.00 ± 0.00	0.00 ± 0.00
$m_{ll} > 12$ GeV	2.40 ± 0.12	1.25 ± 0.12	0.19 ± 0.14	0.37 ± 0.08	0.04 ± 0.04	0.74 ± 0.44	0.00 ± 0.00	0.00 ± 0.00
$\Delta R_{ll} < 2.0$	1.54 ± 0.09	0.69 ± 0.09	0.00 ± 0.00	0.17 ± 0.05	0.04 ± 0.04	0.75 ± 0.37	0.00 ± 0.00	0.00 ± 0.00
lvlv OR	1.45 ± 0.09	0.57 ± 0.08	0.00 ± 0.00	0.10 ± 0.03	0.00 ± 0.00	0.58 ± 0.35	0.00 ± 0.00	0.00 ± 0.00

Table 5.10: The unblinded cutflow for the Monte Carlo background samples in three leptons final states. Z+jets contains the Z boson production associated with heavy flavor jets. Top contains $t\bar{t}$ and single top productions as well as the $t\bar{t}$ productions associated with a W or Z boson. The scale factors are applied at the pre-selection. The quoted uncertainties include both statistical and experimental systematic (described in section 5.10) uncertainties.

5.9 Data Excess Checks

Due to the excess observed in the data compared with simulation expectations in the *Z-depleted* signal region, additional checks have been performed on the goodness of simulations and data. A first check has been made on the MC simulations. In particular, due to the possibility of testing several generators, a study on possible Top background underestimation has been performed. Checks on the charge flipping probability and on the data, in particular on the possible cosmic ray contamination, are also presented.

5.9.1 Top Monte Carlo Studies

A comparison of different $t\bar{t}$ MC has been performed using the following samples

- sample 1 : MC@NLO+Herwig with a software filter requiring 2 leptons (used as default in the present analysis)
- sample 2 : MC@NLO+Herwig with a software filter requesting at least one top decaying leptonically
- sample 3 : Powheg+Pythia6 with a software filter requesting at least one top decaying leptonically
- sample 4 : Alpgen+Herwig, with a software filter requiring both top quarks decaying leptonically

The expected yields are summarized in table 5.11 computed from the different MC samples. The differences are small and no hint of an underestimation has been found. The main problem of the *Z-depleted* signal region is the limited MC statistics. Since the applied selections do not depend on the lepton flavor a cutflow performed using all the possible lepton flavor combinations (including also the SFOS events) has been produced. To compare the new cutflow with the old one, the total number of expected events is normalized to the cutflow 5.11. The standard yields, including also the contributions from single top channels, are compared to those obtained with this method in table 5.12. No significant deviations are observed with the increased MC statistics.

	1	2	3	4
Z-depleted	21.53± 1.88	19.03± 3.47	22.40± 2.68	21.39± 2.88
num. jets < 2	8.25± 1.13	9.19± 2.20	8.45± 1.68	6.67± 1.53
b-veto	3.02± 0.69	4.87± 1.56	3.15± 1.02	3.25± 1.14
$E_{T,rel}^{Miss} > 25$ GeV	1.84± 0.55	3.81± 1.44	1.91± 0.78	3.14± 1.13
$m_{ll} > 12$ GeV	1.84± 0.55	3.81± 1.44	1.91± 0.78	3.14± 1.13
$\Delta R_{ll} < 2.0$	1.73± 0.51	1.54± 1.09	1.06± 0.59	1.38± 0.71
lvlv OR	0.73± 0.34	0.33± 0.87	0.09± 0.09	0.43± 0.43
top CR	8.53± 1.22	6.90± 2.24	6.34± 1.43	9.57± 1.98

Table 5.11: $t\bar{t}$ expected yields with different MC generators in the *Z-depleted* selection and Top Control Region.

	Top expectations	Top expectations with all flav. comb.
Z-depleted	28.27± 2.12	35.06± 1.11
num. jets < 2	10.70± 1.47	10.71± 0.77
b-veto	4.36± 0.98	4.46± 0.59
$E_{T,rel}^{Miss} > 25$ GeV	2.63± 0.75	2.86± 0.46
$m_{ll} > 12$ GeV	2.63± 0.75	2.86± 0.46
$\Delta R_{ll} < 2.0$	1.79± 0.51	1.61± 0.32
lvlv OR	0.77± 0.34	0.74± 0.16

Table 5.12: Top expected yields with standard selection and using all lepton flavor combinations.

5.9.2 Charge flipping study

In events with high p_T lepton it is possible to have a misidentification of the lepton charge. This effect can affect the result and should be considered as an additional source of background. Usually the charge misidentification, also called charge flipping probability, is neglected but due to the excess observed in the data a check on this possible source of discrepancy between data and MC simulations becomes interesting.

To perform this check the events with a total lepton charge of ± 3 were considered. Applying the selection presented in 5.4 to these events no events are observed already after Cut 3 hence the charge flipping probability, in this analysis, is negligible.

5.9.3 Check on Data

Since no important issue has been observed in the simulation, detailed checks have been performed on the data to explore two possible background sources, namely "cosmic ray events" and "fake electron reconstructed as real". Table 5.13 summarizes the run number, event number and flavor composition of the observed events.

	RunNumber (period)	EventNumber	Channel
A	201006 (E)	24034833	$\mu^+\mu^+e^-$
B	211787 (G)	108200777	$\mu^-\mu^-e^+$
C	212034 (G)	92913758	$e^-e^-\mu^+$
D	212742 (H)	99618848	$e^+e^+\mu^-$
E	213695 (I)	128775537	$\mu^-\mu^-e^+$
F	214160 (J)	74654301	$\mu^-\mu^-e^+$
G	215091 (J)	69412871	$\mu^-\mu^-e^+$
H	215091 (J)	77233045	$\mu^-\mu^-e^+$
I	208970 (D)	108827685	$\mu^+\mu^+e^-$

Table 5.13: Summary of observed events in the *Z-depleted* signal region

Cosmic ray events

A possible explanation of the excess observed is a cosmic ray muon overlapping with a single high-p_T lepton production. Such events have a well known topology:

- large $\Delta\phi$

- small $\Sigma\eta$
- Muons in different hemispheres (opposite sign η)

Due to this topology it is possible to select candidate cosmic ray events setting thresholds on $\Delta\phi > 2.0$ and $\Sigma\eta < 1.0$. None of the events listed in table 5.13 passed these simple selections hence it is possible to conclude that there are no candidates of cosmic ray events in the excess of the *Z-depleted* region.

Fake electron reconstructed as real

One possible hypothesis on the excess is the presence of fake electrons reconstructed as real. Such events might not be accurately simulated. To study this hypothesis, checks on the detector hits of electrons are performed. All the electron candidates present a high enough "High TRT ratio", which is the ratio of number of TRT hits which have a high transition radiation activity to the number of total TRT hits. Such information means that all the electron candidates appear to be electron like, hence also the hypothesis of the fake electron reconstructed as real electron could not explain the excess. After these checks no explanation other than a statistical fluctuation in data is found.

5.10 Systematics uncertainties

In this section a description of the systematic uncertainties affecting this analysis is reported. The systematic effects are divided in:

- Theory Systematics
- Experimental Systematics

5.10.1 Theory Systematics uncertainties

Theoretical uncertainties on the signal production cross sections are determined following the LHC Higgs cross section working group suggestions [12]. In the reference, the effects of a different choice for renormalization and factorization scales, PDFs and α_S are assessed. Scale variations by a factor 3 produce effects $\leq 1\%$ on WH production cross-section while the resulting uncertainty from PDF and α_s variations is $\leq 5\%$. An additional 3% uncertainty is assigned to account for the effect of the polarization of W bosons which radiate a Higgs boson in the $WH \rightarrow WWW^{(*)} \rightarrow l\nu l\nu l\nu$ process.

Systematic uncertainties coming from the parton distribution functions (PDFs) of colliding protons are assessed treating as independent the two contributions:

- The uncertainty between different PDF sets
- The uncertainty within a single PDF set

The former is estimated by comparing for two different PDF sets the event yield difference in each signal region while the latter is estimated by using PDF error sets. The PDF re-weighting technique is used in both contributions adopting the following procedure.

1. Calculate the event weight for a given default PDF set using Monte Carlo truth information
2. Calculate the event weight for another PDF set using Monte Carlo truth information
3. Take the ratio (weight) between the two

The PDF sets adopted in the generation of the samples are taken as default sets. To estimate the difference between two sets of PDF an alternative PDF set from a different family is chosen. Table 5.14 summarizes the PDF sets used in this assessment. In this estimate, backgrounds which are normalized to theory cross sections, namely VVV, WW and Wγ, are considered.

Sample	Default set	Alternative set	Error set
VVV	CTEQ6ll (LO)	MRSTMCal (LO)	CTEQ6l1 (LO)
WW	CT10 (NLO)	MSTW2008lo68cl (LO)	CT10 (NLO)
Wγ	CTEQ6ll (LO)	MRSTMCal (LO)	CTEQ6l1 (LO)

Table 5.14: Summary of PDF sets for the systematic uncertainty assessment.

Table 5.15 summarizes the results of the assessment in each signal region.

In addition the cross section uncertainty on the processes which are not normalized to data is treated as systematic error and included in the statistical treatment. Uncertainties on the normalization of 60% for the WW background and of 50% uncertainty on the k-factor of 1.5 for the VVV are assumed.

	VVV	WW	Wγ
Z-enriched SR (error set)	1.3%	4%	7.4%
(2 PDF diff)	0.9%	4%	7.9%
Z-depleted SR (error set)	1.2%	0%	0%
(2 PDF diff)	1.3%	0%	0%

Table 5.15: Summary of relative PDF uncertainties

5.10.2 Experimental Systematics uncertainties

The impact of the experimental systematics has been evaluated taking into account the effect of all the possible variations in the parameters entering the simulation. The experimental sources of systematic uncertainties are listed in table 5.16. These sources include momentum and energy scales, physics object reconstruction and identification efficiencies, the momentum and energy resolutions. The procedure adopted to compute all the systematics variations is:

- The systematic source of interest is varied by 1σ. When necessary, the resultant change in the object kinematics is propagated to the missing transverse momentum calculation. Nothing else in the analysis is changed.
- All the Monte Carlo samples are re-calibrated with this change and the analysis is repeated.
- The impact of the systematic source is evaluated as the difference in event yield between the nominal and the systematic ntuples.

Source of Uncertainty	Treatment in the analysis
Jet Energy Resolution (JER)	MC jet resolution smeared using jet p_T, η-dependent parametrization
Jet Energy Scale (JES)	In-situ JES: 2 components with significant impact
	η intercalibration
	High-p_T jets: applicable only to jets with $p_T > 800$ GeV
	Close-by jets
	Flavor composition, response
	b-JES: significant for $t\bar{t}$
	In-time pileup: depending on the process, jet p_T, η
	Out-of-time pileup:depending on the process, jet p_T, η
	Two additional pile-up components
Electron Selection Efficiency	Separate systematics for electron identification, reconstruction and isolation, added in quadrature
	Identification
	Reconstruction
	trigger
Electron Energy Scale	depending on η and E_T
Electron Energy Resolution	Energy varied within its uncertainty
Muon Momentum Scale, Resolution	Uncertainty smaller than 1%
b-tagging Efficiency	p_T dependent scale factor uncertainties
Missing Transverse Energy	Lepton and hard jet energy uncertainties propagated to MET
	Soft terms: $p_T \pm 1$ GeV uncertainty on energy scale; energy resolution uncertainty as a function of total p_T of hard objects and primary vertex multiplicity
Luminosity	3.6%

Table 5.16: Summary of experimental sources of systematic uncertainty.

Source of Uncertainty	Variation tag
Jet Energy Scale	NP_Modelling1JESUp, NP_Modelling1JESDown
	NP_Detector1JESUp, NP_Detector1JESDown
	HighPtJESUp, HighPtJESDown
	Eta_ModellingJESJESUp, Eta_ModellingJESJESDown
	Eta_StatMethodJESUp, Eta_StatMethodJESDown
	NPVJESUp, NPVJESDown
	MuJESUp, MuJESDown
	PilePtJESUp, PilePtJESDown
	PileRhoJESUp, PileRhoJESDown
	ClosebyJESUp, ClosebyJESDown
	FlavRespJESUp, FlavRespJESDown
	FlavCompJESUp, FlavCompJESDown
	bJESUp, bJESDown
Jet Energy Resolution	JERUp (one variation only)
Electron Energy Scale	ElecScaleUp, ElecScaleDown
Electron Energy Resolution	ElecResolutionUp, ElecResolutionDown
Muon Momentum Scale	MuonScaleUp, MuonScaleLow
Muon Momentum Resolution	MSUP, MSLOW, IDUP, IDLOW
	(the MS and the ID each contribute to muon momentum resolution)
Scale of soft terms in calorimeter E_T^{miss}	ScaleSoftTermsUp_ptHard ScaleSoftTermsDown_ptHard
Resolution of soft terms in calorimeter E_T^{miss}	ResoSoftTermsUp_ptHard, ResoSoftTermsDown_ptHard
	(longitudinal and transverse components treated as correlated)

Table 5.17: Summary of experimental sources of systematic uncertainty and associated variation tags, used to classify the results and combine the results with other analyses.

Z-enriched										
	VH [125GeV]	$W(Z/\gamma^{(*)})$	VVV	WW	$ZZ^{(*)}$	Z+jets	Top	$W\gamma$	other H (125)	Total Bkg
Nominal	1.46	16.03	2.19	0.10	2.49	4.05	0.65	0.15	0.03	25.70
ElecEnergy	± 0.01 (0.48%)	± 0.18 (1.14%)	± 0.02 (0.86%)	± 0.03 (33.98%)	± 0.04 (1.72%)	± 0.00 (0.00%)	± 0.07 (10.16%)	± 0.00 (1.03%)	± 0.00 (2.67%)	± 0.29 (1.12%)
MuonEnergy	± 0.00 (0.21%)	± 0.02 (0.15%)	± 0.01 (0.30%)	± 0.00 (0.00%)	± 0.02 (0.95%)	± 0.00 (0.00%)	± 0.00 (0.28%)	± 0.00 (0.00%)	± 0.00 (2.67%)	± 0.02 (0.07%)
JER	± 0.02 (1.57%)	± 0.19 (1.20%)	± 0.04 (1.63%)	± 0.05 (48.06%)	± 0.12 (4.65%)	± 0.00 (0.05%)	± 0.01 (1.97%)	± 0.00 (0.00%)	± 0.00 (3.79%)	± 0.38 (1.48%)
JES	± 0.02 (1.28%)	± 0.31 (1.92%)	± 0.05 (2.48%)	± 0.05 (52.63%)	± 0.11 (4.25%)	± 0.00 (0.00%)	± 0.02 (3.16%)	± 0.00 (0.00%)	± 0.02 (70.20%)	± 0.44 (1.70%)
METSoftTerm	± 0.01 (0.75%)	± 0.09 (0.54%)	± 0.02 (0.90%)	± 0.00 (0.00%)	± 0.17 (6.79%)	± 0.00 (0.00%)	± 0.00 (0.27%)	± 0.00 (0.00%)	± 0.00 (11.50%)	± 0.27 (1.05%)
LeptonEff	± 0.04 (2.42%)	± 0.35 (2.21%)	± 0.05 (2.42%)	± 0.00 (2.54%)	± 0.07 (2.71%)	± 0.16 (4.04%)	± 0.02 (3.04%)	± 0.00 (2.88%)	± 0.00 (2.31%)	± 0.66 (2.58%)
FlavorTag	± 0.00 (0.29%)	± 0.04 (0.26%)	± 0.01 (0.33%)	± 0.00 (0.38%)	± 0.01 (0.30%)	± 0.00 (0.03%)	± 0.01 (1.83%)	± 0.00 (0.00%)	± 0.00 (0.65%)	± 0.06 (0.23%)
Total	± 0.05 (3.31%)	± 0.55 (3.43%)	± 0.09 (4.06%)	± 0.08 (79.00%)	± 0.25 (9.86%)	± 0.16 (4.04%)	± 0.07 (11.40%)	± 0.00 (3.06%)	± 0.02 (71.38%)	± 0.97 (3.77%)

Table 5.18: Summary of the experimental systematic uncertainties in the *Z-enriched* signal region.

Z-depleted							
	VH [125GeV]	$W(Z/\gamma^{(*)})$	VVV	$ZZ^{(*)}$	Top	other H (125)	Total Bkg
Nominal	0.88	0.57	1.45	0.10	0.58	0.00	2.71
ElecEnergy	± 0.01 (1.00%)	± 0.01 (1.93%)	± 0.01 (1.00%)	± 0.01 (6.75%)	± 0.00 (0.02%)	± 0.00 (8.41%)	± 0.03 (1.00%)
MuonEnergy	± 0.00 (0.08%)	± 0.01 (1.29%)	± 0.01 (0.49%)	± 0.00 (0.00%)	± 0.00 (0.00%)	± 0.00 (0.00%)	± 0.01 (0.42%)
JER	± 0.01 (0.86%)	± 0.01 (2.24%)	± 0.01 (0.81%)	± 0.00 (3.01%)	± 0.13 (22.75%)	± 0.00 (1.92%)	± 0.06 (2.22%)
JES	± 0.01 (1.56%)	± 0.03 (4.40%)	± 0.03 (1.72%)	± 0.00 (1.99%)	± 0.16 (26.97%)	± 0.00 (60.71%)	± 0.17 (6.44%)
METSoftTerm	± 0.01 (0.75%)	± 0.01 (1.19%)	± 0.00 (0.04%)	± 0.01 (8.53%)	± 0.00 (0.00%)	± 0.00 (0.00%)	± 0.01 (0.21%)
LeptonEff	± 0.02 (2.64%)	± 0.01 (2.39%)	± 0.03 (2.33%)	± 0.00 (2.94%)	± 0.02 (3.57%)	± 0.00 (1.43%)	± 0.07 (2.63%)
FlavorTag	± 0.00 (0.33%)	± 0.00 (0.20%)	± 0.01 (0.34%)	± 0.00 (1.02%)	± 0.01 (1.26%)	± 0.00 (1.10%)	± 0.01 (0.43%)
Total	± 0.03 (3.45%)	± 0.03 (6.08%)	± 0.05 (3.23%)	± 0.01 (11.90%)	± 0.21 (35.49%)	± 0.00 (61.35%)	± 0.20 (7.40%)

Table 5.19: Summary of the experimental systematic uncertainties in the *Z-depleted* signal region. The uncertainties on WW, Z+jets and $W\gamma$ backgrounds are negligible and not reported.

Chapter 6

Statistical Interpretation

In this chapter an introduction to the statistical tests commonly used in high energy physics experiments is presented. In section 6.8 statistical interpretations of the results obtained in the analysis presented in chapter 5 are reported. The results are also combined with those of the other production modes for the decay in the $H \to WW^{(*)} \to l\nu l\nu$ channel.

6.1 Formalism

Before going into the details of the statistical tests used in the high energy physics experiments is useful to introduce the formalism used in statistical analysis. In general an analysis is based on observables (here and furthermore defined with "x"). Several measurements of the same observable give an ensemble defined as the probability density function (pdf) of the observable itself. The pdf, often written as $f(x)$, has an important property:

$$\int f(x)dx = 1 \tag{6.1}$$

it is normalized to unity. In experiments an observable usually depends on several parameters, as for example the energy resolution of a calorimeter. The parametric family of pdfs has the form:

$$f(x \mid \alpha) \tag{6.2}$$

where α is the parameter (or the set of parameters) on which the observable depends. The equation 6.2 is often called probability model or just model. The model parameters can represent unknown properties of the detector's response or parameters of a theory. Usually the model parameters are divided in two category:

- parameters of interest
- nuisance parameters

The parameter the analysis is interested in is called "parameter of interest". In the Higgs boson search one of the possible parameters of interest is μ defined as the ratio between the measured cross section and the expected Standard Model Higgs boson cross section. The pdf described above is the probability density function of x for a single event. In experiments where several events are acquired and analyzed, the pdf definition is generalized to a dataset with N events ($E = \{x_1, ..., x_N\}$). If the events are independent the pdf for the E is just the product of the probability densities for each event. In high energy physics experiments predictions of the number of expected events are always computed. If the number of expected events ("e") is known, using a Poisson function it is possible to compute the probability of observing N events given e expected.

Considering together the Poisson probability and the product of the probability densities for each event it is possible to obtain the marked Poisson model for a given dataset.

$$f(E \mid e, \alpha) = P_s(N \mid e) \prod_{a=1}^{N} f(x_a \mid \alpha) \tag{6.3}$$

6.1.1 Example of marked Poisson model

In this section one simple case of marked Poisson model [86] is constructed. In this case the expected signal and background events are respectively S and B. If N events are observed it is possible to construct a marked Poisson probability similar to the one showed in 6.3. To simplify the analysis only one model parameter will be considered, the parameter of interest (POI). The POI will be defined as the "signal strength" μ. This value normalizes the signal such that $\mu = 0$ describes a background-only scenario while $\mu = 1$ describes a signal plus background scenario. Looking only at the expectation it is possible to write $e = \mu S + B$. The probability to observe N with $\mu S + B$ expected events is a Poisson one of the form $P_s(N \mid \mu S + B)$. In this case, since we have no α parameters, the second part of equation 6.3 is not present. The marked Poisson model now should take into account several possibilities to obtain the observable value x_a from a mixture of the pdfs of signal ($f_S(x)$) and background ($f_B(x)$). The final marked Poisson model will have the form

$$P(E \mid \mu) = P_s(N \mid \mu S + B) \times \prod_{a=1}^{N} \frac{\mu S f_S(x_a) + B f_B(x_a)}{\mu S + B} \tag{6.4}$$

6.2 Likelihood function

Starting from the marked Poisson model it is useful to study the equation 6.3, as function of the parameters α, with the data fixed. This kind of equation, called likelihood function ($L(\alpha)$), is the heart of any statistical analysis. One important clarification about the likelihood function is that it is not the pdf of α. The $L(\alpha)$ has not the same property of the pdf and in particular it is not normalized to unity. The difference between the pdf $f(x)$ and the Likelihood function $L(\alpha)$ is that [87]:

- $f(x)$ is the value of f as a function of x given a fixed value of α.
- $L(\alpha)$ is the value of f as a function of α given a fixed value of x.

It is common to work with a log-likelihood (or negative log-likelihood) function.

6.2.1 Example of Likelihood function

As in the case of the marked Poisson model is useful to present an example of a Likelihood function construction. The model presented here is based on a “cut and count” experiment, an experiment in which distribution of the observable is not used but only the number of events is considered in the statistical analysis. This is the case of the statistical analysis performed in the 3-lepton analysis. As in the marked Poisson example, consider an experiment with S signal and B background expected events. In this case B and S will be taken as constants so it is not necessary to add the second part of the 6.4. If the observed number of events it is N the Likelihood function has the same form of a Poisson distribution:

$$L(\mu) = P_s(N \mid \mu S + B) \tag{6.5}$$

where μ is the POI. Often in the analysis the number of background events is not taken directly from the MC expectations. Usually Control Regions, as in the case of the analysis described in this thesis, are constructed to normalize the background. Hence become interesting to add in the 6.5 new parameters, called nuisance parameters (NP), taking into account the normalization factor computed via CR. In this simple case only one normalization factor τ will be introduced but a generalization to several normalization factors is straightforward. If in the CR there are N_{CR} observed and B_{CR} expected events the likelihood function will have the form

$$L(\mu, \tau) = P_s(N \mid \mu S + \tau B) P_s(N_{CR} \mid \tau B_{CR}) \tag{6.6}$$

In literature the second Poisson function is called “auxiliary constraint” because it helps in constraining τ while N_{CR} is called “auxiliary measurement”. A general form of the likelihood function taking into account several NP can be written:

$$L(\mu, \alpha) = L(N \mid \mu, \alpha) \times A(\widetilde{\theta} \mid \theta) \tag{6.7}$$

where $A(\widetilde{\theta} \mid \theta)$ is an auxiliary likelihood that represents the measurements of the auxiliary parameters.

6.3 Analysis using Likelihood function

The final task for all the statistical analysis is to estimate some parameter of a certain model. To do it, it is necessary to define a function of the data useful to estimate the true value of a parameter. This function is called “estimator”. The estimator used more often in the high energy physics experiments is the maximum likelihood estimator (MLE). The MLE is defined as the value of α which maximizes the likelihood function. Sometimes instead of the likelihood function, the log-likelihood is used, but the definition of MLE remains the same. As described in the previous section the likelihood function could be function of more than one parameter α. The estimator related to the likelihood could be divided in two categories:

- Unconditional maximum likelihood estimator
- Conditional maximum likelihood estimator

The estimator is defined “Unconditional” if all the parameters α are free to float in the fit procedure that maximizes the likelihood. If at least one parameter of the list is fixed the estimator is defined as “Conditional”. Considering the case described in 6.6 it is possible to have a likelihood that is function of the “signal strength” and of a nuisance parameter. The MLE of τ will be a function of μ, defined as $\widehat{\tau}$. The likelihood obtained for $\widehat{\tau}$, $L(\mu, \widehat{\tau})$ is called profiled likelihood. To estimate the true value of μ it is possible to use the likelihood function. In particular to estimate it, the value that maximizes the unconditional likelihood ($\widehat{\mu}$) is used. For a simple case as the one described above it is possible to compute analytically the values of $\widehat{\tau}$ and $\widehat{\mu}$. In particular it is easy to demonstrate that

$$\widehat{\tau} = \frac{N_{CR}}{B_{CR}} \tag{6.8}$$

$$\widehat{\mu} = \frac{N - N_{CR}\frac{B}{B_{CR}}}{S} \tag{6.9}$$

For an unconditional estimator the value of the nuisance parameter $\widehat{\widehat{\tau}}$ could be different from $\widehat{\tau}$. This is true because μ can be different from $\widehat{\mu}$.

6.4 Hypothesis test

In general the task of a statistical analysis is to determine which of two hypotheses is in better agreement with the observation and to quantify this agreement. A typical case is the background-only hypothesis (called H_0) against the signal plus background hypothesis (called H_1 or alternate hypothesis).

In case of a "cut and count" scenario with no nuisance parameter, it is easy to define the probability model for both H_0 and H_1. If the number of observed events in a signal region is N_{SR} while the number of expected events for signal and background are respectively N_S and N_B is possible to define the probability models of the two hypotheses as $P_s(N_{SR} \mid N_B)$ for H_0 and $P_s(N_{SR} \mid N_B + N_S)$ for H_1. The problem, once defined the probability models of the different hypotheses, is to choose which is the best test statistics to adopt. The test statistics, in general, is defined as the function that maps the dataset analyzed to a single real number. Different test statistics can give different results but all the tests are characterized by two properties: the size and the power. The size of the test (α) is the probability to reject the hypothesis when it is true while the power of the test is related to the probability to accept the hypothesis when the alternate hypothesis is true. In high energy physics experiments a framework provided by Neyman and Pearson is used to choose the best test statistic. This framework in based on the definition of an acceptance region. Assume to search for a test statistic to test the null hypothesis. The first step is to define an acceptance region in terms of test statistic such that for $T(E) < k_\alpha$ (where E is the dataset and T(E) the test statistic) the null hypothesis is accepted. The size of the test will be

$$\alpha = P(T(E) \geq k_\alpha \mid H_0) \tag{6.10}$$

while the probability to accept the null hypothesis when the alternate is true will be

$$\beta = P(T(E) \leq k_\alpha \mid H_1) \tag{6.11}$$

the power of the test will be $1-\beta$.

The best test statistics is the one that maximizes the power of the test for a fixed test size. It is possible to demonstrate that in case of two simple hypotheses the test statistic leading to the most powerful test is given by the likelihood ratio $T(E \mid H_1)/T(E \mid H_0)$. This explains why the test statistics discussed in the next section have all the form of a likelihood ratio.

6.5 Test Statistic

In high energy physics experiments there are several examples of likelihood ratios used for statistical tests. The most common is the Profile Likelihood Ratio (PLR) $\lambda(\mu)$

$$\lambda(\mu) = \frac{L(\mu, \widehat{\theta}_\mu)}{L(\widehat{\mu}, \widehat{\theta})} \tag{6.12}$$

Often is useful to put physical constraints to the POI. For example in a model without interference between signal and background processes the data observed are expected to be equal or larger than the number of background events. This can be translated in term of signal strength requiring $\widehat{\mu} > 0$. In this case another type of likelihood ratio is used: the alternate PLR $\widehat{\lambda}(\mu)$.

$$\widehat{\lambda}(\mu) = \begin{cases} \frac{L(\mu,\widehat{\theta}_\mu)}{L(\widehat{\mu},\widehat{\theta})} & \text{for } \widehat{\mu} \geq 0 \\ \frac{L(\mu,\widehat{\theta}_\mu)}{L(0,\widehat{\theta}_0)} & \text{for } \widehat{\mu} < 0 \end{cases} \tag{6.13}$$

If it is necessary to compare two different hypotheses the Ratio of Profiled Likelihoods (RPL) λ_{RPL} is used instead. This likelihood ratio can be written in the form

$$\lambda_{RPL} = \frac{L(1, \widehat{\theta}_1)}{L(0, \widehat{\theta}_0)}. \tag{6.14}$$

It is possible to demonstrate that the RPL corresponds to the ratio between the PLRs of the two hypotheses.

$$\frac{L(1,\widehat{\theta}_1)}{L(0,\widehat{\theta}_0)} = \frac{\lambda(1)}{\lambda(0)} \tag{6.15}$$

6.5.1 Test Statistic t_μ

The test statistic t_μ is constructed starting from the $\lambda(\mu)$ and has the form

$$t_\mu = -2ln\lambda(\mu) \tag{6.16}$$

Looking at the $\lambda(\mu)$ definition, it is possible to observe that $0 \leq \lambda(\mu) \leq 1$. In particular for $\lambda(\mu)$ values near to the unity there is good agreement between the data and the hypothesized value of μ. This observation can be translated in terms of test statistic t_μ: higher values of t_μ correspond to an increase in incompatibility between the data and the hypothesis. To quantify the level of disagreement between data and hypothesis the so called p-value is computed.

$$p_\mu = \int_{t_{\mu,obs}}^{\infty} f(t_\mu \mid \mu) dt_\mu \tag{6.17}$$

where $f(t_\mu \mid \mu)$ is the pdf of the test statistic under the assumption of the signal strength μ and $t_{\mu,obs}$ is the value of the t_μ observed from the data. As in the case of $\lambda(\mu)$ also the test statistic t_μ changes form if there are constraints on the value of μ. Since the signal process have μ >0, $\widehat{\mu}$ is expected to be larger than zero. The modified test statistic t_μ is $\widetilde{t}_\mu$, it has the form

$$\widetilde{t}_\mu = \begin{cases} -2ln\frac{L(\mu,\widehat{\theta}_\mu)}{L(\widehat{\mu},\widehat{\theta})} & \text{for } \widehat{\mu} \geq 0 \\ -2ln\frac{L(\mu,\widehat{\theta}_\mu)}{L(0,\widehat{\theta}_0)} & \text{for } \widehat{\mu} < 0 \end{cases} \tag{6.18}$$

Starting from this test statistic it is possible to evaluate the incompatibility between data and hypothesized value of μ using the p-value defined in 6.17.

6.5.2 Test Statistic for discovery: q_0

In general the claim for new signal is related to the rejection of background-only hypothesis. In this scenario an important special case of the test statistic t_μ is when the null hypothesis ($\mu = 0$) is tested. For this test the $q_0 = \widetilde{t}_\mu$ is used. q_0 as the form:

$$q_0 = \begin{cases} -2ln\lambda(0) & \text{for } \widehat{\mu} \geq 0 \\ 0 & \text{for } \widehat{\mu} < 0 \end{cases} \tag{6.19}$$

The test statistic q_0 is chosen to be zero for $\widehat{\mu}$ <0 because otherwise a downward fluctuation of data, not related to the presence of any signal, would increase the incompatibility with a background-only hypothesis. With this definition only the presence of signal (or upward fluctuation of data) is considered for the incompatibility between data and the μ =0 hypothesis. If $f(q_0 \mid 0)$ is the pdf of the test statistic under assumption of the background-only hypothesis it is possible to compute a p-value as in the case of t_μ. The p_0-value can be computed using the formula

$$p_0 = \int_{q_{0,obs}}^{\infty} f(q_0 \mid 0) dq_0 \tag{6.20}$$

6.5.3 Test Statistic to establish upper limits: q_μ

To establish upper limits on the parameter μ a test statistic related to t_μ is used. This test, called q_μ, has the form

$$q_\mu = \begin{cases} -2ln\lambda(\mu) & \text{for } \widehat{\mu} \leq \mu \\ 0 & \text{for } \widehat{\mu} > \mu \end{cases} \tag{6.21}$$

The test statistic is set to 0 for $\widehat{\mu} > \mu$ because when looking at upper limits it is not correct to consider data with $\widehat{\mu} > \mu$ as representing less compatibility with μ than the data observed. For this reason the region $\widehat{\mu} > \mu$ is no taken into account in the rejection region of the test. This property of q_μ is similar to the one described for q_0 but it is necessary to point out that q_0 is not a special case of q_μ with μ =0. The definitions and purposes of the two tests are different. In particular q_0 is zero for a downward fluctuation of data while q_μ is zero if data fluctuates upward. Also in the q_μ case it is interesting to look at the level of agreement between data and the hypothesis using the p-value. For this test the p-value has the form

$$p_\mu = \int_{q_{\mu,obs}}^{\infty} f(q_\mu \mid \mu) dq_\mu \tag{6.22}$$

where the $f(q_\mu \mid \mu)$ is the test statistic pdf for the hypothesized μ. In case of constraints on the signal strength a different test statistic is used, $\widetilde{q}_\mu$. This test statistic is based on the alternate PLR $\widetilde{\lambda}(\mu)$ and has the form

$$\widetilde{q}_\mu = \begin{cases} -2ln\frac{L(\mu,\widehat{\theta}_\mu)}{L(0,\widehat{\theta}_0)} & \text{for } \widehat{\mu} < 0 \\ -2ln\frac{L(\mu,\widehat{\theta}_\mu)}{L(\widehat{\mu},\widehat{\theta})} & \\ 0 & \text{for } \widehat{\mu} > \mu \end{cases} \tag{6.23}$$

6.6 p_0 and confidence level calculation

In general a test statistic is a function that maps the data to a single real-valued number. For the observed data the test statistic has a given value, for example $\widetilde{q}_{\mu,obs}$. If a measurement is repeated several times the test statistic would take different values hence it can be treated as a distribution. In the previous section this distribution was introduced without considering the nuisance parameters but it is useful to remind that experimental measurement always depend on some systematic uncertainties. The systematics uncertainties can be introduced as nuisance parameters and can affect the test statistic pdf. In general a test statistic pdf has the form:

$$f(\widetilde{q}_\mu \mid \mu, \theta) \tag{6.24}$$

and the related p-value for a particular hypothesis (μ, θ) will be

$$p_{\mu,\theta} = \int_{\widetilde{q}_{\mu,obs}}^{\infty} f(\widetilde{q}_\mu \mid \mu, \theta) d\widetilde{q}_\mu \tag{6.25}$$

It is possible to demonstrate that for large sample size (asymptotically) the profiled likelihood ratio is independent of the values of the nuisance parameters. Hence the p-value could be written in the form

$$p_\mu = \int_{\widetilde{q}_{\mu,obs}}^{\infty} f(\widetilde{q}_\mu \mid \mu, \widetilde{\theta}(\mu, obs)) d\widetilde{q}_\mu \tag{6.26}$$

where $\widetilde{\theta}(\mu, obs)$ is the specific value of θ that produces the supremum p-value over all the possible θ. In case of discovery is interesting to study the compatibility of the data with the background-only hypothesis. Statistically rejecting the null hypothesis corresponds to the discovery of new signal. This compatibility is computed using the p_0-value

$$p_0 = \int_{\widetilde{q}_{0,obs}}^{\infty} f(\widetilde{q}_0 \mid 0, \widetilde{\theta}(0, obs)) d\widetilde{q}_0 \tag{6.27}$$

Usually the value obtained from the p_0-value is converted into the quantile of a unit Gaussian. This conversion does not depend on the test static used and is defined as:

$$Z = \Phi^{-1}(1 - p_0) \tag{6.28}$$

where Φ^{-1} is the inverse of the cumulative distribution.

Another result often showed as statistical result is the confidence level interval. To describe this method is useful to go back to the example introduced above, an experiment with N observed events, S signal and B background expected events. To have a more clear notation no nuisance parameters are taking into account here but a generalization introducing these parameters is not difficult. Let's introduce the p-value for the signal plus background hypothesis, called here p_{s+b}

$$p_{s+b} = \int_{q_{obs}}^{\infty} f(q \mid s + b)dq \tag{6.29}$$

and a different definition of p-value for the background-only hypothesis p_b

$$p_b = \int_{-\infty}^{q_{obs}} f(q \mid b)dq \tag{6.30}$$

There are two methods to calculate the confidence level (CL).

The first one, called "CL_{s+b}", is based on the p_{s+b} information. In particular the signal is regarded as excluded at a confidence level 1 - α if

$$p_{s+b} < \alpha. \tag{6.31}$$

In the ATLAS experiment results $\alpha = 0.05$. The CL_{s+b} method is affected by a problem. If the pdfs of test statistic for background-only and signal plus background are really similar, hence there is no sensitivity to exclude the model, the CL_{s+b} method will exclude the hypothesis. For example if $s << b$ the value of s will be excluded also if the test has not real sensitivity to do it.

To solve this problem a different CL method is introduced, the "CL_s" method. This procedure is based on both p_{s+b} and p_b and it is defined as

$$CL_s = \frac{p_{s+b}}{1 - p_b} < \alpha \tag{6.32}$$

In this method the p-value obtained for the signal plus background hypothesis is divided by a factor $1 - p_b$. If the two pdf distributions are well separated the $1 - p_b$ is slightly less than unity and the exclusion limit is similar to the one obtained with p_{s+b}.

Otherwise if one has little sensitivity to the signal model the two pdf distributions are close together and the $1 - p_b$ becomes small hence the CL_s increases and the problem of excluding model to which the test statistic has not enough sensitivity is solved.

6.7 Asymptotic approximation and Toy MC

Looking at the tests presented in the previous sections one important point, when performing test statistic, is the pdf. In high energy physics experiments there are two strategies to reconstruct such distributions:

- Use Toy MC
- Use an asymptotic approximation and an "Asimov dataset"

The Toy MC strategy is simple but really time expensive. The pdf of the test statistic are constructed using pseudo-experiments. This method needs to generate a huge number of MC pseudo-experiments and for each experiment has to evaluate the necessary integrals.

The second method is based on asymptotic formulae for likelihood-based tests presented by G.Cowan, K.Cranmer, E.Gross and O.Vitells [88]. The idea is to use a representative dataset, called "Asimov dataset", instead of producing the pseudo-experiments via MC generators. The Asimov dataset is defined as the dataset that, when used to evaluate the estimators for all parameters, gives the true parameter values. This second method is faster than the first one but it suffers from a problem. The asymptotic approximation is not always valid and it is exact only in the large sample limit. However experimentally the approximation seems to provide accurate results even for small sample sizes. In the analysis presented in this thesis the sample size is small, less than 50 events, hence a check on the accuracy of the asymptotic approximation is necessary. This check was performed and the results of Toy MC and asymptotic approximation compared. In tables 6.1, 6.2 and 6.3 the values of CL_s, p_0 and p_1 obtained for both the methods are reported.

The asymptotic approximation seems to be enough accurate and in the next section it will be used instead of the Toy MC pseudo-experiments to calculate the statistical results.

CL_s	Asy Exp	Asy Obs	Toy Exp	Toy Obs
WH 2012	5.1	9.9	5.1	9.9
WH 11/12	4.0	7.5	4.0	7.6
WH + ZH	3.6	7.2	3.6	7.2

Table 6.1: Comparison between CL_s results for asymptotic approximation and Toy MC pseudo-experiments, both expected and observed. The rows represent possible combinations with analyses related to an Higgs boson decay $H \to WW^{(*)} \to l\nu l\nu$. A more detailed description of these combinations is reported in next section.

p_0 (σ)	Asy Obs	Toy Obs
WH 2012	2.3	2.3
WH 11/12	1.65	1.70
WH + ZH	2.10	2.17

Table 6.2: Comparison between p_0 results, observed only, for asymptotic approximation and Toy MC pseudo-experiments. The rows represent possible combinations with analyses related to an Higgs boson decay $H \to WW^{(*)} \to l\nu l\nu$. A more detailed description of these combinations is reported in next section.

p_1 (σ)	Asy Obs	Toy Obs
WH 2012	1.52	1.54
WH 11/12	0.66	0.62
WH + ZH	1.1	1.1

Table 6.3: Comparison between p_1 results for asymptotic approximation and Toy MC pseudo-experiments. The rows represent possible combinations with analysss related to an Higgs boson decay $H \to WW^{(*)} \to l\nu l\nu$. A more detailed description of these combinations is reported in next section.

6.8 Statistical Interpretation

The statistical studies presented here are divided into two main branches. The first one is connected to events with 3-lepton final state (aimed at WH production) presented in chapter 5 while the second is related to all the combinations performed with other analyses. In particular, statistical combinations with three other analyses involving the $H \to WW^{(*)} \to l\nu l\nu$ decay will be presented. These are:

- $WH \to WWW^{(*)} \to l\nu l\nu l\nu$ performed with the data collected by the ATLAS experiment in 2011
- $ZH \to ZWW^{(*)} \to lll\nu l\nu$ performed using the data collected by the ATLAS experiment in 2012
- $H \to WW^{(*)} \to l\nu l\nu$ performed with all the data collected by the ATLAS experiment in 2011 and 2012

The statistical analysis uses a likelihood function $\mathcal{L}(\mu, \boldsymbol{\theta})$ constructed as the product of Poisson probability terms obtained from the number of expected and observed events in signal and control regions. In this expression μ represents the "signal strength" relative to the SM Higgs boson prediction while $\boldsymbol{\theta}$ indicates nuisance parameters. The latter include systematic uncertainties affecting the signal and background predictions and are parametrized as Gaussian functions.

The test statistic q_μ is then constructed using the profile likelihood:

$$q_\mu = -2 \ln \left(\mathcal{L}(\mu, \hat{\boldsymbol{\theta}}_\mu) / \mathcal{L}(\hat{\mu}, \hat{\boldsymbol{\theta}}) \right), \tag{6.33}$$

where $\hat{\mu}$ and $\hat{\boldsymbol{\theta}}$ are the parameters that maximize the likelihood (with the constraint $0 \leq \hat{\mu} \leq \mu$), and $\hat{\boldsymbol{\theta}}_\mu$ are the nuisance parameters' values that maximize the likelihood for a given μ. This test statistic is used to compute exclusion limits following the modified frequentist method known as CL_s [88] [89] described in section 6.6 for 19 different Higgs mass hypotheses between 110 GeV and 200 GeV.

6.8.1 3-lepton analysis for 2012 data

In this section a statistical interpretation of the 3-lepton analysis discussed in chapter 5 will be reported. Three separated signal regions (*Z-depleted*, *Z-enriched* with *eee* and $\mu\mu\mu$ composition and *Z-enriched* with $\mu\mu e$ and $ee\mu$ composition) are used to construct the likelihood function. A nuisance parameter is introduced for each background contribution, describing the uncertainty on the normalization factor. Since a simultaneous fit for the scale factors has been already performed, no additional parameter to normalize the contributions from the control regions is used in this analysis.

The resulting expected, computed in the absence of a SM Higgs boson, and observed upper limits at 95% CL are presented in figure 6.1. The observed limit lies close to the upper edge of the $\pm 2\sigma$ band of the expected limit, reflecting the observed excess of events in the data, as discussed in chapter 5. At $m_H = 125$ GeV, the expected and observed limits are 5.2 and 10.0 times the SM cross section respectively. The size of the excess is quantified by computing the local probability p_0 for a background fluctuation to produce, in the absence of any signal, a number of events at least as large as the observed one. At $m_H = 125$ GeV, this probability is $p_0 = 1.2\%$, corresponding to a significance of the excess of 2.3σ. The probability of obtaining the observed number of events from the expected background plus the SM Higgs boson signal (local probability p_1) can be computed as well. At $m_H = 125$ GeV the significance of the excess with respect to the background plus SM Higgs boson signal is 1.8σ ($p_1 = 3.3\%$) while the signal strength is 5.15 times the SM Higgs boson expectation. In figure 6.2 the local p_0 and the fitted signal strength are presented as a function of the hypothesized Higgs boson mass.

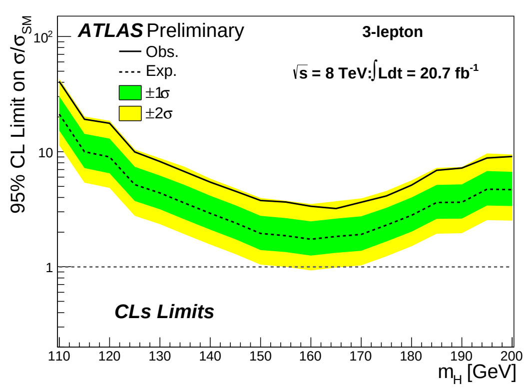

Figure 6.1: Upper limits, observed (continuous line) and expected (dashed line), at 95% CL on the WH production using 20.7 fb^{-1} at $\sqrt{s} = 8$ TeV in the SM Higgs scenario [60]. For a SM Higgs boson at $m_H = 125$ GeV the expected and observed limits are respectively 5.2 and 10.0 times the SM cross section.

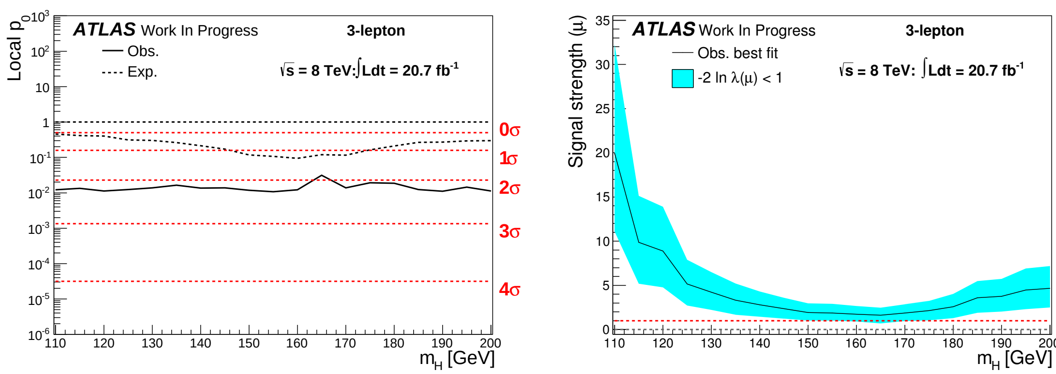

(a) (b)

Figure 6.2: (a) Observed (continuous line) and expected (dashed line) local p_0 as a function of the hypothesized Higgs boson mass for the search for WH production using 20.7 fb^{-1} at $\sqrt{s} = 8$ TeV in the SM Higgs scenario. For a SM Higgs boson at $m_H = 125$ GeV the excess as a significance of 2.3σ. (b) Signal strength as a function of the hypothesized Higgs boson mass using 20.7 fb^{-1} at $\sqrt{s} = 8$ TeV in the SM Higgs scenario. The blue area represents $\pm 1\sigma$ on the signal strength value obtained by the fit.

6.8.2 3-lepton analysis for 2011 data

In this section a combination of the 3-lepton analysis performed using the data acquired in the 2012 and 2011 by the ATLAS experiment is presented. Before going into details of the statistical results a brief introduction to the $WH \rightarrow WWW^{(*)} \rightarrow l\nu\, l\nu\, l\nu$ analysis performed using the data acquired by the ATLAS experiment in the 2011, is presented.

Introduction to the $WH \rightarrow WWW^{(*)} \rightarrow l\nu l\nu l\nu$ 2011 data analysis

This analysis is similar to the one presented in chapter 5. The final state is the same but the center-of-mass energy of the collision was $\sqrt{s} = 7$ TeV instead of 8 TeV. This difference in energy changes the signal and background cross sections and can originate a different definition of signal regions. In this case as shown in table 6.4 the signal regions selections are the same but the background compositions are different. Besides the triboson (VVV) processes, for which the cross section is small, the source of backgrounds are the same described in the previous chapter. Also in the analysis of $WH \rightarrow WWW^{(*)} \rightarrow l\nu l\nu l\nu$ of 2011 (defined here and in the following as “3-lepton 2011”) a distinction between *Z-depleted* and *Z-enriched* is performed to take into account the different sources of background (lepton fakes and the Z-related backgrounds). Due to the limited statistic the *Z-enriched* is not further split according to the number of SFOS lepton pairs.

Signal Selections		
Cut1	require at most 1 jet with transverse momentum above 25 GeV	
Cut2	the jet should not be b-tagged	
Cut3	$E_{T,rel}^{Miss}$ above a threshold	
	Z enriched	*Z depleted*
	$E_{T,rel}^{Miss} > 40$GeV	$E_{T,rel}^{Miss} > 25$ GeV
Cut4	invariant masses of all SFOS pairs should be at least 25 GeV away from the Z boson mass	
	Z enriched	*Z depleted*
	require Z-veto	not applicable
Cut5	the smallest invariant mass of OS lepton pairs is required to be above 12 GeV	
Cut6	$\Delta R_{lep0,lep1}$ is required to be below 2.0	
Cut7	overlap removal with the di-lepton analysis	

Table 6.4: Summary of the selection criteria defining the 3-lepton 2011 signal regions.

A more detailed description of backgrounds and selections could be found in

Ref.[90]. In tables 6.5 and 6.6 the number of expected and observed events at several stages of the cutflow is presented. At the end of the cutflow the number of observed events is compatible with the expectations. As shown in the next section the resulting small deficit changes slightly the significance (p_0 and p_1) of the result obtained considering only 2012 $WH \to WWW^{(*)} \to l\nu l\nu l\nu$ analysis

	$W(Z/\gamma^{(*)})$	WW	ZZ	Z+jets	Top
Pre-selection	392 ± 24	2.26 ± 0.33	85 ± 7	1720 ± 230	38.6 ± 1.2
Z enriched	390 ± 23	1.84 ± 0.27	85 ± 7	1720 ± 230	30.2 ± 1.1
At most 1 jet not b-tagged	335 ± 21	1.65 ± 0.27	75 ± 6	1550 ± 210	5.0 ± 0.5
$E_{T,rel}^{Miss} > 40$ GeV	106 ± 7	0.60 ± 0.15	1.9 ± 0.4	5.2 ± 2.8	1.88 ± 0.30
Z mass veto	6.6 ± 0.7	0.39 ± 0.12	0.31 ± 0.11	1.5 ± 1.5	1.10 ± 0.22
All cuts	3.2 ± 0.8	0.09 ± 0.06	0.17 ± 0.07	–	0.28 ± 0.12
Z depleted	1.36 ± 0.15	0.42 ± 0.11	0.15 ± 0.05	2.1 ± 0.8	8.4 ± 0.6
At most 1 jet not b–tagged	1.08 ± 0.13	0.37 ± 0.10	0.15 ± 0.05	2.0 ± 0.7	1.27 ± 0.29
$E_{T,rel}^{Miss} > 25$ GeV	0.49 ± 0.07	0.17 ± 0.07	0.03 ± 0.03	–	0.52 ± 0.20
All cuts	0.21 ± 0.07	0.00 ± 0.05	0.03 ± 0.03	–	0.01 ± 0.10

Table 6.5: Expected background events at several stages of the cutflow for 3-lepton 2011 analysis. The background processes are reported separately.

Four control regions are defined to check the normalization of the main sources of background. For the *Z-enriched* three control regions are defined (WZ$^{(*)}$, Z+jets and Top) while only a Top CR is defined for the *Z-depleted*. The fit to the background scale factor is performed within the statistical framework rather than with an external simultaneous fit as described in section 5.6.2. In table 6.7 the CRs definitions are reported while in table 6.8 the number of observed and expected events in the control regions and the scale factors are shown.

Combining the 3-lepton 2011 and 2012 results

For the 3-lepton 2011 analysis the likelihood function is constructed as the product of Poisson probability terms obtained from the number of expected and observed events in the signal and control regions. As for the 3-lepton 2012 analysis a nuisance parameter is introduced for each background contribution, describing the uncertainty on the normalization factor. In this case the normalization from the WZ$^{(*)}$, Z+jets and Top components in *Z-enriched* and the Top component in *Z-depleted* are obtained from a combined fit which includes the control regions directly in the statistical framework. In the full likelihood the WZ$^{(*)}$, Z+jets and Top production strength are represented

	$W(H \to WW)$	$Z(H \to WW)$	$V(H \to \tau\tau)$	$H \to ZZ$	Observed	Total Bkg.
Pre-selection	1.78 ± 0.15	3.56 ± 0.30	0.66 ± 0.06	0.97 ± 0.08	2077	2240 ± 260
Z enriched	1.36 ± 0.11	3.50 ± 0.28	0.54 ± 0.05	0.97 ± 0.08	2056	2220 ± 260
At most 1 jet not b-tagged	1.24 ± 0.12	2.22 ± 0.21	0.48 ± 0.05	0.80 ± 0.07	1801	1960 ± 240
$E_{T,rel}^{Miss} > 40$ GeV	0.61 ± 0.05	0.54 ± 0.05	0.10 ± 0.01	0.01 ± 0.01	114	115 ± 10
Z mass veto	0.47 ± 0.05	0.04 ± 0.01	0.04 ± 0.01	–	13	9.9 ± 2.2
All cuts	0.34 ± 0.06	0.03 ± 0.01	0.02 ± 0.01	–	3	3.7 ± 0.9
Z depleted	0.43 ± 0.06	0.06 ± 0.01	0.12 ± 0.02	–	21	12.49 ± 1.07
At most 1 jet,not b-tagged	0.40 ± 0.06	0.04 ± 0.01	0.11 ± 0.02	–	7	4.9 ± 0.9
$E_{T,rel}^{Miss} > 25$ GeV	0.26 ± 0.03	0.02 ± 0.01	0.04 ± 0.01	–	1	1.22 ± 0.24
All cuts	0.18 ± 0.04	0.01 ± 0.01	0.03 ± 0.01	–	0	0.25 ± 0.15

Table 6.6: Expected and observed events at several stages of the cutflow for 3-lepton 2011 analysis. All the signal processes, total background and observed events are reported.

Control Region name	Selection
WZ CR defined only for *Z enriched*	isolated leptons Cut 1: at most one jet with $p_{\mathrm{T},jet} > 25$ GeV Cut 2: no b–tagged jets with $p_T > 25$ GeV Cut 3b: $E^{Miss}_{T,rel} > 25$ GeV $\overline{\text{Cut4}}$: Z mass selection Cut 5: $m_{\ell\ell,min} > 12$ GeV $\overline{\text{Cut6}}$: $\Delta R_{lep0,lep1} > 2.0$ Cut 7: overlap removal with di-lepton analysis
Z+jets CR defined only for *Z enriched*	isolated leptons Cut 1: at most one jet with $p_{\mathrm{T},jet} > 25$ GeV Cut 2: no b–tagged jets with $p_T > 25$ GeV $\overline{\text{Cut3}b}$: $E^{Miss}_{T,rel} < 25$ GeV $\overline{\text{Cut4}}$: Z mass selection $p_T^{lep_0} + p_T^{lep_1} + p_T^{lep_2} > 60$ GeV Cut 7: overlap removal with di-lepton analysis
Top CR *Z enriched*	NO isolation requirement at least 1 jet with $p_T > 25$ GeV $\overline{\text{Cut2}}$:at least 1 b–tagged jet with $p_T > 25$ GeV Cut 3a: $E^{Miss}_{T,rel} > 40$ GeV (*Z enriched*) Cut 4: Z mass veto $p_T^{lep_0} + p_T^{lep_1} + p_T^{lep_2} > 60$ GeV $\Delta R_{lep0,lep1} > 0.5$ Cut 7: overlap removal with di-lepton analysis
Top CR *Z depleted*	NO isolation requirement at least 1 jet with $p_T > 25$ GeV $\overline{\text{Cut2}}$:at least 1 b–tagged jet with $p_T > 25$ GeV Cut 3b: $E^{Miss}_{T,rel} > 25$ GeV (*Z depleted*) $p_T^{lep_0} + p_T^{lep_1} + p_T^{lep_2} > 60$ GeV Cut 7: overlap removal with di-lepton analysis

Table 6.7: Summary of the selections defining the control regions. A bar over a cut means that this is the reverse of the cut in the signal selection.

CR	Observed	Expected	Data/MC	$W(Z/\gamma^{(*)})$	$WW + ZZ$	Z+jets	Top
Z *enriched* : WZ	30	31 ± 5	0.98 ± 0.25	30 ± 5	0.52 ± 0.17	0.4 ± 0.4	0.16 ± 0.10
Z *enriched* : $Z + jets$	365	360 ± 80	1.02 ± 0.23	127 ± 21	32 ± 7	200 ± 50	0.52 ± 0.15
Z *enriched* : Top	84	75.2 ± 1.9	1.12 ± 0.13	0.10 ± 0.04	0.10 ± 0.12	0.5 ± 0.4	74.4 ± 1.8
Z *depleted* : Top	63	59.3 ± 1.6	1.06 ± 0.14	0.04 ± 0.02	0.05 ± 0.03	0.09 ± 0.09	59.1 ± 1.6

Table 6.8: The number of observed events in data for the four control regions defined in the text compared to the total number of expected events and the breakdown of their sources. Uncertainties on each component of the Top control regions are statistical only while for the other control regions they include the experimental systematic uncertainties.

by nuisance parameters which multiply the expected background wherever they appear. In figure 6.3 the resulting expected, computed in the absence of a SM Higgs boson, and observed upper limits at 95% CL combining the results obtained from the data collected at a center-of-mass energy of $\sqrt{s} = 7$ TeV in 2011 [90] and $\sqrt{s} = 8$ TeV in 2012 is presented. At $m_H = 125$ GeV the expected and observed limits are 4.1 and 7.5 times the SM cross section respectively and the observed significance is 1.6σ ($p_0 = 4.9\%$) with respect to the background-only hypothesis and 1.1σ ($p_1 = 13\%$) when including the SM Higgs boson signal. The signal strength is 3.36 times the SM Higgs boson expectation. In figure 6.4 the local p_0 and the fitted signal strength are presented as a function of the hypothesized Higgs boson mass.

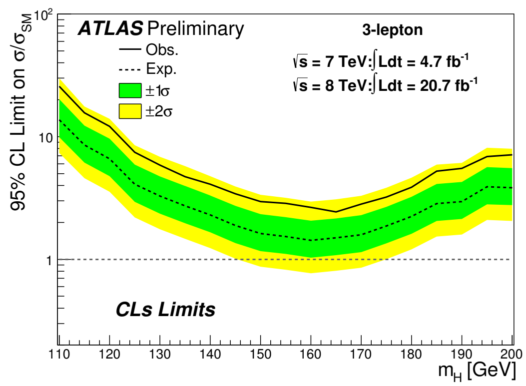

Figure 6.3: Upper limits, observed (continuous line) and expected (dashed line), at 95% CL on the WH production using data acquired by the ATLAS experiment up to the 2012 end. For a SM Higgs boson at $m_H = 125$ GeV the expected and observed limits are respectively 4.1 and 7.5 times the SM cross section.

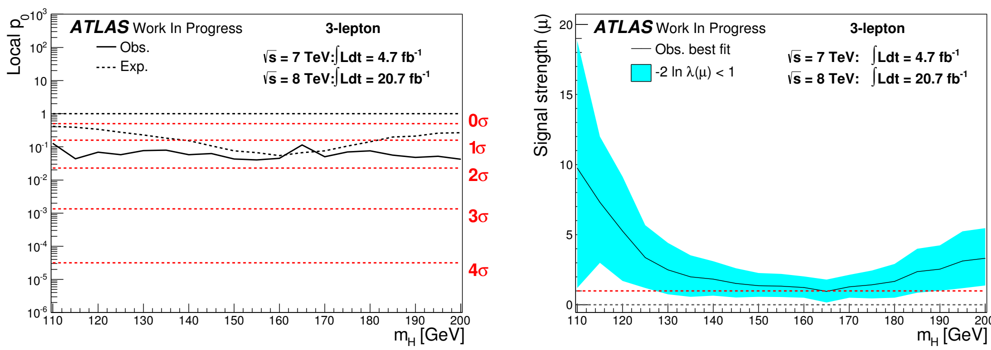

(a) (b)

Figure 6.4: (a)Observed (continuous line) and expected (dashed line) local p_0 as a function of the hypothesized Higgs boson mass for the search for WH production using data acquired by the ATLAS experiment up to the 2012 end in the SM Higgs scenario. For a SM Higgs boson at $m_H = 125$ GeV the excess as a significance of 1.6σ. (b) Signal strength as a function of the hypothesized Higgs boson mass using data acquired by the ATLAS experiment up to the 2012 end in the SM Higgs scenario. The blue area represents $\pm 1\sigma$ on the signal strength value obtained by the fit.

6.8.3 4-lepton analysis 2012

In this section a combination of the 3-lepton analyses, 2011 and 2012, with a $ZH \rightarrow ZWW^{(*)} \rightarrow lll\nu l\nu$ study is presented. The $ZH \rightarrow ZWW^{(*)} \rightarrow lll\nu l\nu$ study, also called 4-lepton analysis, is performed using the data collected by the ATLAS experiment in the 2012. Before going into the details of the statistical results a brief introduction to the 4-lepton analysis is presented.

Introduction to the $ZH \rightarrow ZWW^{(*)} \rightarrow lll\nu l\nu$

The final state of this analysis is characterized by four charged leptons and missing transverse momentum produced by the two neutrinos. Due to the topology of the events the irreducible backgrounds are $ZWW^{(*)} \rightarrow lll\nu l\nu$ and $ZZZ^{(*)} \rightarrow \nu\nu llll$. As in the 3-lepton analyses processes containing fake leptons can lead to the same final state of the signal. Those backgrounds (as $\mathrm{WZ}^{(*)}$+jets and $\mathrm{W}\gamma^{(*)}$+jets) could be suppressed using tight lepton identification criteria. For the 4-lepton analysis the main source of background is the $ZZ^{(*)} \rightarrow llll$ process with fake missing transverse momentum due to the pile-up or mismeasured jets. In this process, if a Z boson does not decay in $\tau\tau$, the final state is characterized by 2 SFOS lepton pairs. The signal, due to the decay of two W bosons, could have 1 SFOS or 2 SFOS lepton pairs. Due to this difference between signal and background topologies, to gain in significance, the signal region is split according to the number of SFOS lepton pairs. The $\mathrm{ZZ}^{(*)}$ contribution is automatically suppressed in the 1SFOS signal region. Moreover a ZZ CR is constructed to compare the data and the MC expectations for this source of background. In table 6.9 a summary of the selections criteria is listed.

The events are selected requiring at most one jet not b-tagged to suppress $\mathrm{t\bar{t}Z}$ process. A requirement on the missing transverse momentum ($E_T^{Miss} > 30$ GeV) is made to suppress events with no real missing transverse momentum. A Z mass window ($|m_{ll} - m_Z| < 10$ GeV) on the leptons not coming from the Higgs boson and a dilepton invariant mass selection on the leptons coming from the Higgs boson are required to suppress the $\mathrm{ZZ}^{(*)}$. A complete description of the selections is reported in Ref. [60]. In this analysis only one CR is constructed. The CR information are used directly in the statistical framework to constraint the number of background events for the $\mathrm{ZZ}^{(*)}$ process. In table 6.10 the list of selections used to define the ZZ CR is reported while in table 6.11 the number of events expected and observed at the end of the cutflow in the control region is showed. In table 6.12 the cutflow at several stages of the selections for both the signal regions of the 4-lepton analysis is reported. Though the analysis is not really sensible to the presence of an Higgs boson due to the low signal over background ratio, the result have an impact on the analysis. A

Signal Selections		
Cut		
E_T^{Miss} cut	$E_T^{Miss} > 30$ GeV	
p_{T}^{ℓ} cuts	highest p_T lepton: $p_T > 25$ GeV second highest p_T lepton: $p_T > 20$ GeV third highest p_T lepton: $p_T > 15$ GeV fourth highest p_T lepton: $p_T > 10$ GeV	
Jet multiplicity	$N_{\mathrm{jet}} \leq 1$	
b-veto	$N_{b-\mathrm{tag}} = 0$	
Mass cuts	$\lvert m_{\ell_2\ell_3} - m_Z \rvert < 10$ GeV 10 GeV $< m_{\ell_0\ell_1} < 65$ GeV	
Angular cut	$\Delta\Phi_{Boost} < 2.5$	
Channel separation	2SFOS	1SFOS
$p_{T4\ell}$ cut	$p_{T4\ell} > 30$ GeV	
$m_{4\ell}$ cut	$m_{4\ell} > 130$ GeV	
Overlap removal	remove overlap with $H \to WW^{(*)}$ analysis	

Table 6.9: Summary of the selection criteria defining the 4-lepton signal regions.

	Selection
ZZ CR	2 SFOS pairs of isolated leptons highest p_T lepton: $p_T > 25$ GeV second highest p_T lepton: $p_T > 20$ GeV third highest p_T lepton: $p_T > 15$ GeV fourth highest p_T lepton: $p_T > 10$ GeV at most one jet with $p_{\mathrm{T,jet}} > 25$ GeV no b–tagged jets with $p_T > 25$ GeV $\lvert m_{\ell_2\ell_3} - m_Z \rvert < 10$ GeV $m_{\ell_0\ell_1} > 65$ GeV overlap removal with dilepton analysis

Table 6.10: Summary of the selections defining the ZZ CR in the 4-lepton analysis.

	Z(H$\to$WW)	Obs.	Total Bkg.	Data/MC	ZZ	Top	VVV	W(Z/$\gamma^{(*)}$)	Z+jets
ZZ CR	0.03 $\pm$ 0.00	100	110.04 $\pm$ 0.73	0.91 $\pm$ 0.09	109.46 $\pm$ 0.73	0.03 $\pm$ 0.01	0.55 $\pm$ 0.03	0.00 $\pm$ 0.00	0.00 $\pm$ 0.00

Table 6.11: Number of observed events in the data for the ZZ CR of the 4-lepton analysis compared to the total number of expected events (indicated here as "MC"), after the application of the normalization factor on the ZZ$^{(*)}$ process. The uncertainty on the data/MC ratio includes statistical and systematic effects.

	ZZ	VVV	Fakes	Total Bkg.	$VH(125)$	Data
4 leptons	164 ± 6	1.89 ± 0.08	8.8 ± 5.8	175 ± 10	0.89 ± 0.04	182
E_T^{Miss} and p_T	41.8 ± 1.6	1.65 ± 0.07	7.8 ± 5.3	51.3 ± 5.6	0.71 ± 0.03	55
Jet multiplicity and b-veto	30.8 ± 1.1	1.30 ± 0.06	0.31 ± 0.11	32.5 ± 1.2	0.52 ± 0.02	35
Mass cuts	2.97 ± 0.15	0.22 ± 0.02	0.05 ± 0.03	3.24 ± 0.16	0.41 ± 0.02	2
Angular cut	1.88 ± 0.12	0.20 ± 0.02	0.04 ± 0.02	2.12 ± 0.12	0.39 ± 0.02	2
1 SFOS pair	0.24 ± 0.04	0.08 ± 0.01	0.00 ± 0.01	0.33 ± 0.05	0.19 ± 0.01	2
Overlap removal	0.23 ± 0.04	0.08 ± 0.01	0.00 ± 0.01	0.32 ± 0.05	0.18 ± 0.01	2
2 SFOS pairs	1.64 ± 0.11	0.12 ± 0.01	0.04 ± 0.02	1.79 ± 0.11	0.20 ± 0.01	0
4ℓ system cuts	0.72 ± 0.07	0.11 ± 0.01	0.04 ± 0.02	0.86 ± 0.08	0.18 ± 0.01	0
Overlap removal	0.70 ± 0.07	0.10 ± 0.01	0.04 ± 0.02	0.84 ± 0.08	0.17 ± 0.01	0

Table 6.12: Number of expected events for the signal and the background, for an integrated luminosity of 20.7 fb^{-1}, and number of events observed in the data, as a function of the selection requirement.

small excess is found in 1 SFOS pair signal region. This excess is compatible with a background only hypothesis but in the combination with the 3-lepton 2011 and 2012 analyses it pushes the total significance toward a lower value.

Combining the 3-lepton 2011, 3-lepton 2012 and 4-lepton results

For the 4-lepton analysis the likelihood function is constructed as the product of Poisson probability terms obtained from the number of expected and observed events in the signal regions and ZZ control region. As for the 3-lepton analyses a nuisance parameter is introduced for each background contribution, describing the uncertainty on the normalization factor. In the 4-lepton case the normalization of the contribution from the ZZ is obtained from a combined fit which includes also the control region in the statistical framework. In the full likelihood the ZZ production strength is represented by a nuisance parameter which multiply the expected background wherever it appears. In figure 6.5 the resulting expected, computed in the absence of a SM Higgs boson, and observed upper limits at 95% CL are presented combining the 3-lepton 2011, 3-lepton 2012 and 4-lepton analysis [90]. At $m_H = 125$ GeV the expected and observed limits are 3.6 and 7.2 times the SM cross section respectively and the observed significance is 2.0σ ($p_0 = 2.1\%$) with respect to the background-only hypothesis and 1.4σ ($p_1 = 7.9\%$) when including the SM Higgs boson signal. The signal strength is 3.72 times the SM Higgs boson expectation. In figure 6.6 the local p_0 and the fitted signal strength are presented as a function of the hypothesized Higgs boson mass.

6.8.4 2-lepton analysis

After the discovery of the SM Higgs boson it became interesting to look into the properties of this particle. In the previous sections a combination between different processes related to the same SM Higgs boson production mechanism, the associated production, has been presented. Another interesting study could be the combination of the results of all the SM Higgs boson production mechanism analyses. Here this kind of combination is presented taking into account only the $H \to WW^{(*)}$ decay. Due to the events topology (mainly the presence of missing transverse momentum), to the background and to the small BR, the $H \to WW^{(*)}$ channel is less sensitive than the $H \to \gamma\gamma$ and $H \to ZZ^{(*)}$ to the presence of a SM Higgs boson. Adding the results obtained combining WH in 3-lepton and ZH in 4-lepton with the $H \to WW^{(*)}$ result, the significance of the analysis reaches 4σ.

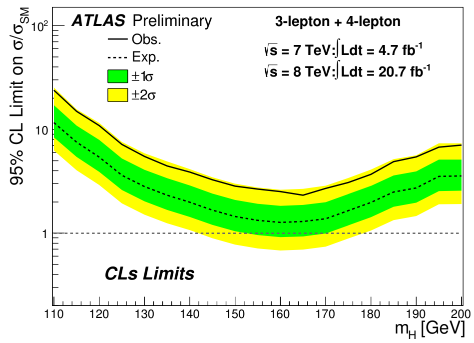

Figure 6.5: Upper limits, observed (continuous line) and expected (dashed line), at 95% CL on the VH (WH + ZH) production cross section as a function of the Higgs boson mass using data acquired by the ATLAS experiment up to the 2012 end. For a SM Higgs boson at $m_H = 125$ GeV the expected and observed limits are respectively 3.6 and 7.2 times the SM cross section.

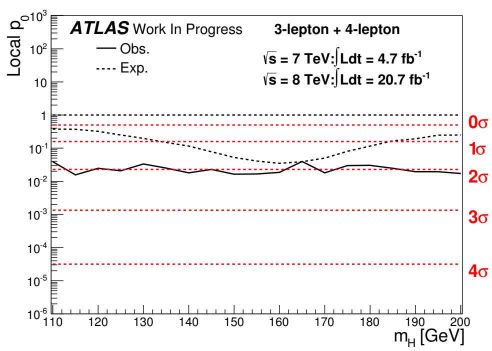

(a)

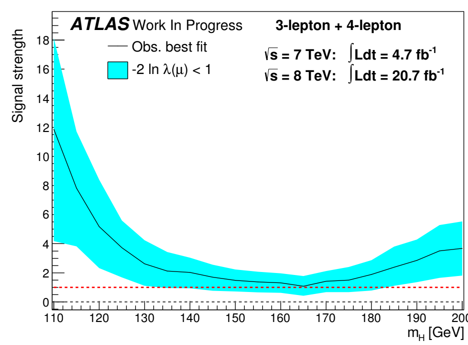

(b)

Figure 6.6: (a)Observed (continuous line) and expected (dashed line) local p_0 as a function of the hypothesized Higgs boson mass for the search for VH production using data acquired by the ATLAS experiment up to the 2012 end in the SM Higgs scenario. For a SM Higgs boson at $m_H = 125$ GeV the excess as a significance of 2.0σ. (b) Signal strength as a function of the hypothesized Higgs boson mass using data acquired by the ATLAS experiment up to the 2012 end in the SM Higgs scenario. The blue area represents $\pm 1\sigma$ on the signal strength value obtained by the fit.

Combining several SM Higgs boson production mechanisms

The $H \to WW^{(*)} \to l\nu l\nu$ studies reported in Ref. [61] are complementary to the studies reported in this thesis since they target mainly the Higgs boson production through the gluon-gluon fusion mechanism and the vector-boson fusion process. Due to overlap removal performed in all the analyses (as described in chapter 5), the combination of the 3-lepton 2011, 3-lepton 2012 and 4-lepton with the analysis presented in Ref. [61] is straightforward. Figure 6.7 shows the expected and observed local p_0 for this combination while in table 6.13 the expected and observed significance for the VH and $H \to WW^{(*)} \to l\nu l\nu$ analyses and their combination for a Higgs boson mass of 125 GeV are reported.

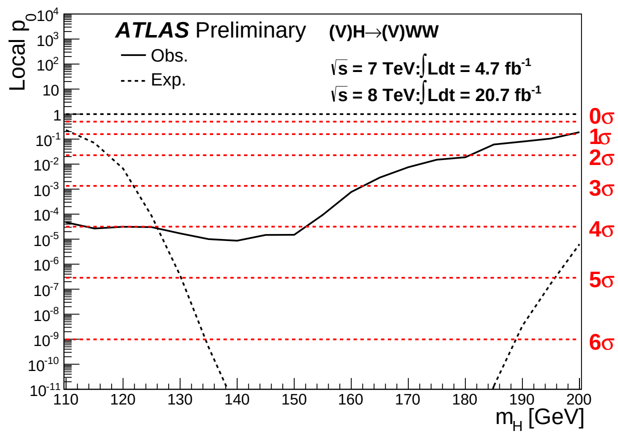

Figure 6.7: The observed (continuous line) and expected (dashed line) local p_0 as a function of the hypothesized Higgs boson mass for the combination of VH and $H \to WW^{(*)} \to l\nu l\nu$ analyses.

significance (σ)	VH	$H \to WW^{(*)} \to l\nu l\nu$ [61]	Combined
expected	0.7	3.7	3.8
observed	2.0	3.8	4.0

Table 6.13: Expected and observed significance for the VH and $H \to WW^{(*)} \to l\nu l\nu$ analyses and their combination, for $m_H = 125$ GeV.

Conclusion

On the 4^{th} of July 2012 both the ATLAS and CMS experiments announced the observation of a new particle in the search for the Standard Model Higgs boson. The discovery is based on the data acquired in pp collisions at LHC by ATLAS and CMS and both the experiments observed a new boson Higgs SM like in a mass range between 125-126 GeV decaying into $\gamma\gamma$, ZZ and WW. This observation contributes to the assignment of the Nobel Prize in Physics 2013 to P. Higgs and F. Englert "for the theoretical discovery of a mechanism that contributes to our understanding of the origin of mass of subatomic particles, and which recently was confirmed through the discovery of the predicted fundamental particle, by the ATLAS and CMS experiments at CERN's Large Hadron Collider" (http://www.nobelprize.org/nobel_prizes/physics/).

After the discovery of this new particle studying his properties becomes the main goal of all the Higgs boson related analyses. In this scenario the study of the associated production mechanisms becomes relevant, in particular to measure the coupling between the Higgs boson and the vector bosons. In this thesis an analysis of the WH associated production mode, with $H \to WW^{(*)}$ and all vector bosons decaying to electrons or muons, is performed using 20.7 fb^{-1} of proton-proton collision data at a center-of-mass energy of 8 TeV collected in 2012 with the ATLAS detector at the CERN Large Hadron Collider.

In chapter 5 the whole analysis structure was presented focusing on the optimized event selection for a $m_H = 125$ GeV and on the comparison between observed and expected events. An excess, although still compatible with a statistical fluctuation, is observed in data, and was carefully investigated. A detailed discussion on the statistical analysis was presented focusing on a Higgs boson mass interval between 110 and 200 GeV. The resulting expected, computed in the absence of a SM Higgs boson, and observed upper limits at 95% CL are presented together with a study of the significance of the excess. The latter was quantified by computing the local probability p_0 for a background fluctuation to produce, in the absence of any signal, a number of events at least as large as the observed one. Also the signal strength and the probability of obtaining the observed number of events from the expected background plus the SM Higgs boson signal (local probability p_1) are computed. At $m_H = 125$ GeV, the expected and observed limits are 5.2 and 10.0 times the SM cross section respectively, the p_0 is 2.3σ, the p_1 is 1.8σ and the signal strength is 5.15 times the SM Higgs boson expectation.

Moreover a combination of this analysis with the $WH \rightarrow WWW^{(*)} \rightarrow l\nu l\nu l\nu$ analysis performed using 4.7 fb^{-1} of proton-proton collision data at a center-of-mass energy of 7 TeV collected in 2011 was presented. At $m_H = 125$ GeV, the expected and observed limits are 4.1 and 7.5 times the SM cross section respectively, the p_0 is 1.6σ, the p_1 is 1.1σ and the signal strength is 3.36 times the SM Higgs boson expectation. These results could be compared with the ones presented in Ref. [91] by the CMS collaboration which describes the result obtained analyzing the $WH \rightarrow WWW^{(*)} \rightarrow l\nu l\nu l\nu$ process using the full 2011-2012 statistics. For the analysis not using the shape of a discriminant variable the resulting observed (expected) upper limit at the 95% CL for $m_H = 125$ GeV is 3.8 (3.7) times larger than the SM expectation.

In this thesis also a combination with the search for the Higgs boson production in association with a Z boson is presented. The analysis considers the $H \rightarrow WW$ decay and a totally leptonic final state and it is performed using 20.7 fb^{-1} of proton-proton collision data at a center-of-mass energy of 8 TeV. At $m_H = 125$ GeV, the expected and observed limits are 3.6 and 7.2 times the SM cross section respectively, the p_0 is 2.0σ, the p_1 is 1.4σ and the signal strength is 3.72 times the SM Higgs boson expectation. It's interesting to compare these results with the ones obtained by the analyses involving the same Higgs boson production mechanism but a different Higgs boson decay channel. In particular due to the high branching ratio at $m_H = 125$ GeV, described in chapter 2, it is interesting to look at the $H \rightarrow b\bar{b}$ channel. The ATLAS collaboration results on $VH \rightarrow Vb\bar{b}$ are presented in Ref. [92]. For $m_H = 125$ GeV, a 95% CL upper limit of 1.4 times the SM expectation is set on the cross section times branching ratio for $pp \rightarrow (W/Z)(H \rightarrow b\bar{b})$ while the expected limit in the absence of signal is 1.3. As expected the $VH \rightarrow b\bar{b}$ analysis is more sensitive than the one presented in this thesis. This can be explained by the larger branching ratio of the $H \rightarrow b\bar{b}$ compared to the $H \rightarrow WW$ for $m_H = 125$ GeV.

Finally a combination with other Higgs boson production mechanism taking into account only the $H \rightarrow WW^{(*)}$ decay is performed. In particular a combination of ggf, vbf and VH associated production modes is presented. With this combination the significance of the $H \rightarrow WW^{(*)}$ analysis reaches 4σ.

Although the associate production for this decay channel is not yet sensitive enough to the SM Higgs boson production this result combined with other production mechanisms has contributed to a small increase in the significance of the Higgs boson observation, but above all it contributes in setting an upper bound to the Higgs boson coupling to the vector bosons strengthening the SM-like nature of the observed particle.

The associate production will play a key role in the Higgs boson properties studies in the next LHC run.

List of Figures

List of Tables

Bibliography

[1] F.Mandl and G.Shaw, *Quantum field theory*. John Wiley and Sons, 1984.

[2] D.H. Perkins, *Introduction to High Enrgy Physics*. Cambridge University Press, 2000.

[3] J. B. et al. (Particle Data Group), *The Review of Particle Physics*, Phys. Rev. D **86** (2012) 010001.

[4] P. W. Higgs, *Broken Symmetries And The Masses Of Gauge Bosons*, Phys. Rev. Lett. **13** (1964) .

[5] F. Englert and R. Brout, *Broken Symmetry and the Mass of Gauge Vector Mesons.*, Phys. Rev. Lett. **13** (1964) .

[6] C. R. Hagen, G. S. Guralnik, and T. W. B. Kibble, *Global Conservation Laws and Massless Particles*, Phys. Rev. Lett. **13** (1964) .

[7] S. L. Glashow, *Partial Symmetries of Weak Interactions*, Nucl. Phys. **22** (1961) .

[8] S. Weinberg, *A Model of Leptons*, Phys. Rev. Lett. **19** (1967) .

[9] ALEPH Collaboration, CDF Collaboration, D0 Collaboration, DELPHI Collaboration, L3 Collaboration, OPAL Collaboration, SLD Collaboration, LEP Electroweak Working Group, Tevatron Electroweak Working Group, SLD Electroweak and Heavy Flavour Groups Collaboration, *Precision Electroweak Measurements and Constraints on the Standard Model*, `arXiv:1012.2367 [hep-ex]`.

[10] ALEPH and CDF and D0 and DELPHI and L3 and OPAL and SLD and LEP Electroweak Working Group and Tevatron Electroweak Working Group and SLD Electroweak Working Group and Heavy Flavour Group Collaboration,

Precision Electroweak Measurements and Constraints on the Standard Model, `arXiv:0811.4682 [hep-ex]`.

[11] M. Baak, M. Goebel, J. Haller, A. Hoecker, D. Ludwig, et al., *Updated Status of the Global Electroweak Fit and Constraints on New Physics*, Eur.Phys.J. **C72** (2012) 2003, `arXiv:1107.0975 [hep-ph]`.

[12] LHC Higgs Cross Section Working Group, S. Dittmaier, C. Mariotti, G. Passarino, and R. Tanaka (Eds.), *Handbook of LHC Higgs Cross Sections: 1. Inclusive Observables*, CERN-2011-002 (CERN, Geneva, 2011) , `arXiv:1101.0593 [hep-ph]`.

[13] LHC Higgs Cross Section Working Group, S. Dittmaier, C. Mariotti, G. Passarino, and R. Tanaka (Eds.), *Handbook of LHC Higgs Cross Sections: 2. Differential Distributions*, CERN-2012-002 (CERN, Geneva, 2012) , `arXiv:1201.3084 [hep-ph]`.

[14] ATLAS Collaboration Collaboration, G. Aad et al., *Combined search for the Standard Model Higgs boson in pp collisions at* $\sqrt{s} = 7$ *TeV with the ATLAS detector*, Phys.Rev. **D86** (2012) 032003, `arXiv:1207.0319 [hep-ex]`.

[15] CMS Collaboration Collaboration, S. Chatrchyan et al., *Combined results of searches for the standard model Higgs boson in pp collisions at* $\sqrt{s} = 7$ *TeV*, Phys.Lett. **B710** (2012) 26–48, `arXiv:1202.1488 [hep-ex]`.

[16] CDF Collaboration Collaboration, T. Aaltonen et al., *Combined search for the standard model Higgs boson decaying to a bb pair using the full CDF data set*, Phys.Rev.Lett. **109** (2012) 111802, `arXiv:1207.1707 [hep-ex]`.

[17] D0 Collaboration Collaboration, V. M. Abazov et al., *Combined search for the standard model Higgs boson decaying to* $b\bar{b}$ *using the D0 Run II data set*, Phys.Rev.Lett. **109** (2012) 121802, `arXiv:1207.6631 [hep-ex]`.

[18] CDF Collaboration, D0 Collaboration Collaboration, T. Aaltonen et al., *Evidence for a particle produced in association with weak bosons and decaying to a bottom-antibottom quark pair in Higgs boson searches at the Tevatron*, Phys.Rev.Lett. **109** (2012) 071804, `arXiv:1207.6436 [hep-ex]`.

[19] ATLAS Collaboration Collaboration, G. Aad et al., *Observation of a new particle in the search for the Standard Model Higgs boson with the ATLAS detector at the LHC*, Phys.Lett. **B716** (2012) 1–29, `arXiv:1207.7214 [hep-ex]`.

[20] CMS Collaboration Collaboration, S. Chatrchyan et al., *Observation of a new boson at a mass of 125 GeV with the CMS experiment at the LHC*, Phys.Lett. **B716** (2012) 30–61, `arXiv:1207.7235 [hep-ex]`.

[21] ATLAS Collaboration Collaboration, G. Aad et al., *Measurements of Higgs boson production and couplings in diboson final states with the ATLAS detector at the LHC*, Phys.Lett. **B726** (2013) 88–119, `arXiv:1307.1427 [hep-ex]`.

[22] ATLAS Collaboration Collaboration, G. Aad et al., *Evidence for the spin-0 nature of the Higgs boson using ATLAS data*, Phys.Lett. **B726** (2013) 120–144, `arXiv:1307.1432 [hep-ex]`.

[23] ATLAS Collaboration, *Study of the spin of the new boson with up to 25 fb^{-1} of ATLAS data*, ATLAS-CONF-2013-040, 2013. http://cds.cern.ch/record/1542341.

[24] ATLAS Collaboration, *Combined coupling measurements of the Higgs-like boson with the ATLAS detector using up to 25 fb^{-1} of proton-proton collision data*, ATLAS-CONF-2013-034, 2013. http://cds.cern.ch/record/1528170.

[25] ATLAS Collaboration, *Coupling properties of the new Higgs-like boson observed with the ATLAS detector at the LHC*, ATLAS-CONF-2011-127, 2012. http://cds.cern.ch/record/1476765.

[26] CMS Collaboration Collaboration, S. Chatrchyan et al., *Measurement of the properties of a Higgs boson in the four-lepton final state*, `arXiv:1312.5353 [hep-ex]`.

[27] ATLAS Collaboration, G. Aad et al., *The ATLAS Experiment at the CERN Large Hadron Collider*, JINST **3** (2008) no. 08, S08003.

[28] *ATLAS: letter of intent for a general-purpose pp experiment at the large hadron collider at CERN.* Letter of Intent. CERN, Geneva, 1992.

[29] ATLAS Collaboration Collaboration, W. Armstrong et al., *ATLAS: Technical proposal for a general-purpose p p experiment at the Large Hadron Collider at CERN*, .

[30] L. Evans and P. Bryant, *LHC Machine*, JINST **3** (2008) no. 08, S08001.

[31] K. Schindl, *The PS Booster as Pre-Injector for LHC*, Tech. Rep. CERN-PS-97-011-DI, CERN, Geneva, Apr, 1997.

[32] P. Collier, B. Goddard, R. Jung, K. Kissler, T. Linnecar, et al., *The SPS as injector for LHC: Conceptual design*, .

[33] *https://twiki.cern.ch/twiki/bin/view/AtlasPublic/LuminosityPublicResults*, tech. rep.

[34] ATLAS Collaboration, G. Aad et al., *Luminosity Determination in pp Collisions at $\sqrt{s} = 7$ TeV Using the ATLAS Detector at the LHC*, Eur.Phys.J. **C71** (2011) 1630, `arXiv:1101.2185 [hep-ex]`.

[35] G. L. Bayatian et al., *CMS Physics: Technical Design Report Volume 1: Detector Performance and Software.* Technical Design Report CMS. CERN, Geneva, 2006.

[36] LHCb Collaboration, J. Alves, A. Augusto et al., *The LHCb Detector at the LHC*, JINST **3** (2008) S08005.

[37] ALICE Collaboration Collaboration, K. Aamodt et al., *The ALICE experiment at the CERN LHC*, JINST **3** (2008) S08002.

[38] TOTEM Collaboration, G. Anelli et al., *The TOTEM experiment at the CERN Large Hadron Collider*, JINST **3** (2008) S08007.

[39] LHCf Collaboration, O. Adriani et al., *The LHCf detector at the CERN Large Hadron Collider*, JINST **3** (2008) S08006.

[40] J. Pinfold, R. Soluk, Y. Yao, S. Cecchini, G. Giacomelli, M. Giorgini, L. Patrizii, G. Sirri, D. H. Lacarrère, K. Kinoshita, J. Jakubek, M. Platkevic, S. Pospísil, Z. Vykydal, T. Hott, A. Houdayer, C. Leroy, J. Swain, D. Felea, D. Hasegan, G. E. Pavalas, and V. Popa, *Technical Design Report of the MoEDAL Experiment*, Tech. Rep. CERN-LHCC-2009-006. MoEDAL-TDR-001, CERN, Geneva, Jun, 2009.

[41] A. Yamamoto, Y. Makida, R. Ruber, Y. Doi, T. Haruyama, et al., *The ATLAS central solenoid*, Nucl.Instrum.Meth. **A584** (2008) 53–74.

[42] A. Foussat, H. H. J. ten Kate, B. Levesy, C. Mayri, Y. Pabot, V. Petrov, M. Raymond, Z. Sun, and P. Védrine, *Assembly Concept and Technology of the ATLAS Barrel Toroid*, IEEE Trans. Appl. Supercond. **16** (2006) 565–569.

[43] D. E. Baynham, J. Butterworth, F. S. Carr, M. J. D. Courthold, D. A. Cragg, C. J. Densham, D. Evans, E. Holtom, J. Rochford, D. Sole, E. F. Towndrow, and G. P. Warner, *Engineering status of the superconducting end cap toroid magnets for the ATLAS experiment at LHC*, IEEE Trans. Appl. Supercond. **10** (2000) no. 1, 357–60.

[44] D. E. Baynham, J. Butterworth, F. S. Carr, C. J. Densham, E. Holtom, D. Morrow, E. F. Towndrow, G. Luijckx, and J. Geerinck, *ATLAS End Cap Toroid Magnets cold mass design and manufacturing status*, IEEE Trans. Appl. Supercond. **14** (2004) 485–490.

[45] *ATLAS inner detector: Technical Design Report, 1.* Technical Design Report ATLAS. CERN, Geneva, 1997.

[46] S. Haywood, L. Rossi, R. Nickerson, and A. Romaniouk, *ATLAS inner detector: Technical Design Report, 2.* Technical Design Report ATLAS. CERN, Geneva, 1997.

[47] G. Aad, M. Ackers, F. Alberti, M. Aleppo, G. Alimonti, et al., *ATLAS pixel detector electronics and sensors*, JINST **3** (2008) P07007.

[48] A. Ahmad, Z. Albrechtskirchinger, P. Allport, J. Alonso, L. Andricek, et al., *The Silicon microstrip sensors of the ATLAS semiconductor tracker*, Nucl.Instrum.Meth. **A578** (2007) 98–118.

[49] ATLAS TRT Collaboration, E. Abat et al., *The ATLAS Transition Radiation Tracker (TRT) proportional drift tube: Design and performance*, JINST **3** (2008) P02013.

[50] *ATLAS liquid-argon calorimeter: Technical Design Report.* Technical Design Report ATLAS. CERN, Geneva, 1996.

[51] *ATLAS tile calorimeter: Technical Design Report.* Technical Design Report ATLAS. CERN, Geneva, 1996.

[52] ATLAS Collaboration, G. Aad et al., *ATLAS muon spectrometer: Technical Design Report.* No. ATLAS-TDR-010. CERN, Geneva, 1997.

[53] *ATLAS Trigger Performance: Status Report*, Tech. Rep. CERN-LHCC-98-015, CERN, Geneva, Jun, 1998.

[54] G. Piacquadio, K. Prokofiev, and A. Wildauer, *Primary vertex reconstruction in the ATLAS experiment at LHC*, J.Phys.Conf.Ser. **119** (2008) 032033.

[55] ATLAS Collaboration, E. Bouhova-Thacker et al., *A framework for vertex reconstruction in the ATLAS experiment at LHC*, J.Phys.Conf.Ser. **219** (2010) 032019.

[56] ATLAS Collaboration, *Improved electron reconstruction in ATLAS using the Gaussian Sum Filter-based model for bremsstrahlung*, ATLAS-CONF-2012-047, 2012. http://cds.cern.ch/record/1449796.

[57] S. Hassani, L. Chevalier, E. Lancon, J. Laporte, R. Nicolaidou, et al., *A muon identification and combined reconstruction procedure for the ATLAS detector at the LHC using the (MUONBOY, STACO, MuTag) reconstruction packages*, Nucl.Instrum.Meth. **A572** (2007) 77–79.

[58] M. Cacciari, G. P. Salam, and G. Soyez, *The Anti-k(t) jet clustering algorithm*, JHEP **0804** (2008) 063, `arXiv:0802.1189 [hep-ph]`.

[59] ATLAS Collaboration, *Commissioning of the ATLAS high-performance b-tagging algorithms in the 7 TeV collision data*, ATLAS-CONF-2011-102, 2011. https://cds.cern.ch/record/1369219.

[60] ATLAS Collaboration, *Search for associated production of the Higgs boson in the* $WH \to WWW^{(*)} \to l\nu l\nu l\nu$ *and* $ZH \to ZWW^{(*)} \to lll\nu l\nu$ *channels with the ATLAS detector at the LHC*, ATLAS-CONF-2013-075, 2013. http://cds.cern.ch/record/1463915.

[61] ATLAS Collaboration, *Measurements of the properties of the Higgs-like boson in the* $WW^{(*)} \to \ell\nu\ell\nu$ *decay channel with the ATLAS detector using 25* fb^{-1} *of proton-proton collision data*, ATLAS-CONF-2013-030, 2013. https://cds.cern.ch/record/1527126.

[62] T. Sjostrand, S. Mrenna, and P. Z. Skands, *A Brief Introduction to PYTHIA 8.1*, Comput.Phys.Commun. **178** (2008) 852–867, `arXiv:0710.3820 [hep-ph]`.

[63] O. Brein, A. Djouadi, and R. Harlander, *NNLO QCD corrections to the Higgs-strahlung processes at hadron colliders*, Phys.Lett. **B579** (2004) 149–156, `arXiv:hep-ph/0307206 [hep-ph]`.

[64] M. Ciccolini, S. Dittmaier, and M. Kramer, *Electroweak radiative corrections to associated WH and ZH production at hadron colliders*, Phys.Rev. **D68** (2003) 073003, `arXiv:hep-ph/0306234 [hep-ph]`.

[65] A. Djouadi, J. Kalinowski, and M. Spira, *HDECAY: A Program for Higgs boson decays in the standard model and its supersymmetric extension*, Comput.Phys.Commun. **108** (1998) 56–74, `arXiv:hep-ph/9704448 [hep-ph]`.

[66] M. L. Mangano et al., *ALPGEN, a generator for hard multi-parton processes in hadronic collisions*, JHEP **0307** (2003) 001, `arXiv:hep-ph/0206293`.

[67] G. Corcella et al., *HERWIG 6: An event generator for hadron emission reactions with interfering gluons (including super-symmetric processes)* , JHEP **0101** (2001) 010.

[68] J. Alwall et al., *Comparative study of various algorithms for the merging of parton showers and matrix elements in hadronic collisions*, Eur. Phys. J. **C53** (2008) 473, `arXiv:0706.2569 [hep-ph]`.

[69] S. Frixione and B. R. Webber, *Matching NLO QCD computations and parton shower simulations*, JHEP **06** (2002) 029, `arXiv:hep-ph/0204244`.

[70] J. M. Butterworth, J. R. Forshaw, and M. H. Seymour, *Multiparton interactions in photoproduction at HERA*, Z. Phys. **C72** (1996) 637–646, `arXiv:hep-ph/9601371`.

[71] P. Nason, *Recent Developments in POWHEG*, PoS **RADCOR2009** (2010) 018, `arXiv:1001.2747 [hep-ph]`.

[72] T. Binoth, M. Ciccolini, N. Kauer, and M. Kramer, *Gluon-induced W-boson pair production at the LHC*, JHEP **0612** (2006) 046, `arXiv:hep-ph/0611170`.

[73] J. Alwall et al., *MadGraph/MadEvent v4: The new web generation*, JHEP **0709** (2007) 028, `arXiv:0706.2334 [hep-ph]`.

[74] J. Alwall, M. Herquet, F. Maltoni, O. Mattelaer, and T. Stelzer, *MadGraph 5 : Going Beyond*, JHEP **1106** (2011) 128, `arXiv:1106.0522 [hep-ph]`.

[75] R. C. Gray, C. Kilic, M. Park, S. Somalwar, and S. Thomas, *Backgrounds To Higgs boson searches from $W\gamma^* \to l\nu l(l)$ asymmetric internal conversion*, arXiv:1110.1368 (2011) , `arXiv:1110.1368 [hep-ph]`.

[76] B. P. Kersevan and E. Richter-Was, *The Monte Carlo event generator AcerMC version 2.0 with interfaces to PYTHIA 6.2 and HERWIG 6.5*, hep-ph/0405247 (2004) , arXiv:hep-ph/0405247.

[77] H.-L. Lai et al., *New parton distributions for collider physics*, Phys. Rev. **D82** (2010) 074024, arXiv:1007.2241 [hep-ph].

[78] P. M. Nadolsky et al., *Implications of CTEQ global analysis for collider observables*, Phys. Rev. **D78** (2008) 013004, arXiv:0802.0007 [hep-ph].

[79] A. Sherstnev and R. S. Thorne, *Parton distributions for the LHC*, Eur. Phys. J **C55** (2009) 553, arXiv:0711.2473 [hep-ph].

[80] ATLAS Collaboration, *The ATLAS Simulation Infrastructure*, Eur.Phys.J. **C70** (2010) 823–874, arXiv:1005.4568 [physics.ins-det].

[81] GEANT4 Collaboration, S. Agostinelli et al., *GEANT4: A Simulation toolkit*, Nucl.Instrum.Meth. **A506** (2003) 250–303.

[82] ATLAS Collaboration, *Electron performance measurements with the ATLAS detector using the 2010 LHC proton-proton collision data*, Eur. Phys. J. C **72** (2012) 1909, arXiv:1110.3174 [hep-ex].

[83] ATLAS Collaboration, *Muon reconstruction efficiency in reprocessed 2010 LHC proton-proton collision data recorded with the ATLAS detector*, ATLAS-CONF-2011-063, 2011. https://cdsweb.cern.ch/record/1345743.

[84] ATLAS Collaboration, *Jet energy measurement with the ATLAS detector in proton-proton collisions at $\sqrt{s} = 7$ TeV*, Eur.Phys.J. **C73** (2013) 2304, arXiv:1112.6426 [hep-ex].

[85] ATLAS Collaboration, *Performance of Missing Transverse Momentum Reconstruction in Proton-Proton Collisions at 7 TeV with ATLAS*, Eur.Phys.J. **C72** (2012) 1844, arXiv:1108.5602 [hep-ex].

[86] K. Cranmer, G. Lewis, L. Moneta, A. Shibata, and W. Verkerke, *HistFactory: A tool for creating statistical models for use with RooFit and RooStats*, Tech. Rep. CERN-OPEN-2012-016, New York U., New York, Jan, 2012.

[87] Kyle Cranmer, *Practical Statistics for the LHC*, tech. rep. http://indico.cern.ch/getFile.py/access?resId=1materialId=slidesconfId=243641.

[88] G. Cowan, K. Cranmer, E. Gross, and O. Vitells, *Asymptotic formulae for likelihood-based tests of new physics*, Eur.Phys.J. **C71** (2011) 1554, arXiv:1007.1727 [physics.data-an].

[89] A.L. Read, *Presentation of search results: the CL_s technique*, J. Phys. G **28** (2002) 2693.

[90] ATLAS Collaboration, *Search for the Associate Higgs Boson production in the Decay Mode Using 4.7 of Data Collected with the ATLAS Detector at* $\sqrt{s} = 7$, ATLAS-CONF-2012-078, 2012. https://cds.cern.ch/record/1460390.

[91] CMS Collaboration Collaboration, S. Chatrchyan et al., *Measurement of Higgs boson production and properties in the WW decay channel with leptonic final states*, arXiv:1312.1129 [hep-ex].

[92] T. A. collaboration, *Search for the bb decay of the Standard Model Higgs boson in associated W/ZH production with the ATLAS detector*, .